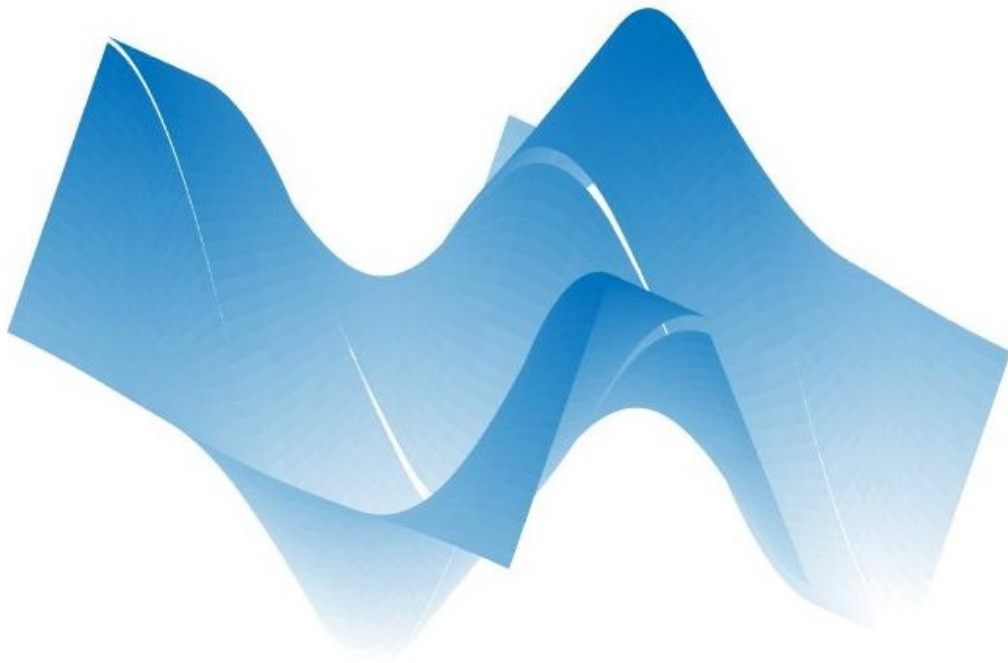


# Development of a fully discontinuous Hybrid Spectral Finite Element Method

Solution of the vector Laplace and the Stokes' equation

Simone Olto





# Development of a fully discontinuous Hybrid Spectral Finite Element Method

Solution of the vector Laplace and the Stokes' equation

by

Simone Olto

to obtain the degree of Master of Science in Aerospace Engineering

at the Delft University of Technology,

to be defended publicly on Monday June 17, 2019.

|                   |                              |          |
|-------------------|------------------------------|----------|
| Student number:   | 4511468                      |          |
| Project duration: | June 1, 2017 – June 17, 2019 |          |
| Supervisor:       | Prof. ir. M. I. Gerritsma    | TU Delft |
| Thesis committee: | Prof. dr. S. Hickel          | TU Delft |
|                   | Dr. M. Möller                | TU Delft |
|                   | Ir. V. Jain                  | TU Delft |

An electronic version of this thesis is available at <http://repository.tudelft.nl/>.



# Acknowledgements

I see computational fluid dynamics as the perfect fusion of math and physics: I think this is the main reason why I started studying numerical methods applied to fluid dynamics. This explains even why I have decided to examine in depth mimetic methods. I heard about this particular class of numerical methods during the CFD1 course held by Dr. Gerritsma. Back then I had no idea this would have ended in a master thesis' project.

For this reason, first of all, I would like to thank my thesis supervisor Dr. Marc Gerritsma for his support and help throughout the whole writing phase of this thesis. Furthermore, I would like to express my gratitude to J. Varun, who got me back on track during the hardest times. It is not a commonplace to say that I would not have been able to complete this thesis without them.

Being a student it is not easy. Lots of people helped me along this journey. I would like to thank my parents, Cinzia and Cludio, and my sister Valentina to have always encouraged me to pursue this master degree. Furthermore, I would like to mention all the people that I have met in the last four years: the Italian friends of the old whatsapp group "Karting & more", my flatmates in Lisztstraat, the DUT18 Aero department and the friends that I have met during my time in Stuttgart and then in Munich. Moreover, a very special thank you goes to all my friends in Italy.

Last but not least I would like to thank Sara, who always believed in me even more than I believed in myself, who supported me in my lightest and darkest days. For sure, without her, I would not be here today.

*Simone Olto*  
*Delft, June 2019*



# Abstract

Being able to solve numerically partial differential equations is fundamental for engineers to evaluate, optimize and improve industrial equipments. The framework of mimetic finite element methods allows engineers to find solutions characterized by strong conservation properties: this may result in a pointwise divergence free-flow field. However, sometimes, the computation of the solution of partial differential equations is time consuming, as a results, to reduce the computational time, engineers and mathematicians have developed hybrid methods.

The objective of this thesis is the development of a hybrid mixed finite element formulation of the vector Laplace equation without spurious modes. Discontinuous elements permit an higher degree of parallelism, and, at the end, a lower computational time. Lagrange multipliers are used to impose continuity between discontinuous elements. These turn out to be not only mathematical features but they are connected to the physical variables of the problem. Furthermore, it has been found that the usage of a new Lagrange multiplier, on the intersection of 4 or more elements, removes the spurious modes. Therefore, the associated system of equation is non-singular. The usage of the hybrid finite element methods reduces the computational time while maintaining the pointwise divergence constraint and the optimal convergence rate of all variables.

At the end, the mixed hybrid formulation is modified to solve the Stokes equations. Lagrange multipliers are used as boundary conditions. Solution of the lid-driven Stokes flow is shown.



# Contents

|  |           |
|--|-----------|
| <b>List of Figures</b>   | <b>ix</b> |
| <b>1 Introduction</b>  | <b>1</b>  |
| <b>2 Basics of mimetic methods</b>   | <b>3</b>  |
| 2.1 The divergence operator and its discrete counterpart . . . . .                   | 5         |
| 2.2 The curl operator and its discrete counterpart . . . . .                         | 7         |
| 2.3 The mimetic element and the associated basis functions . . . . .                 | 8         |
| 2.3.1 Primal grid: basis functions, reconstruction and reduction operators . . . . . | 11        |
| 2.3.2 Dual grid: basis functions, reconstruction and reduction operators . . . . .   | 13        |
| 2.4 Wedge, mass and Hodge matrices . . . . .   | 15        |
| 2.4.1 Algebraic-dual basis functions . . . . .                                       | 16        |
| <b>3 The vector Laplace equation</b>   | <b>19</b> |
| 3.1 From the Stokes to the Laplace equation . . . . .                                | 19        |
| 3.2 Variable-geometry association . . . . .  | 20        |
| 3.3 Weak and matrix formulation . . . . .  | 22        |
| <b>4 Discontinuous approach</b>  | <b>27</b> |
| 4.1 The discontinuous element . . . . .  | 28        |
| 4.1.1 Inter-element flux continuity . . . . .  | 29        |
| 4.1.2 Inter-element point continuity . . . . .                                       | 32        |
| 4.2 Variational formulation: discontinuous elements . . . . .                        | 34        |
| 4.3 Cross-intersections: a non-singular system . . . . .                             | 35        |
| 4.4 Domain discretization . . . . .  | 36        |
| 4.5 Non-singular variational formulation . . . . .                                   | 37        |
| 4.6 The <i>Lagrange multipliers</i> ' system . . . . .                               | 40        |
| 4.7 A new set of basis functions . . . . .   | 42        |

|          |   |           |
|----------|---|-----------|
| <b>5</b> | <b>Model Verification</b>   | <b>47</b> |
| 5.1      | Divergence-free manufactured solution . . . . .                                       | 47        |
| 5.2      | Qualitative analysis . . . . .  | 48        |
| 5.3      | $h$ -Convergence rate analysis. . . . .   | 53        |
| 5.4      | $p$ -Convergence rate . . . . .   | 55        |
| 5.5      | Computation time . . . . .  | 56        |
| <b>6</b> | <b>Lid-driven cavity Stokes-flow</b>  | <b>57</b> |
| 6.1      | Incompressible Stokes equations: from the variational to the matrix formulation . . . | 57        |
| 6.2      | Numerical solution. . . . .   | 61        |
| <b>7</b> | <b>Conclusions and further developments</b>   | <b>67</b> |
| 7.1      | Further developments . . . . .  | 68        |
| 7.1.1    | A physical meaning for $\theta$ . . . . .   | 68        |
| 7.1.2    | $h$ and $p$ local refinement. . . . .   | 70        |
|          | <b>Bibliography</b>   | <b>73</b> |
| <b>A</b> | <b>2-dimensional basis functions</b>  | <b>77</b> |
| A.1      | Primal basis functions . . . . .  | 78        |
| A.2      | Perfect-dual basis functions. . . . .   | 80        |
| <b>B</b> | <b>Verification: continuous formulation</b>   | <b>83</b> |
| B.1      | Manufactured solution . . . . .   | 83        |
| B.2      | Qualitative analysis . . . . .  | 83        |
| B.3      | Convergence analysis . . . . .  | 85        |
| B.4      | Analysis on the sparsity structure . . . . .  | 86        |
| <b>C</b> | <b>Vector calculus</b>  | <b>89</b> |
| <b>D</b> | <b>Condition number and error propagation</b>   | <b>91</b> |
| <b>E</b> | <b>Elimination of spurious modes by Cockburn et. al. [14]</b>                         | <b>93</b> |

# List of Figures

|     |   |    |
|-----|---|----|
| 2.1 | Outer-oriented 2-dimensional cell complex. . . . .  | 5  |
| 2.2 | Inner-oriented 2-dimensional cell complex. . . . .  | 7  |
| 2.3 | (left) primal outer oriented grid, (center) dual inner oriented grid, (right) oriented <i>cell complex</i> . . . . .  | 8  |
| 2.4 | $3^{rd}$ -degree element. Primal and dual grid are show black and red. The variables $-\omega, u, p$ - may be associated to the primal points, lines and surfaces or to the dual surfaces, lines and points, respectively. Blue arrows show the orientation of each primal <i>space element</i> and its dual counterpart. . . . .   | 9  |
| 2.5 | Primal <i>nodal</i> (left) and <i>edge basis functions</i> (right), $N = 4$ . Circular marks are placed where $h_i(x_i) = 1$ and $\int_{x_i}^{x_{i+1}} e_i(x) dx = 1$ is shown with a coloured shadow. $x_i$ represent the Lobatto points. . . . .  | 12 |
| 2.6 | Dual <i>nodal</i> (left) and <i>edge basis functions</i> (right), $N = 4$ . Circular marks are placed where $h_i(x_i) = 1$ and $\int_{\tilde{x}_i}^{\tilde{x}_{i+1}} e_i(x) dx = 1$ is shown with a coloured shadow. $\tilde{x}_i$ represent the Gauss points. . . . .  | 14 |
| 2.7 | Algebraic-dual <i>nodal</i> (left) and <i>edge basis functions</i> (right), $N = 4$ . $x_i$ represent the Lobatto points. . . . .   | 16 |
| 3.1 | Continuous primal element. The variables $\omega^{(n-2)}$ , $u^{(n-1)}$ and $p^{(n)}$ are associated to the points, lines and surfaces of the primal grid, respectively. Arrows show the <i>outer orientations</i> . . . . .  | 22 |
| 3.2 | Continuous primal-dual element. The variables $\omega^{(n-2)}$ and $u^{(n-1)}$ are associated to the points and lines of the primal (black) grid, respectively. The variable $p$ is associated to the dual (red) points. Black arrows denote an <i>outer orientation</i> , while the red ones an <i>inner orientation</i> . . . . . | 24 |
| 3.3 | Sparsity structure of the LHS in (3.17) (left) and in (3.18) (right). $2 \times 2$ grid, $4^{th}$ order elements. . . . .   | 24 |
| 4.1 | Element with embedded boundary. . . . .   | 28 |

|  |    |
|--|----|
| 4.2 Flux continuity . . . . .  | 29 |
| 4.3 Lagrange multiplier $\lambda$ : local numbering. . . . .   | 31 |
| 4.4 Point continuity. . . . .  | 32 |
| 4.5 Lagrange multiplier $\gamma$ : local numbering. . . . .  | 33 |
| 4.6 Cross-intersection: local numbering. . . . .   | 35 |
| 4.7 Position of the <i>Lagrange multipliers</i> on a $3 \times 3$ grid of $2^{nd}$ order elements. $\lambda$ is represented by red points on the boundary of the elements, $\gamma$ by the red lines and $\theta$ by the black points in the intersections. Each element may be seen in Figure 4.1. . . . .  | 37 |
| 4.8 Sparsity structure of the LHS in (4.26) (left) and in (4.27) (right). $2 \times 2$ grid, $4^{th}$ order elements. . . . .  | 39 |
| 4.9 Solution flowchart . . . . .   | 40 |
| 4.10 Number of degrees of freedom of the continuous, the full hybrid and the reduced formulation varying the number of elements (left) and the polynomial degree (right). . . . .  | 42 |
| 4.11 $p_{\lambda_1}$ (top-left), $\omega_{\lambda_1}$ (top-right), $u_{\lambda_1}$ (bottom). Solution of (4.38) for $\lambda_1 = 1$ . Single element of $2^{nd}$ -order degree. . . . .  | 43 |
| 4.12 $p_{\gamma_1}$ (top-left), $\omega_{\gamma_1}$ (top-right), $u_{\gamma_1}$ (bottom). Solution of (4.39) for $\lambda_1 = 1$ . Single element of $2^{nd}$ -order degree. . . . .   | 44 |
| 5.1 Comparison of the reconstruction of the <i>Lagrange multiplier</i> $\gamma$ along internal element boundaries (coloured full lines) with the tangential part of the solution (dashed lines, grey shadow). The reconstruction on vertical lines is compared to $u_y$ (left) while the one on horizontal lines to $u_x$ (right). $5 \times 5$ grid, $2^{nd}$ order elements. . . . . | 48 |
| 5.2 Comparison of the reconstruction of the Lagrange multiplier $\lambda$ along internal element boundaries (coloured full lines) with the divergence of the solution (dashed lines, grey shadow). $5 \times 5$ grid, $2^{nd}$ order elements. . . . .   | 49 |
| 5.3 Reconstruction of the <i>Lagrange multiplier</i> $\theta$ on the point intersection of more than two elements. $5 \times 5$ grid, $2^{nd}$ order elements. . . . .   | 49 |
| 5.4 Comparison between the numerical (left) and the exact solution (right) of the vorticity ( $\omega$ ). $5 \times 5$ grid, $2^{nd}$ order elements. . . . .  | 50 |
| 5.5 Comparison between the numerical (left) and the exact solution (right) of the horizontal velocity ( $u_x$ ). $5 \times 5$ grid, $2^{nd}$ order elements. . . . .   | 50 |
| 5.6 Comparison between the numerical (left) and the exact solution (right) of the vertical velocity ( $u_x$ ). $5 \times 5$ grid, $2^{nd}$ order elements. . . . .   | 51 |

|      |  |    |
|------|--|----|
| 5.7  | Reconstruction of the vertical velocity, $u_x$ , (left) and the horizontal velocity, $u_y$ , (right) in prospective view. $5 \times 5$ grid, $2^{nd}$ order elements. . . . .  | 51 |
| 5.8  | Position of the degrees of freedom of $u_x$ (left) and $u_y$ (right) and the <i>Lagrange multipliers</i> $\lambda$ which respectively impose their continuity. . . . .   | 52 |
| 5.9  | Reconstruction of the variable $p$ , which is equal to $\nabla \cdot u$ , on the domain $\Omega$ . $5 \times 5$ grid, $2^{nd}$ order elements. . . . .   | 53 |
| 5.10 | h-Convergence plot of $L^2(\Omega)$ -error of the divergence of $u$ , $p$ . $K = \{3^2, 6^2, \dots, 33^2\}$ . . .  | 53 |
| 5.11 | h-convergence of $L^2(\Omega)$ -error of the velocity $u$ (left) and the vorticity (right). $K = \{3^2, 6^2, \dots, 33^2\}$ . . . . .  | 54 |
| 5.12 | h-Convergence plot of $L^2(\partial K)$ -error of $\lambda$ (left) and $\gamma$ (right). $K = \{3^2, 6^2, \dots, 33^2\}$ . . . .   | 55 |
| 5.13 | $N$ -Convergence plot of $L^2(\Omega)$ -error of $p$ , $\omega$ ad $u$ . $2 \times 2$ grid (left) and $3 \times 3$ grid (right). .   | 55 |
| 5.14 | Computational time [s] for $K = \{2^2, 4^2, \dots, 40^2\}$ , $N = 2$ (left) and for $K = 3^2$ , $N = \{2, 3, \dots, 15\}$ (right). . . . .   | 56 |
| 6.1  | Lid-driven cavity Stokes flow: discretization of the physical domain. $u$ and $\omega$ are described by the primal black edges and points while the internal dual red points describe the position of $p$ . The red points and lines in the element boundaries shows the <i>Lagrange multipliers</i> $\lambda$ and $\gamma$ , respectively. The blue points represents the location of $\theta$ . On the boundary blue primal edges impose the impermeability condition while the green edges, on the top boundary, impose the unitary tangential velocity boundary condition. . . . . | 58 |
| 6.2  | Sparsity structure of the LHS in (6.3)(left) and mixed method presented by J.Kreeft et al. in [19] (right). $2 \times 2$ grid, $4^{th}$ order elements. . . . .  | 60 |
| 6.3  | Numerical solution of the lid-driven Stokes flow: velocity magnitude (top-left), vorticity (top-right), pressure (bottom-left) and the divergence of the velocity (bottom-right). $16 \times 16$ grid, $4^{th}$ order elements. . . . .  | 61 |
| 6.4  | Comparison of the reconstruction of the Lagrange multiplier $\lambda$ along internal element boundaries (colored lines) with the pressure (grey shadow). $16 \times 16$ grid, $4^{th}$ order elements. . . . .   | 62 |

|      |  |    |
|------|--|----|
| 6.5  | Comparison of the reconstruction of the <i>Lagrange multiplier</i> $\gamma$ along internal element boundaries (colored lines) with the tangential velocity (grey shadow). The reconstruction on vertical lines is compared to $u_y$ (left) while the one on horizontal lines to $u_x$ (right). $16 \times 16$ grid, $4^{th}$ order elements. . . . . | 63 |
| 6.6  | Reconstruction of the <i>Lagrange multiplier</i> $\theta$ at every cross-intersection. $16 \times 16$ grid, $4^{th}$ order elements. . . . .   | 63 |
| 6.7  | Incompressibility constraint. $N = 1, 2, 4$ and $K = \{4^2, 5^2, \dots, 16^2\}$ . . . . .  | 64 |
| 6.8  | Comparison of horizontal velocity ( $u_x$ ) on the vertical centreline (left) and vertical velocity ( $u_y$ ) on the horizontal centreline. Reference solution [23]. $16 \times 16$ grid, $1^{st}, 2^{nd}$ and $4^{th}$ order elements. . . . .  | 64 |
| 6.9  | Horizontal velocity ( $u_x$ ) on the vertical centreline (left) and vertical velocity ( $u_y$ ) on the horizontal centreline. Reference solution [23]. $K = \{4^2, 8^2, 16^2, 32^2\}$ , $1^{st}$ order elements. . . . .   | 65 |
| 6.10 | Horizontal velocity ( $u_x$ ) on the vertical centreline (left) and vertical velocity ( $u_y$ ) on the horizontal centreline. $K = \{4^2, 8^2, 16^2, 32^2\}$ , $1^{st}$ order elements. . . . .  | 65 |
| 6.11 | Effect of the $h$ -convergence on the solution of the top-right vorticity ( $\omega$ ) singularity. Red empty circles show the primal points of the most upper-left element. . . . .   | 66 |
| 7.1  | Element with embedded dual boundary. . . . .   | 69 |
| 7.2  | Comparison of the <i>Lagrange multipliers</i> ' location on the intersection of four elements: numerical method developed along this thesis (left) and its possible improvement (right). . . . .   | 69 |
| 7.3  | Graphical representation of a $p$ -refinement. . . . .   | 71 |
| 7.4  | Graphical representation of an $h$ -refinement. . . . .  | 72 |
| A.1  | $\epsilon^{(n-2)}$ on a $3^{rd}$ order element (Figure 2.4) in the domain $\Omega_k$ (A.2). . . . .  | 78 |
| A.2  | Horizontal $\epsilon^{(n-1)}$ on a $3^{rd}$ order element (Figure 2.4) in the domain $\Omega_k$ (A.2). . . . .   | 78 |
| A.3  | Vertical $\epsilon^{(n-1)}$ on a $3^{rd}$ order element (Figure 2.4) in the domain $\Omega_k$ (A.2). . . . .   | 79 |
| A.4  | $\epsilon^{(n)}$ on a $3^{rd}$ order element (Figure 2.4) in the domain $\Omega_k$ (A.2). . . . .  | 79 |
| A.5  | $\tilde{\epsilon}^{(0)}$ on a $3^{rd}$ order element (Figure 2.4) in the domain $\Omega_k$ (A.2). . . . .  | 80 |
| A.6  | Vertical $\tilde{\epsilon}^{(1)}$ on a $3^{rd}$ order element (Figure 2.4) in the domain $\Omega_k$ (A.2) . . . . .  | 80 |
| A.7  | Horizontal $\tilde{\epsilon}^{(1)}$ on a $3^{rd}$ order element (Figure 2.4) in the domain $\Omega_k$ (A.2) . . . . .  | 81 |
| A.8  | $\tilde{\epsilon}^{(2)}$ on a $3^{rd}$ order element (Figure 2.4) in the domain $\Omega_k$ (A.2) . . . . .   | 81 |
| B.1  | Comparison between the numerical (left) and the exact solution (right) of the vorticity ( $\omega$ ). $5 \times 5$ grid, $2^{nd}$ order elements. . . . .  | 84 |

|     |   |    |
|-----|---|----|
| B.2 | Comparison between the numerical (left) and the exact solution (right) of the horizontal velocity ( $u_x$ ). $5 \times 5$ grid, $2^{nd}$ order elements. . . . .                  | 84 |
| B.3 | Comparison between the numerical (left) and the exact solution (right) of the vertical velocity ( $u_x$ ). $5 \times 5$ grid, $2^{nd}$ order elements. . . . .                    | 85 |
| B.4 | $h$ -Convergence plot of $L^2(\Omega)$ -error of the divergence of $u$ , $p$ . $K = \{3^2, 6^2, \dots, 33^2\}$ . . .  | 85 |
| B.5 | $h$ -convergence of $L^2(\Omega)$ -error of the velocity $u$ (left) and the vorticity (right). $K = \{3^2, 6^2, \dots, 33^2\}$ . . . . .  | 86 |
| B.6 | $p$ -convergence of $L^2(\Omega)$ -error of the $p$ , $u$ and $\omega$ . $2 \times 2$ grid (left) $3 \times 3$ grid (right). . . .  | 86 |
| B.7 | Sparsity structure of the LHS in (3.17) computed using $N$ (left) and $2*N$ Lobatto points (right). $2 \times 2$ grid, $4^{th}$ order elements. . . . .                           | 87 |
| B.8 | $h$ -convergence of $L^2(\Omega)$ -error of $u$ and $\omega$ (left) and $p$ (right) using the approximated matrix (figure B.7-left) and the exact one (figure B.7-right). . . . . | 88 |
| E.1 | Singular cross intersection. . . . .  | 93 |



# Introduction

Computational Fluid Dynamics is the study of numerical methods, which are able to solve and analyse the motions of fluids. Over the last years, its usage has significantly increased for the evaluation, optimization and improvement of the design process for various industrial applications. The advent of commercial software and the exponential increase of computational power, in fact, drove its transition from an exclusive research instrument to an instrument for almost everyday use.

Nonetheless, nowadays, CFD poses new challenges to researchers involved in its development. Physical problems are described by partial differential equations (PDE), which express fundamental conservation laws. Conserving quantities such as mass, momentum, or energy is paramount: this has pushed the development of conserving methods, also called *mimetic* methods.

The incompressible *Navier-Stokes equations*, which describe the motion of fluids, can be modified in order to find a simpler equation that incorporates, at least, part of the structure of the fluid flow equations. The reasoning starts from the incompressible Navier-Stokes equations

$$\left\{ \begin{array}{l} \frac{\partial \vec{u}}{\partial t} + \vec{u} \cdot \nabla \vec{u} + \frac{1}{\rho} \nabla p - \nu \nabla^2 \vec{u} = f \\ \nabla \cdot \vec{u} = 0 \end{array} \right. , \quad (1.1)$$

$$(1.2)$$

which, assuming Low Reynolds number <sup>1</sup>, can be simplified into the *Stokes equations*:

$$\begin{cases} \nabla p - \mu \nabla^2 \vec{u} = f & (1.3) \\ \nabla \cdot \vec{u} = 0 & (1.4) \end{cases}$$

Although their simpler mathematical description, the *Stokes equations* find multiple engineering application such as the computation of the flow around immersed bodies (i.e. small particles) or in lubrication theory. Furthermore, their modified version, called Darcy-Brinkman-Stokes equations [9], describes the flow through porous media, which is relevant, for example, to petroleum engineering.

The equations (1.3) and (1.4) turn out to be very close to the mixed formulation of the *vector Laplace* equation. For this reason, the objective of this thesis is the development of an hybrid mixed finite element method for the *vector Laplace* equation, able to exactly impose the incompressibility constraint. However, the hybrid approach creates a singular system in many cases where more than two elements come together (cross-intersection). As a consequence, the research question may be stated as follows:

Research question: how do we remove singular modes from the hybrid  
formulation of the *vector Laplace* equation?

In order to reply to this research question, the thesis has been structured as follows. In Chapter 2 the basics of mimetic methods is presented. The sets of basis functions are defined; incidence, wedge and mass matrices are introduced. In Chapter 3 the relation between the *Stokes equations* and the *vector Laplace* equation is explained. The variational formulation is derived first supposing primal continuous elements, then primal-dual elements. The matrix formulation is set up. Furthermore, advantages and disadvantages of a primal-dual formulation are discussed. Chapter 4 describes the hybrid formulation for discontinuous elements. A new set of *Lagrange multipliers* is used to remove the singularities created by the cross-intersections among elements. At the end of the chapter, the *Lagrange multipliers'* system is introduced and the *Lagrange multipliers* are characterized. In Chapter 5 results are shown using a divergence-free manufactured solution, while in Chapter 6, after having modified the variational and matrix formulation to solve the *Stokes equations*, the lid-driven Stokes flow was computed and compared with [23]. Conclusions and possible future developments are discussed in Chapter 7.

<sup>1</sup>Using the following dimensionless(\*) quantities:  $\vec{u}^* = \frac{\vec{u}}{U}$ ,  $x^* = \frac{x}{L}$ ,  $p^* = \frac{pL}{\mu U}$ .

# 2

## Basics of mimetic methods

A *mimetic* method is a numerical method which mimics fundamental properties of mathematical and physical systems, including conservation laws, symmetry and positiveness [21]. In this context, the word *mimetic* is related to the exactness, in some sense, of the discrete version of the partial differential operators: We will see how the natural discrete counterpart of the divergence, the curl and the gradient operator may be traced back, respectively, to the divergence theorem, the Stokes theorem and the fundamental theorem of calculus[24].

A mimetic method may be developed using the pairing between geometry and variables, hidden in the conservation laws, which may get lost in the passage towards partial differential equation (PDE). The first study on this geometry-variable association was conducted by E. Tonti, who recognized that similarities between physical theories arise from the connection of the physical variables to the same *space elements*<sup>1</sup>. Furthermore, he recognised that two orientations, *outer* or *inner*, are associated to each *space element* [26, 28].

Having two possible orientations for each *space element* means, for example, that a velocity field may be discretized using velocity fluxes through mesh surfaces (*outer orientation*) or using tangential velocities along mesh edges (*inner orientation*)<sup>2</sup>. The double interpretation of the same velocity field leads to the definition of an operator able to switch among the two. This is called *hodge* and indicated by the symbol  $\star$ . Arnold, Falk & R. Winther [1]; Bochev & Hyman [6]; Kreeft,

---

<sup>1</sup>E. Tonti called *space elements* all points, lines, surfaces and volumes that create a mesh.

<sup>2</sup>Supposing a 3-dimensional domain.

Palha & Gerritsma [20] agree that the definitions of the Hodge operator and the discrete operators of the differential operator lead to a finite element method in which metric-dependent and metric-independent terms are clearly recognizable. On this matter, Tarhasaari, Kettunen & Bossavit write: *the  $\star$ -operator can be exploited to separate the metric-dependent and metric-independent parts of boundary value problems*, [25].

The association between variable and *space elements* creates the need of new *basis functions* (indicated with the letter  $\epsilon$  along this thesis) defined over each element<sup>3</sup>. Finite element methods are based on *basis functions*, which are continuous on each element and are defined according to the following:

$$\epsilon_i(x_j) = \begin{cases} 1 & \text{if } i = j, \\ 0 & \text{if } i \neq j, \end{cases} \quad (2.1)$$

where  $x_j$  indicate the  $j^{\text{th}}$  point of the element. It is worth to underline that, up to now, no restriction on the geometry of the element, or the degree of the *basis functions* has been made. Nonetheless, using this definition, we can state that such  $\epsilon$  associate the variable that they discretize to the points resulting from the discretization of the domain (i.e. the mesh). For this reason (2.1) will be called *nodal basis functions*. This does not mean that such  $\epsilon$  are defined only in certain points. On the contrary, they are defined over the whole element, and consequently the whole domain.

Engineers and mathematicians, who are used to work on computational physics, know that a mesh is composed by points, lines, surfaces and volumes. According to E. Tonti, all of them are *space elements* and it should be possible to associate variables to each of them. This is the reason why *edge basis functions* were developed in [12]. As the *nodal basis functions* are equal to 1 in one point and equal to 0 in the other points of the element, the integral of an *edge basis function* is equal to 1 over one edge and equal to zero over all the others. Furthermore, assuming quadrilateral elements, we can define variables over surfaces and volumes using *nodal* and *edge basis functions*, and the tensor product.

In order to be able to develop a *mimetic* finite element method, two other "ingredients" are needed. Assuming that a variable  $u$  can be approximated in the following way:

$$u \approx \sum [u]_i \epsilon_i \quad , \quad (2.2)$$

the *reduction* ( $\mathcal{R}$ ) has been defined as the operator that maps  $u$  into  $[u]$ , while the *reconstruction* ( $\mathcal{I}$ ) as its right inverse. The vector of the coefficients  $[u]_i$  is called the *cochain*, [20].

---

<sup>3</sup>An element is a subspace of the domain. The intersection of any two elements is the boundary, a portion of it, or it is empty. The union of all the elements is equal to the domain. Such elements are computed by discretizing the domain.

In the following sections of this chapter, starting from the divergence and the curl operator, the geometry-variable association will be explained. The discrete counterpart of the continuous operators, called *incidence matrix* ( $\mathbb{E}$ ), will be introduced. *Inner* and *outer orientations* will derive naturally. *Nodal* and *edge basis functions* will be introduced for a 1-dimensional domain and, using the tensor product, generalised to a 2-dimensional one. On the same domain, the *reduction* and the *reconstruction* operator will be defined. Furthermore, the *wedge* and *mass matrices* will be computed from the definition of the *basis function*. At the end of the chapter, the building blocks, needed to develop a *mimetic* finite element method, will be known to the reader.

For these purposes, the domain is assumed to be 2-dimensional. This allows an easier representation of the domain and its discretization, without loosing generality in the mathematical derivation.

## 2.1. The divergence operator and its discrete counterpart

It has been underlined, at the beginning of this chapter, that the starting point of a *mimetic* finite element method may be traced back to the construction of a discrete counterpart of the divergence and the Stokes theorem. In this section, the divergence operator will be treated first because of its importance in the imposition of the incompressibility constraint.

Consider a domain, for example the one in Figure 2.1, the divergence theorem relates the volume integral of the divergence of a vector quantity,  $u$ , and the surface integral of the component of  $u$  normal to the boundary. Algebraically:

$$\int_{\Omega} \nabla \cdot \vec{u} \, d\Omega = \oint_{\partial\Omega} \vec{u} \cdot \vec{n} \, d\partial\Omega \quad . \quad (2.3)$$

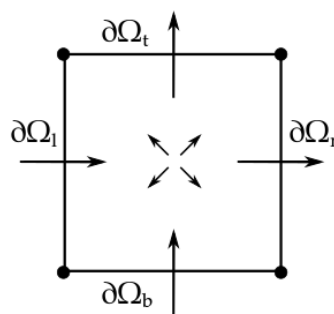


Figure 2.1: Outer-oriented 2-dimensional cell complex.

Figure 2.1 shows the 2-dimensional domain  $\Omega$ , which is essentially a *surface*; its boundary  $\partial\Omega$  consisting of four *lines*; and four corner *points*. *Surfaces*, *lines* and *points* represent the *space elements* of the domain  $\Omega$ . Furthermore, Figure 2.1 shows the orientations associated to them. The divergence theorem assumes the outflow as positive, so the *surface* is associated with the same orientation (indicated in the figure by the four arrows in the center pointing outward). Regarding the boundary lines, they are positive oriented if the flux through them is pointing rightward or upward as the divergence operator is in function of the flux entering or exiting the domain. This results in the definition of the *oriented cell complex* in Figure 2.1. This kind of orientation will be called *outer orientation* and, as explained, it is intrinsically connected to (2.3).

Taking into account the sign convention depicted in the same figure, (2.3) may be re-written dissociating the effect of each boundary:

$$\int_{\Omega} \nabla \cdot \vec{u} \, d\Omega = (-1) \int_{\partial\Omega_b} \vec{u} \cdot \vec{n} \, d\partial\Omega + (+1) \int_{\partial\Omega_t} \vec{u} \cdot \vec{n} \, d\partial\Omega + (-1) \int_{\partial\Omega_l} \vec{u} \cdot \vec{n} \, d\partial\Omega + (+1) \int_{\partial\Omega_r} \vec{u} \cdot \vec{n} \, d\partial\Omega \quad , \quad (2.4)$$

where the +1 and -1 coefficients are associated to the boundaries where surface and line orientations are pointing in the same or in the opposite direction, respectively.  $\partial\Omega_b$ ,  $\partial\Omega_t$ ,  $\partial\Omega_l$  and  $\partial\Omega_r$  indicate the top, bottom, left and right boundary in Figure 2.1.

From (2.4), the first variable-geometry duality is obtained. On the one hand the divergence of  $u$  is associated to the surface  $\Omega$ , on the other hand the flux of the velocity  $\vec{u} \cdot \vec{n}$  is coupled to the boundary lines  $\partial\Omega$ . The idea is, therefore, to discretize the divergence theorem using the integral of the above variables on the respective geometry. This integral will be called *cochain*, indicated with the brackets  $[\cdot]$ . Using the *cochains*, (2.4) becomes:

$$[\nabla \cdot u]^{(n)} = \mathbb{E}^{(n,n-1)} [u]^{(n-1)} \quad ^4 \quad , \quad (2.5)$$

where:

$$[\nabla \cdot u]^{(n)} = \int_{\Omega} \nabla \cdot \vec{u} \, d\Omega \quad , \quad (2.6)$$

$$[u]^{(n-1)} = \begin{pmatrix} \int_{\partial\Omega_b} \vec{u} \cdot \vec{n} \, d\partial\Omega \\ \int_{\partial\Omega_t} \vec{u} \cdot \vec{n} \, d\partial\Omega \\ \int_{\partial\Omega_l} \vec{u} \cdot \vec{n} \, d\partial\Omega \\ \int_{\partial\Omega_r} \vec{u} \cdot \vec{n} \, d\partial\Omega \end{pmatrix} \quad , \quad (2.7)$$

<sup>4</sup>The superscripts  $(n)$  and  $(n-1)$  indicate the dimension of each *space element* on which the cochains have been computed, where  $n$  is the dimension of the physical domain (i.e. In Figure 2.1,  $u$  is associated to the lines which are 1-dimensional. The physical domain is 2-dimensional hence  $n-1$  is equal to 1). The variable  $n$  is explicit for two reasons. On the one hand the formula is the same for physical domain of dimension 1 or 3, on the other hand is used to indicate that the cochain is *outer oriented*. Superscripts of cochains in which  $n$  does not appear are *inner oriented*.

and  $E^{(n,n-1)}$  is the matrix which takes into account the +1 and -1 coefficients ( $n$  is the dimension of the physical domain):

$$\mathbb{E}^{(n,n-1)} = [-1 + 1 - 1 + 1] \quad . \quad (2.8)$$

(2.6) and (2.7) describe the *reduction* operator. The *reduction* operator derives naturally from the divergence theorem, therefore it is unique.

More interesting is (2.8), where the incidence matrix -the discrete counterpart of the divergence operator- is shown. It is clearly metric free because it depends only on the topology of the *cell complex*.

Regarding the *mimetic* finite element method that we are going to developed in this thesis, two considerations may be underlined on the difference between it, the finite element method and the finite volume method:

- in a traditional finite element method only nodal basis functions are used, while the *mimetic* finite element method involves the usage of *nodal* and *edge basis functions* at the same time,
- the main difference between a finite volume and a mimetic method is the location of the variables. In the latter, variables are located in all the *space elements* of the discretization, while in the common FVM method variables are located in the centroid of the cell.

## 2.2. The curl operator and its discrete counterpart

Analogously to the divergence operator, the curl operator has its discrete mimetic counterpart. Starting from the algebraic definition of the Stokes' theorem

$$\int_{\Omega} \nabla \times u \, d\Omega = \oint_{\partial\Omega} \vec{u} \cdot \vec{t} \, d\partial\Omega \quad , \quad (2.9)$$

it is clear that a new orientation is needed for the *cell complex*. In this case, the integral of the curl of the vector field  $u$  is related to the integral of the component of  $u$  tangent to the boundary. Therefore, the following orientation is used and it will be referred in the future as *inner orientation*:

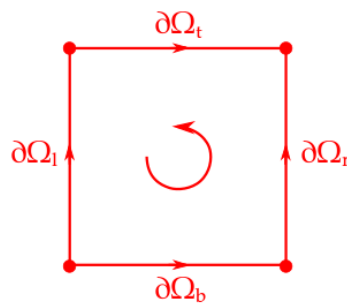


Figure 2.2: Inner-oriented 2-dimensional cell complex.

Using Figure 2.2, (2.9) may be re written as follows:

$$\int_{\Omega} \nabla \times u \, d\Omega = (+1) \int_{\partial\Omega_b} \vec{u} \cdot \vec{t} \, d\partial\Omega + (-1) \int_{\partial\Omega_t} \vec{u} \cdot \vec{t} \, d\partial\Omega + (-1) \int_{\partial\Omega_l} \vec{u} \cdot \vec{t} \, d\partial\Omega + (+1) \int_{\partial\Omega_r} \vec{u} \cdot \vec{t} \, d\partial\Omega \quad , \quad (2.10)$$

which, using the *cochains*, becomes:

$$[\nabla \times u]^{(2)} = \mathbb{E}^{(2,1)} [u]^{(1)} \quad . \quad (2.11)$$

In this case  $\mathbb{E}^{(2,1)}$  -the discrete counterpart of the curl operator- is equal to the following:

$$\mathbb{E}^{(2,1)} = [+1 -1 -1 +1] \quad . \quad (2.12)$$

Analogously to the discrete divergence operator, even the discrete curl operator depends only on the topology of the element. So it is metric independent.

It is interesting to notice that the vector field  $u$  in (2.3) and (2.9) may be the same. This leads to the fact that the user has to decide the appropriate orientation in function of the operator that will be applied later to the variable. Furthermore, it is clear the existence of an operator, called *Hodge- $\star$* , which maps  $[u]^{(n-1)}$  into  $[u]^{(1)}$  and vice versa. The dependence on the metric of the domain discretization is condensed into the *Hodge- $\star$*  matrix.

As both orientations are equally important, we are looking for an element, or an *oriented cell complex*, in which both of them are present.

### 2.3. The mimetic element and the associated basis functions

Aiming to combine *inner* and *outer orientations* in the same *oriented cell complex*, a primal-dual grid may be used. Using Figure 2.1, and associating each  $(n - k)$ -*space element* with its dual  $k$ -*space element*<sup>5</sup>, the following *oriented cell* may be created.

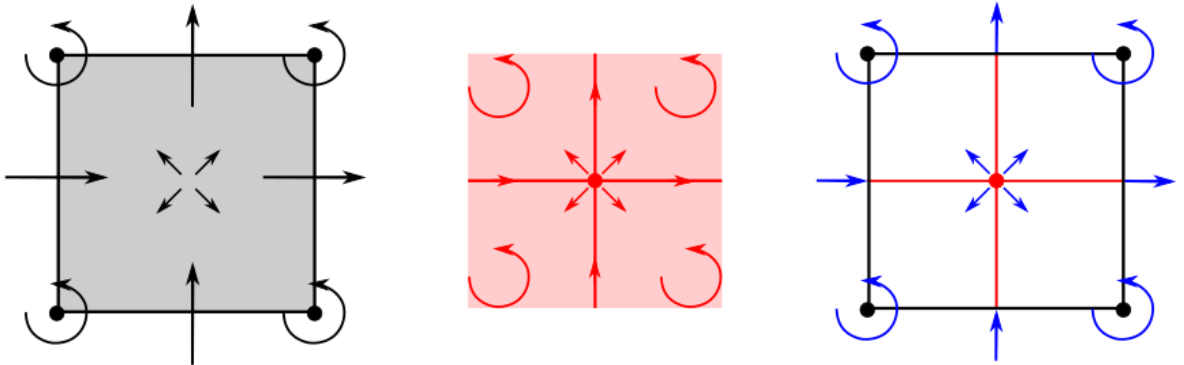


Figure 2.3: (left) primal outer oriented grid, (center) dual inner oriented grid, (right) oriented *cell complex*.

<sup>5</sup>i.e. associating each surface (2-dimensional *space element*) with a point (0-dimensional *space element*)

Figure 2.3 shows the complete *oriented cell complex* (right), which is the combination of the *outer oriented primal grid* (left) and the *dual inner oriented* (center). The *outer oriented* surface and the four *inner oriented* ones are shown using black and red shadows, respectively. The orientations of the *cell complex* (Figure 2.3,right) are depicted in blue in order to underline that each *space element* (for example the black surface) and its dual (the red point) have the same orientation. The *oriented cell complex* in the figure above will be referred as  $1^{st}$ -degree element for reasons that will be explained when the *basis functions* will be introduced.

Using an analogous reasoning, an element of degree greater than one may be constructed.

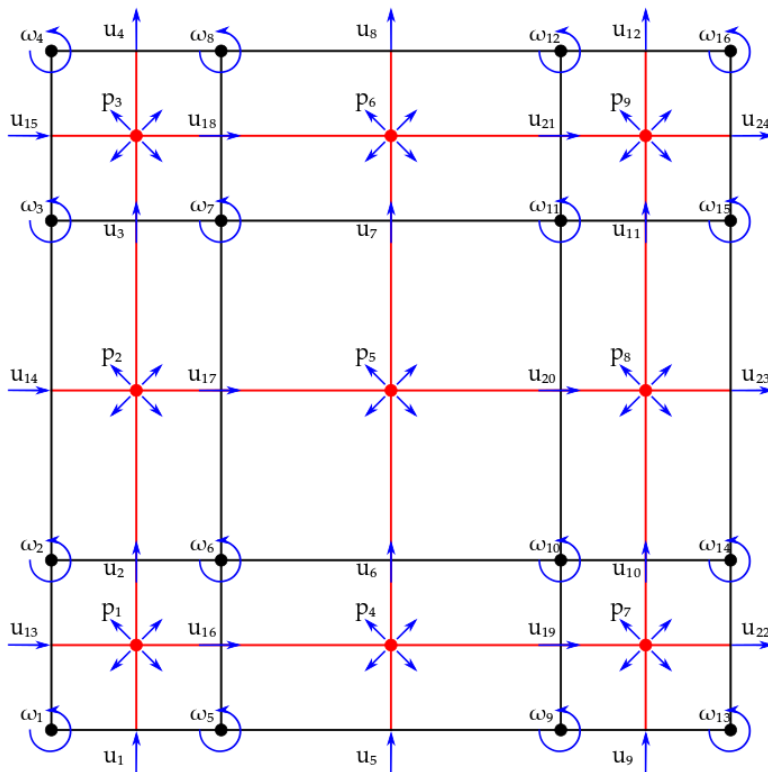


Figure 2.4:  $3^{rd}$ -degree element. Primal and dual grid are shown black and red. The variables  $-\omega, u, p$  may be associated to the primal points, lines and surfaces or to the dual surfaces, lines and points, respectively. Blue arrows show the orientation of each primal *space element* and its dual counterpart.

Figure 2.4 shows a  $3^{rd}$ -degree element. In the same figure, the *space elements* are labelled with the variable to which they will be associated in this thesis and numbered in order to unequivocally be able to refer to each of them. Considering  $\omega, u$  and  $p$  being associated with the primal points, lines and surfaces, the following *incidence matrices* may be computed:

$$\mathbb{E}^{(n,n-1)} = \begin{matrix} p_1 \\ p_2 \\ p_3 \\ p_4 \\ p_5 \\ p_6 \\ p_7 \\ p_8 \\ p_9 \end{matrix} \begin{pmatrix} u_1 & u_2 & u_3 & u_4 & u_5 & u_6 & u_7 & u_8 & u_9 & u_{10} & u_{11} & u_{12} & u_{13} & u_{14} & u_{15} & u_{16} & u_{17} & u_{18} & u_{19} & u_{20} & u_{21} & u_{22} & u_{23} & u_{24} \\ -1 & 1 & 0 & 0 & 0 & 0 & 0 & 0 & 0 & 0 & 0 & 0 & -1 & 0 & 0 & 1 & 0 & 0 & 0 & 0 & 0 & 0 & 0 & 0 \\ 0 & -1 & 1 & 0 & 0 & 0 & 0 & 0 & 0 & 0 & 0 & 0 & 0 & -1 & 0 & 0 & 1 & 0 & 0 & 0 & 0 & 0 & 0 & 0 \\ 0 & 0 & -1 & 1 & 0 & 0 & 0 & 0 & 0 & 0 & 0 & 0 & 0 & 0 & -1 & 0 & 0 & 1 & 0 & 0 & 0 & 0 & 0 & 0 \\ 0 & 0 & 0 & 0 & -1 & 1 & 0 & 0 & 0 & 0 & 0 & 0 & 0 & 0 & 0 & -1 & 0 & 0 & 1 & 0 & 0 & 0 & 0 & 0 \\ 0 & 0 & 0 & 0 & 0 & -1 & 1 & 0 & 0 & 0 & 0 & 0 & 0 & 0 & 0 & 0 & -1 & 0 & 0 & 1 & 0 & 0 & 0 & 0 \\ 0 & 0 & 0 & 0 & 0 & 0 & -1 & 1 & 0 & 0 & 0 & 0 & 0 & 0 & 0 & 0 & 0 & -1 & 0 & 0 & 1 & 0 & 0 & 0 \\ 0 & 0 & 0 & 0 & 0 & 0 & 0 & 0 & -1 & 1 & 0 & 0 & 0 & 0 & 0 & 0 & 0 & 0 & -1 & 0 & 0 & 1 & 0 & 0 \\ 0 & 0 & 0 & 0 & 0 & 0 & 0 & 0 & 0 & -1 & 1 & 0 & 0 & 0 & 0 & 0 & 0 & 0 & 0 & -1 & 0 & 0 & 1 & 0 \\ 0 & 0 & 0 & 0 & 0 & 0 & 0 & 0 & 0 & 0 & -1 & 1 & 0 & 0 & 0 & 0 & 0 & 0 & 0 & 0 & -1 & 0 & 0 & 1 \end{pmatrix} \quad (2.13)$$

$$\mathbb{E}^{(n-1,n-2)} = \begin{matrix} u_1 \\ u_2 \\ u_3 \\ u_4 \\ u_5 \\ u_6 \\ u_7 \\ u_8 \\ u_9 \\ u_{10} \\ u_{11} \\ u_{12} \\ u_{13} \\ u_{14} \\ u_{15} \\ u_{16} \\ u_{17} \\ u_{18} \\ u_{19} \\ u_{20} \\ u_{21} \\ u_{22} \\ u_{23} \\ u_{24} \end{matrix} \begin{pmatrix} \omega_1 & \omega_2 & \omega_3 & \omega_4 & \omega_5 & \omega_6 & \omega_7 & \omega_8 & \omega_9 & \omega_{10} & \omega_{11} & \omega_{12} & \omega_{13} & \omega_{14} & \omega_{15} & \omega_{16} \\ 1 & 0 & 0 & 0 & -1 & 0 & 0 & 0 & 0 & 0 & 0 & 0 & 0 & 0 & 0 & 0 \\ 0 & 1 & 0 & 0 & 0 & -1 & 0 & 0 & 0 & 0 & 0 & 0 & 0 & 0 & 0 & 0 \\ 0 & 0 & 1 & 0 & 0 & 0 & -1 & 0 & 0 & 0 & 0 & 0 & 0 & 0 & 0 & 0 \\ 0 & 0 & 0 & 1 & 0 & 0 & 0 & -1 & 0 & 0 & 0 & 0 & 0 & 0 & 0 & 0 \\ 0 & 0 & 0 & 0 & 1 & 0 & 0 & 0 & -1 & 0 & 0 & 0 & 0 & 0 & 0 & 0 \\ 0 & 0 & 0 & 0 & 0 & 1 & 0 & 0 & 0 & -1 & 0 & 0 & 0 & 0 & 0 & 0 \\ 0 & 0 & 0 & 0 & 0 & 0 & 1 & 0 & 0 & 0 & -1 & 0 & 0 & 0 & 0 & 0 \\ 0 & 0 & 0 & 0 & 0 & 0 & 0 & 1 & 0 & 0 & 0 & -1 & 0 & 0 & 0 & 0 \\ 0 & 0 & 0 & 0 & 0 & 0 & 0 & 0 & 1 & 0 & 0 & 0 & -1 & 0 & 0 & 0 \\ 0 & 0 & 0 & 0 & 0 & 0 & 0 & 0 & 0 & 1 & 0 & 0 & 0 & 0 & -1 & 0 \\ 0 & 0 & 0 & 0 & 0 & 0 & 0 & 0 & 0 & 0 & 1 & 0 & 0 & 0 & 0 & -1 \\ -1 & 1 & 0 & 0 & 0 & 0 & 0 & 0 & 0 & 0 & 0 & 0 & 0 & 0 & 0 & 0 \\ 0 & -1 & 1 & 0 & 0 & 0 & 0 & 0 & 0 & 0 & 0 & 0 & 0 & 0 & 0 & 0 \\ 0 & 0 & -1 & 1 & 0 & 0 & 0 & 0 & 0 & 0 & 0 & 0 & 0 & 0 & 0 & 0 \\ 0 & 0 & 0 & 0 & -1 & 1 & 0 & 0 & 0 & 0 & 0 & 0 & 0 & 0 & 0 & 0 \\ 0 & 0 & 0 & 0 & 0 & -1 & 1 & 0 & 0 & 0 & 0 & 0 & 0 & 0 & 0 & 0 \\ 0 & 0 & 0 & 0 & 0 & 0 & -1 & 1 & 0 & 0 & 0 & 0 & 0 & 0 & 0 & 0 \\ 0 & 0 & 0 & 0 & 0 & 0 & 0 & 0 & -1 & 1 & 0 & 0 & 0 & 0 & 0 & 0 \\ 0 & 0 & 0 & 0 & 0 & 0 & 0 & 0 & 0 & 0 & -1 & 1 & 0 & 0 & 0 & 0 \\ 0 & 0 & 0 & 0 & 0 & 0 & 0 & 0 & 0 & 0 & 0 & 0 & -1 & 1 & 0 & 0 \\ 0 & 0 & 0 & 0 & 0 & 0 & 0 & 0 & 0 & 0 & 0 & 0 & 0 & -1 & 1 & 0 \\ 0 & 0 & 0 & 0 & 0 & 0 & 0 & 0 & 0 & 0 & 0 & 0 & 0 & 0 & -1 & 1 \end{pmatrix} \quad (2.14)$$

Furthermore, it can be easily seen that considering  $p$ ,  $u$ , and  $\omega$  as the variables associated to the dual points, lines and surfaces respectively, the following identities holds:

$$\mathbb{E}^{(1,0)} = (\mathbb{E}^{(n,n-1)})^T, \quad (2.15)$$

$$\mathbb{E}^{(2,1)} = (\mathbb{E}^{(n-1,n-2)})^T. \quad (2.16)$$

Assuming a two dimensional domain, the gradient, curl and divergence operator have an exact discrete counterpart, which highly depends on the variable-geometry duality. The following scheme (2.17), using the notation used in Figure 2.4, summarized what we have said so far.

$$\begin{array}{ccccc} \omega^{(n-2)} & \xrightarrow[\mathbb{E}^{(n-1,n-2)}]{\nabla \times} & u^{(n-1)} & \xrightarrow[\mathbb{E}^{(n,n-1)}]{\nabla \cdot} & p^{(n)} & \textit{outer orientation} \\ \uparrow \star & & \uparrow \star & & \uparrow \star & \\ \omega^{(2)} & \xleftarrow[\mathbb{E}^{(2,1)}]{\nabla \times} & u^{(1)} & \xleftarrow[\mathbb{E}^{(1,0)}]{\nabla \cdot} & p^{(0)} & \textit{inner orientation} \end{array} \quad (2.17)$$

The scheme (2.17) may be considered an alternative form of the *De Rham complex* [20] (for a 2-dimensional domain) which relates *forms* using the *exterior derivative* and the *Hodge- $\star$*  operator.

### 2.3.1. Primal grid: basis functions, reconstruction and reduction operators

At this point, it is fundamental to define the basis function,  $\epsilon$ , belonging to the points  $\epsilon^{(n-2)}$ , lines  $\epsilon^{(n-1)}$  and surfaces  $\epsilon^{(n)}$  of the primal grid in Figure 2.4. With this objective in mind, it is fundamental to define the *nodal* and *edge basis function* on a 1-dimensional domain. Considering a 1-dimensional domain ( $x \in [-1; 1]$ ), the *Gauss-Lobatto-Legendre* points are used. These are the roots of the following equation:

$$(1 - x^2) \frac{dL_p(x)}{dx} = 0 \quad , \quad (2.18)$$

where  $L_p(x)$  indicates the Legendre polynomial of degree  $p$ . Having  $N$  points, it is possible to define  $N$  *nodal basis functions* of degree  $p = N - 1$ , which satisfy (2.1):

$$h_i(x) = \prod_{j=1, j \neq i}^{p+1} \frac{x - x_j}{x_i - x_j} \quad . \quad (2.19)$$

From (2.19), the *edge basis functions* may be constructed using the following formula [12]:

$$e_i(x) = - \sum_{k=1}^i \frac{dh_k(x)}{dx} \quad , \quad (2.20)$$

so that each  $e_i(x)$  satisfies the following property:

$$\int_{x_j}^{x_{j+1}} e_i(x) dx = \begin{cases} 1 & \text{if } i = j, \\ 0 & \text{if } i \neq j, \end{cases} \quad . \quad (2.21)$$

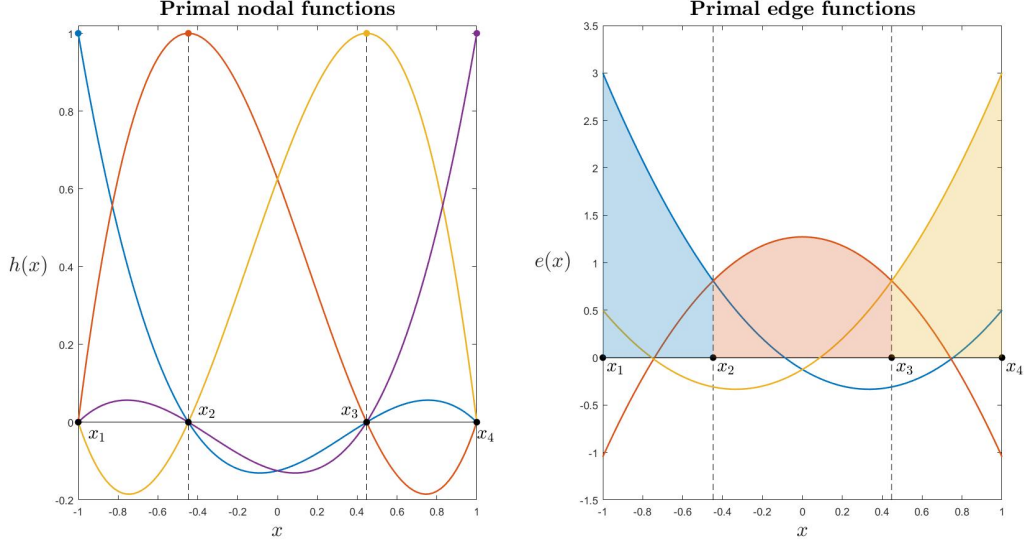


Figure 2.5: Primal *nodal* (left) and *edge basis functions* (right),  $N = 4$ . Circular marks are placed where  $h_i(x_i) = 1$  and  $\int_{x_i}^{x_{i+1}} e_i(x) dx = 1$  is shown with a coloured shadow.  $x_i$  represent the Lobatto points.

*Nodal* and *edge basis functions* are shown in Figure 2.5. It has to be noted that the former have been described by a third order polynomial degree, while the latter with a second order polynomial. Therefore, in the primal grid, the degree of the *edge functions* ( $p = N - 2$ ) is lower than the degree of the *nodal basis functions* ( $p = N - 1$ ).

Knowing the *nodal* and *edge basis functions* on a 1-dimensional domain, the basis functions on a 2-dimensional domain are constructed using the tensor product:

$$\epsilon_{j+N(i-1)}^{(n-2)}(x, y) = h_i(x)h_j(y) \quad i = 1, \dots, N \quad j = 1, \dots, N \quad , \quad (2.22)$$

$$\epsilon_{j+N(i-1)}^{(n-1)}(x, y) = e_i(x)h_j(y) \quad i = 1, \dots, N-1 \quad j = 1, \dots, N \quad , \quad (2.23)$$

$$\epsilon_{N(N-1)+j+(N-1)(i-1)}^{(n-1)}(x, y) = h_i(x)e_j(y) \quad i = 1, \dots, N \quad j = 1, \dots, N-1 \quad , \quad (2.24)$$

$$\epsilon_{j+(N-1)(i-1)}^{(n)}(x, y) = e_i(x)e_j(y) \quad i = 1, \dots, N-1 \quad j = 1, \dots, N-1 \quad , \quad (2.25)$$

where (2.23) and (2.24) describe the basis function attached to the horizontal and vertical lines, respectively.

The *reduction* ( $\mathcal{R}$ ) operator is defined as:

$$[\omega]_i^{(n-2)} = \omega(x_i) \quad i = 1, \dots, N^2 \quad , \quad (2.26)$$

$$[u]_i^{(n-1)} = \int_{e_i} \vec{u} \cdot \vec{n} dl \quad i = 1, \dots, 2N(N-1) \quad , \quad (2.27)$$

$$[p]_i^{(n)} = \int_{s_i} p \, d\Omega \quad i = 1, \dots, (N-1)^2 \quad , \quad (2.28)$$

where  $x$ ,  $e$  and  $s$  represent the points, lines and surfaces of the primal grid, the *reconstruction* ( $\mathcal{I}$ ) may be defined in the following way:

$$\omega^{(n-2)}(x, y) = \sum_{i=1}^{N^2} [\omega]^{(n-2)} \epsilon^{(n-2)}(x, y) \quad , \quad (2.29)$$

$$u^{(n-1)}(x, y) = \sum_{i=1}^{2N(N-1)} [u]^{(n-1)} \epsilon^{(n-1)}(x, y) \quad , \quad (2.30)$$

$$p^{(n)}(x, y) = \sum_{i=1}^{(N-1)^2} [p]^{(n)} \epsilon^{(n)}(x, y) \quad . \quad (2.31)$$

Figure 2.4 shows an oriented cell complex in which boundaries are discretized with 4 points ( $N = 4$ ). Being the basis functions associated with the primal points ( $\epsilon^{(n-2)}$ ) of 3<sup>rd</sup> order in  $x$  and  $y$  direction ( $p = N - 1$ ), the element in Figure 2.4 will be called 3<sup>rd</sup>-degree element. Analogously, Figure 2.3 (right) will be called 1<sup>st</sup>-degree element.

### 2.3.2. Dual grid: basis functions, reconstruction and reduction operators

Analogously to the construction of the primal basis functions  $\epsilon^{(n-2)}$ ,  $\epsilon^{(n-1)}$  and  $\epsilon^{(n)}$ , the dual basis functions, associated to the points, lines and surface of the dual (red, Figure 2.4) grid, may be computed. As the primal points were the *Gauss-Lobatto* points, the dual ones are the *Gauss* points which are the roots of the following equation:

$$L_p(x) = 0 \quad , \quad (2.32)$$

where  $L_p(x)$  indicates the Legendre polynomial of degree  $p$ .

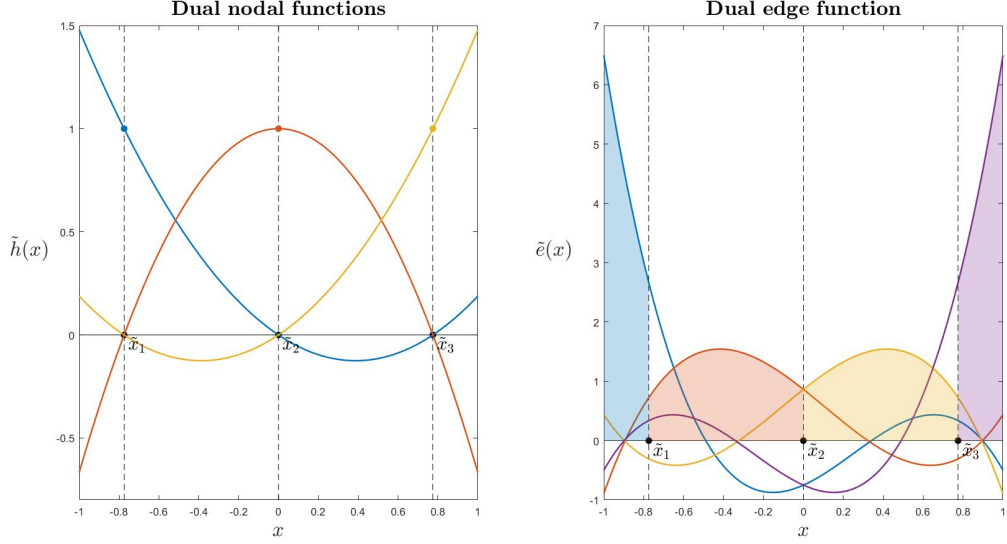


Figure 2.6: Dual *nodal* (left) and *edge basis functions* (right),  $N = 4$ . Circular marks are placed where  $h_i(x_i) = 1$  and  $\int_{\tilde{x}_i}^{\tilde{x}_{i+1}} e_i(x) dx = 1$  is shown with a coloured shadow.  $\tilde{x}_i$  represent the Gauss points.

Figure 2.6 shows the *nodal* (left) and *edge basis functions* (right) associated to the dual grid. As the primal functions, even the dual *basis functions* satisfy the properties (2.1) and (2.21) on the dual grid. Starting from the dual *nodal* and *edge functions* in a 1-dimensional domain (Figure 2.6), the *basis functions* on a 2-dimensional domain are constructed:

$$\epsilon_{j+(N-1)(i-1)}^{(0)}(x, y) = \tilde{h}_i(x)\tilde{h}_j(y) \quad i = 1, \dots, N-1 \quad j = 1, \dots, N-1 \quad , \quad (2.33)$$

$$\epsilon_{j+N(i-1)}^{(1)}(x, y) = \tilde{h}_i(x)\tilde{e}_j(y) \quad i = 1, \dots, N-1 \quad j = 1, \dots, N \quad , \quad (2.34)$$

$$\epsilon_{N(N-1)+j+(N-1)(i-1)}^{(1)}(x, y) = \tilde{e}_i(x)\tilde{h}_j(y) \quad i = 1, \dots, N-1 \quad j = 1, \dots, N \quad , \quad (2.35)$$

$$\epsilon_{j+N(i-1)}^{(2)}(x, y) = \tilde{e}_i(x)\tilde{e}_j(y) \quad i = 1, \dots, N \quad j = 1, \dots, N \quad , \quad (2.36)$$

Analogously to the primal grid, also on the dual one the *reduction* ( $\mathcal{R}$ ) operator is defined assuming  $p$ ,  $u$  and  $\omega$  as belonging to the dual points ( $\tilde{x}$ ), edge ( $\tilde{e}$ ) and surfaces ( $\tilde{s}$ ):

$$[p]_i^{(0)} = p(\tilde{x}_i) \quad i = 1, \dots, (N-1)^2 \quad , \quad (2.37)$$

$$[u]_i^{(1)} = \int_{\tilde{e}_i} \vec{u} \cdot \vec{t} dl \quad i = 1, \dots, 2N(N-1) \quad , \quad (2.38)$$

$$[\omega]_i^{(2)} = \int_{\tilde{s}_i} \omega d\Omega \quad i = 1, \dots, N^2 \quad . \quad (2.39)$$

The *reconstruction* ( $\mathcal{L}$ ) operator in the dual grid, is defined:

$$p^{(0)}(x, y) = \sum_{i=1}^{(N-1)^2} [p]_i^{(0)} \epsilon^{(0)}(x, y) \quad , \quad (2.40)$$

$$\mathbf{u}^{(1)}(x, y) = \sum_{i=1}^{2N(N-1)} [\mathbf{u}]^{(1)} \boldsymbol{\epsilon}^{(1)}(x, y) \quad , \quad (2.41)$$

$$\boldsymbol{\omega}^{(2)}(x, y) = \sum_{i=1}^{(N)^2} [\boldsymbol{\omega}]^{(2)} \boldsymbol{\epsilon}^{(2)}(x, y) \quad . \quad (2.42)$$

## 2.4. Wedge, mass and Hodge matrices

Let's assume to have  $\mathbf{a}^{(k)}$ ,  $\mathbf{a}^{(n-k)}$ ,  $\mathbf{b}^{(k)}$ ,  $\mathbf{b}^{(n-k)}$  defined as (2.29),(2.30),(2.31),(2.40),(2.41) or (2.42). We define the *wedge* ( $\wedge$ ) product between  $\mathbf{a}^{(k)}$  and  $\mathbf{b}^{(n-k)}$  as [6]:

$$\begin{aligned} \left( \mathbf{a}^{(k)}, \mathbf{b}^{(n-k)} \right) &= \int_{\Omega} \mathbf{a}^{(k)} \wedge \mathbf{b}^{(n-k)} \, d\Omega \\ &= [\mathbf{a}]^{(k)} \mathbb{W}^{(k,n-k)} [\mathbf{b}]^{(n-k)} \end{aligned} \quad \text{where} \quad \mathbb{W}_{i,j}^{(k,n-k)} = \int_{\Omega} \boldsymbol{\epsilon}_i^{(k)} \boldsymbol{\epsilon}_j^{(n-k)} \, d\Omega \quad . \quad (2.43)$$

The *wedge* matrix ( $\mathbb{W}^{(k,n-k)}$ ) defined in (2.43) is metric independent. Furthermore, from the definition of the *inner* product, the mass matrix may be derived [6]:

$$\begin{aligned} \langle \mathbf{a}^{(k)}, \mathbf{b}^{(k)} \rangle &= \int_{\Omega} \mathbf{a}^{(k)} \wedge \star \mathbf{b}^{(k)} \, d\Omega \\ &= [\mathbf{a}]^{(k)} \mathbb{M}^{(k)} [\mathbf{b}]^{(n-k)} \end{aligned} \quad \text{where} \quad \mathbb{M}_{i,j}^{(k)} = \int_{\Omega} \boldsymbol{\epsilon}_i^{(k)} \boldsymbol{\epsilon}_j^{(k)} \, d\Omega \quad . \quad (2.44)$$

The presence of the *Hodge- $\star$*  operator in the definition of the *inner product* suggests that the mass matrix ( $\mathbb{M}^{(k)}$ ) is metric dependent. This implies that it will change under mappings. Furthermore, it is clear that the *wedge* product, *inner* product and *Hodge* are not independent. The definition of the *Hodge- $\star$*  matrix, may be written as a function of the *wedge* and the *mass* matrices. Assuming that  $\mathbf{b}^{(k)} = \star \mathbf{b}^{(n-k)}$ , it is clear that:

$$\begin{aligned} \left( \mathbf{a}^{(n-k)}, \mathbf{b}^{(k)} \right) &= \int_{\Omega} \mathbf{a}^{(n-k)} \wedge \mathbf{b}^{(k)} \, d\Omega = \int_{\Omega} \mathbf{a}^{(n-k)} \wedge \star \mathbf{b}^{(n-k)} \, d\Omega = \langle \mathbf{a}^{(n-k)}, \mathbf{b}^{(n-k)} \rangle \\ [\mathbf{a}]^{(n-k)} \mathbb{W}^{(n-k,k)} [\mathbf{b}]^{(k)} &= [\mathbf{a}]^{(n-k)} \mathbb{M}^{(n-k)} [\mathbf{b}]^{(n-k)} \\ \mathbb{W}^{(n-k,k)} [\mathbf{b}]^{(k)} &= \mathbb{M}^{(n-k)} [\mathbf{b}]^{(n-k)} \\ [\mathbf{b}]^{(k)} &= \left( \mathbb{W}^{(n-k,k)} \right)^{-1} \mathbb{M}^{(n-k)} [\mathbf{b}]^{(n-k)} \end{aligned} \quad , \quad (2.45)$$

so the *Hodge- $\star$*  matrix may be computed:

$$\mathbb{H}^{(k,n-k)} = \left( \mathbb{W}^{(n-k,k)} \right)^{-1} \mathbb{M}^{(n-k)} \quad . \quad (2.46)$$

When a primal and dual grid is employed, the *Hodge* is a square and invertible matrix [5] so

$$\mathbb{H}^{(n-k,k)} = \left( \mathbb{H}^{(k,n-k)} \right)^{-1} \quad . \quad (2.47)$$

It is clear from (2.46) that the *Hodge* matrix is the multiplication of a metric-independent matrix ( $\mathbb{W}$ ) and a metric-dependent one ( $\mathbb{M}$ ). With the objective of simplifying the matrix formulation, it is useful to define a new set of *dual basis function* for which the *wedge* matrix is the identity matrix.

### 2.4.1. Algebraic-dual basis functions

The development and the mathematical description of what will be referred as *algebraic-dual basis functions* has been conducted in [15]. Analogously to Sections 2.3.1 and 2.3.2, first the *algebraic-dual basis functions* will be defined on a 1-dimensional domain and then arranged in order to create the 2-dimensional *basis functions*.

*Nodal algebraic-dual basis functions* may be computed using the following equation:

$$\tilde{\Psi}^{(0)}(x) = \Psi^{(1)} \left( \mathbb{M}_1^{(1)} \right)^{-1} , \quad (2.48)$$

where  $\mathbb{M}_1^{(1)}$  is the *mass matrix* associated with the *primal edge polynomial*  $e(x)$

$$\mathbb{M}_1^{(1)} \quad i,j = \int_{-1}^{+1} e_i(x) e_j(x) dx , \quad (2.49)$$

$\Psi^{(1)} = [e_1(x), \dots, e_{N-1}(x)]$  and  $\tilde{\Psi}^{(0)} = [\tilde{h}_1(x), \dots, \tilde{h}_{N-1}(x)]$ . Using the same reasoning, *edge algebraic-dual basis functions* are given by:

$$\tilde{\Psi}^{(1)}(x) = \Psi^{(0)} \left( \mathbb{M}_1^{(0)} \right)^{-1} , \quad (2.50)$$

where:

$$\mathbb{M}_1^{(0)} \quad i,j = \int_{-1}^{+1} h_i(x) h_j(x) dx , \quad (2.51)$$

$\Psi^{(0)} = [h_1(x), \dots, h_N(x)]$  and  $\tilde{\Psi}^{(1)} = [\tilde{e}_1(x), \dots, \tilde{e}_N(x)]$ .

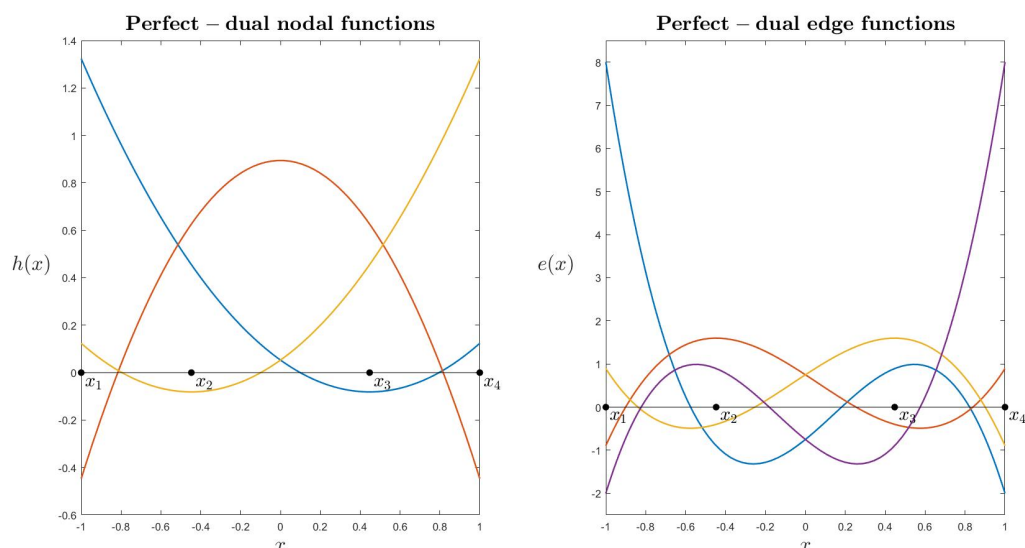


Figure 2.7: Algebraic-dual *nodal* (left) and *edge basis functions* (right),  $N = 4$ .  $x_i$  represent the Lobatto points.

Figure 2.7 shows the *nodal* (left) and *edge* (right) *algebraic-dual basis functions*. As can be seen, they resemble the *dual basis functions* depicted in Figure 2.6. Furthermore, it can be seen that they do not satisfy (2.1) and (2.21); as a consequence, the geometrical connection is lost.

However, the usage of the *algebraic-dual basis function* leads to an easier matrix formulation. Starting from the dual *nodal* ( $\tilde{\epsilon}$ ) and *edge* ( $\tilde{h}$ ) *basis functions*,  $\epsilon^{(0)}$ ,  $\epsilon^{(1)}$  and  $\epsilon^{(2)}$  may be computed using (2.33), (2.34), (2.35) and (2.36). Using the *perfect-dual basis functions*, the computation of the *mass*, *wedge* and *hodge* matrices becomes easier. They are equal to the following [15]:

$$\mathbb{M}^{(k)} = \left( \mathbb{M}^{(n-k)} \right)^{-1} , \quad (2.52)$$

$$\mathbb{W}^{(k,n-k)} = I , \quad (2.53)$$

$$\mathbb{H}^{(k,n-k)} = \mathbb{M}^{(n-k)} , \quad (2.54)$$

where  $I$  is the identity matrix.

Having lost the geometrical connection in the definition of the dual basis functions ( $\epsilon^{(0)}$ ,  $\epsilon^{(1)}$  and  $\epsilon^{(2)}$ ), it is necessary to use the *hodge* matrix to evaluate the dual cochains:

$$[a]^{(k)} = \mathbb{M}^{(n-k)} [a]^{(n-k)} , \quad (2.55)$$

where  $[a]^{(n-k)}$  is defined in (2.26), (2.27) and (2.28). The *reconstruction* ( $\mathcal{I}$ ) is performed in the same way as for the *dual basis functions* in (2.40), (2.41) and (2.42).

In the following chapters only the *primal* and the *algebraic-dual basis functions* will be used. For simplicity, the term *algebraic* will sometimes be omitted.



# 3

## The vector Laplace equation

When engineers and mathematicians try to implement new numerical schemes, first, they try to implement them on simple problems. In particular, referring to numerical schemes able to solve partial differential equations, the word simple refers both to the equations and the domain on which they are solved.

The simplest set of equations that have a meaningful aerodynamic application are the *Stokes equations*. As introduced in the first chapter, the Stokes equations describe flows characterized by a low Reynolds number.

In order to further simplify the problem, at first the *vector Laplace* equation will be solved in this thesis. As suggested by Arnold, Falk & Gopalakrishnan [2] the study of the hybrid formulation of the *vector Laplace* equation is strictly connected to the solution of the *Stokes equation* using a pressure-vorticity-velocity hybrid formulation. Attention is given to the choice of stable and consistent finite dimensional spaces [1]. Furthermore, they studied both natural and essential boundary condition proving an optimal convergence for the former and a sub-optimal convergence for the latter.

### 3.1. From the Stokes to the Laplace equation

In this chapter attention will be given to the *vector Laplace* equation. This derives from the fact that its fully-mixed formulation is very close to the mixed formulation of the Stokes equation for

incompressible flows (3.1, 3.2).

$$\begin{cases} \nabla \cdot \vec{u} = 0 \\ \nabla p - \mu \nabla^2 \vec{u} = f \end{cases} . \quad (3.1)$$

Using the vector identity of the Laplace operator:

$$\nabla^2 \vec{u} = \nabla(\nabla \cdot \vec{u}) - \nabla \times \nabla \times \vec{u} \quad , \quad (3.2)$$

substituting it into (3.2) and using (3.1), the *Stokes equation* for incompressible flows takes the following form:

$$\begin{cases} \nabla \cdot \vec{u} = 0 \\ \nabla p + \mu \nabla \times \nabla \times \vec{u} = f \end{cases} . \quad (3.4)$$

From (3.4) and (3.5), the mixed-formulation can be easily derived:

$$\begin{cases} -\nabla \cdot \vec{u} = 0 \\ \omega \quad -\nabla \times \vec{u} = 0 \\ \nabla p \quad + \mu \nabla \times \omega = f \end{cases} , \quad (3.5)$$

which, assuming  $\mu = 1$  and imposing  $p = \nabla \cdot \vec{u}$ , resembles the fully mixed formulation of the *vector Laplace equation*:

$$\begin{cases} p \quad -\nabla \cdot \vec{u} = 0 \\ \omega \quad -\nabla \times \vec{u} = 0 \\ \nabla p \quad -\nabla \times \omega = f \end{cases} . \quad (3.6)$$

It is preferable to study the vector Laplace equation instead of the Stokes equation for its properties, such as *positiveness* and *symmetry*, which will be characteristic even for the associated finite element formulation.

Furthermore, E. Tonti [27] used geometrical arguments to describe that even the stationary thermal conduction, the electric conduction and the electrostatic field can be all described by the Laplace equation. In other words, it can be stated that the mathematical operators and the geometrical features, in which the variables live, are strongly linked together.

### 3.2. Variable-geometry association

In Chapter 2 it has been explained how the association between mesh geometries -also called *space elements*- and variables is fundamental in a *mimetic* finite element method. In the same chapter,

it has been underlined how the partial differential operator, that has to be applied to the variable, dictates on which *space element* the variable has to be placed.

Recalling the fully mixed formulation of the vector Laplace equation:

$$\begin{cases} p & -\nabla \cdot \vec{u} & = & 0 \\ & \omega & -\nabla \times \vec{u} & = & 0 \\ \nabla p & -\nabla \times \omega & & = & f \end{cases} , \quad (3.8)$$

it can be noticed that both the divergence and the curl operator have to be applied to the velocity variable  $\vec{u}$ . Whether  $\vec{u}$  has to be associated to the outer oriented edges ( $u^{(n-2)}$ ) or to the inner oriented ones ( $u^{(1)}$ ) will dictate whether the velocity vector could be pointwise divergence-free (incompressible flow) or curl-free (irrotational flow).

For their importance in engineering practice, we would like to focus on incompressible flows. For this purpose, the vector field  $\vec{u}$  will be discretized as a velocity flux through the primal outer-oriented edges  $u^{(n-1)}$ . In order to prove the possibility to impose exactly the divergence free constraint using  $u^{(n-1)}$ , we have to define a new operator. This *projection operator* ( $\pi_\star$ ) is equal to the following:

$$\pi_\star = \mathcal{IR} \quad . \quad (3.9)$$

One of the properties of the *projection operator* is that it can commute with the divergence operator. The following diagram commutes

$$\begin{array}{ccc} u & \xrightarrow{\nabla \cdot} & p \\ \downarrow \pi_\star & & \downarrow \pi_\star \\ u^{(n-1)} & \xrightarrow{\mathbb{E}^{(n,n-1)}} & p^{(n)} \end{array} , \quad (3.10)$$

which proves that the solution  $u^{(n-1)}$  is pointwise divergence free when  $p = 0$  [19].

Therefore, the variable  $u$  is associated to the outer oriented edges

$$u \longrightarrow u^{(n-1)} = \sum [u]^{(n-1)} \epsilon^{(n-1)} \quad . \quad (3.11)$$

Furthermore, using the *De Rham complex* (2.17), it is clear to associate  $p$  to the primal outer-oriented surfaces and  $\omega$  to the primal outer-oriented points

$$p \longrightarrow p^{(n)} = \sum [p]^{(n)} \epsilon^{(n)} \quad , \quad (3.12)$$

$$\omega \longrightarrow \omega^{(n-2)} = \sum [\omega]^{(n-2)} \epsilon^{(n-2)} \quad . \quad (3.13)$$

Figure 3.1 shows the mimetic element that derives from this reasoning. The three variables  $\omega$ ,  $u$  and  $p$  are associated to the primal (black) points, lines and surfaces, respectively. Furthermore, the figure underlines their *outer orientations*.

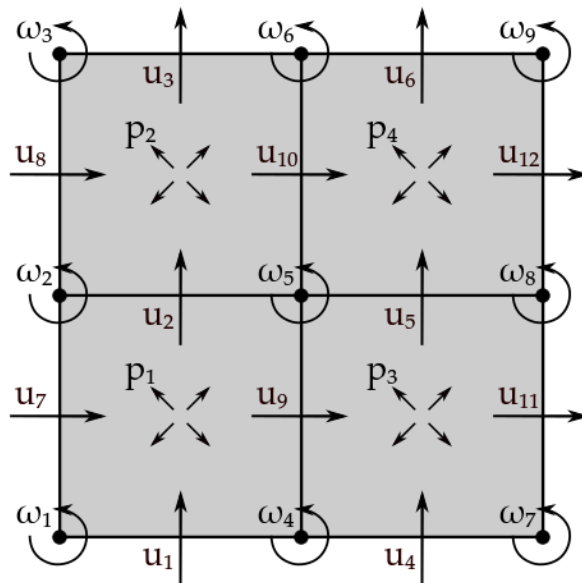


Figure 3.1: Continuous primal element. The variables  $\omega^{(n-2)}$ ,  $u^{(n-1)}$  and  $p^{(n)}$  are associated to the points, lines and surfaces of the primal grid, respectively. Arrows show the *outer orientations*.

The mixed formulation of the vector Laplace equation (3.8) may be re-written using the variable-geometry duality as follows:

$$\begin{cases} p^{(n)} & -\nabla \cdot u^{(n-1)} & = & 0 \\ & \omega^{(n-2)} & -\nabla^* \times u^{(n-1)} & = & 0 \\ \nabla^* p^{(n)} & -\nabla \times \omega^{(n-2)} & & = & f \end{cases}, \quad (3.14)$$

where  $\nabla^* \times$  and  $\nabla^*$  indicate the curl and the gradient operator, which, according to the *De Rham complex* (2.17), cannot be applied directly to  $u^{(n-1)}$  and  $p^{(n)}$ , respectively.

### 3.3. Weak and matrix formulation

In the previous section, (3.11), (3.12), (3.13) it has been underlined how the unknown variables are approximated by a finite number of polynomial basis functions. Using the theory developed in [7], it can be said that  $p^{(n)}$ ,  $u^{(n-1)}$  and  $\omega^{(n-2)}$  belong to  $L^2(\Omega)$ ,  $H(\text{div}, \Omega)$  and  $H(\text{curl}, \Omega)$ , respectively.  $L^2(\Omega)$  defines the square integrable functions over the domain  $\Omega$ , while  $H(\text{div}, \Omega)$  and  $H(\text{curl}, \Omega)$  are defined as follows:

$$H(\text{div}; \Omega) := \{u \mid u \in L^2(\Omega), \nabla \cdot u \in L^2(\Omega)\} \quad ,$$

$$H(\text{curl}; \Omega) := \{\omega \mid \omega \in L^2(\Omega), \nabla \times \omega \in L^2(\Omega)\} \quad .$$

Starting from the mixed formulation (3.14) and applying the Galerkin's method, the weak formulation may be stated as follows: for a given  $f \in L^2(\Omega)$ , find  $p \in L^2(\Omega)$ ,  $u \in H(\text{div}, \Omega)$  and  $\omega \in H(\text{curl}, \Omega)$ , such that:

$$\begin{aligned} \langle \epsilon^{(n)}, p^{(n)} \rangle & - \langle \epsilon^{(n)}, \nabla \cdot u^{(n-1)} \rangle & = & 0 \\ \langle \epsilon^{(n-2)}, \omega^{(n-2)} \rangle & - \langle \epsilon^{(n-2)}, \nabla^* \times u^{(n-1)} \rangle & = & 0 \\ \langle \epsilon^{(n-1)}, \nabla^* p^{(n)} \rangle & - \langle \epsilon^{(n-1)}, \nabla \times \omega^{(n-2)} \rangle & = & \langle \epsilon^{(n-1)}, f^{(n-1)} \rangle \end{aligned} \quad , \quad (3.15)$$

$\forall \epsilon^{(n)} \in L^2(\Omega)$ ,  $\forall \epsilon^{(n-2)} \in H(\text{curl}, \Omega)$  and  $\forall \epsilon^{(n-1)} \in H(\text{div}, \Omega)$ .

From Chapter 2, it is clear how to convert an *inner product*  $\langle \cdot, \cdot \rangle$  to its matrix formulation (2.44), how to apply the divergence operator to  $u^{(n-1)}$  ( $\mathbb{E}^{(n, n-1)}$ ) and the curl operator to  $\omega^{(n-2)}$  ( $\mathbb{E}^{(n-1, n-2)}$ ). The only missing pieces are the matrix evaluation of  $\langle \epsilon^{(n-2)}, \nabla^* \times u^{(n-1)} \rangle$  and  $\langle \epsilon^{(n-1)}, \nabla^* p^{(n)} \rangle$ . These may be evaluated using integration by parts (C.1) and (C.2). Therefore, the matrix formulation takes the following form:

$$\begin{aligned} \langle \epsilon^{(n)}, p^{(n)} \rangle & - \langle \epsilon^{(n)}, \nabla \cdot u^{(n-1)} \rangle & = & 0 \\ \langle \epsilon^{(n-2)}, \omega^{(n-2)} \rangle & - \langle \nabla \times \epsilon^{(n-2)}, u^{(n-1)} \rangle & = & \int_{\partial\Omega} \epsilon^{(n-2)} \cdot \vec{t} u \, d\partial\Omega \\ - \langle \nabla \cdot \epsilon^{(n-1)}, p^{(n)} \rangle & - \langle \epsilon^{(n-1)}, \nabla \times \omega^{(n-2)} \rangle & = & \langle \epsilon^{(n-1)}, f^{(n-1)} \rangle - \int_{\partial\Omega} \epsilon^{(n-1)} \cdot \vec{n} p^{(n)} \, d\partial\Omega \end{aligned} \quad . \quad (3.16)$$

From the weak formulation, assuming  $p = 0$  and  $\vec{u} \cdot \vec{t} = 0$  on  $\partial\Omega^1$ , the following matrix formulation may be computed:

$$\begin{bmatrix} \mathbb{M}^{(n)} & 0 & -\mathbb{M}^{(n)} \mathbb{E}^{(n, n-1)} \\ 0 & \mathbb{M}^{(n-2)} & -(\mathbb{M}^{(n-1)} \mathbb{E}^{(n-1, n-1)})^T \\ -(\mathbb{M}^{(n)} \mathbb{E}^{(n, n-1)})^T & -\mathbb{M}^{(n-1)} \mathbb{E}^{(n-1, n-2)} & \end{bmatrix} \begin{pmatrix} [p]^{(n)} \\ [\omega]^{(n-2)} \\ [u]^{(n-1)} \end{pmatrix} = \begin{pmatrix} 0 \\ 0 \\ \mathbb{M}^{(n-1)} [f]^{(n-1)} \end{pmatrix} \quad . \quad (3.17)$$

The matrix formulation above will be referred as *primal* matrix formulation, in which the word "primal" underlines that all the variables  $-p, \omega, u-$  are associated to the grid having the same name.

Looking at (3.17), two simplifications may be made. Firstly,  $\mathbb{M}^{(n)}$  may be simplified from the first column and moved to multiply  $[p]^{(n)}$ , secondly the first row may be multiplied by  $(\mathbb{M}^{(n)})^{-1}$ . This yields to the following matrix formulation:

$$\begin{bmatrix} (\mathbb{M}^{(n)})^{-1} & 0 & -\mathbb{E}^{(n, n-1)} \\ 0 & \mathbb{M}^{(n-2)} & -(\mathbb{M}^{(n-1)} \mathbb{E}^{(n-1, n-1)})^T \\ -(\mathbb{E}^{(n, n-1)})^T & -\mathbb{M}^{(n-1)} \mathbb{E}^{(n-1, n-2)} & \end{bmatrix} \begin{pmatrix} \mathbb{M}^{(n)} [p]^{(n)} \\ [\omega]^{(n-2)} \\ [u]^{(n-1)} \end{pmatrix} = \begin{pmatrix} 0 \\ 0 \\ \mathbb{M}^{(n-1)} [f]^{(n-1)} \end{pmatrix} \quad . \quad (3.18)$$

<sup>1</sup>  $p = 0$  and  $\vec{u} \cdot \vec{t} = 0$  will be referred as *natural* or *electric* boundary conditions [2].

What seems to be just a numerical simplification hides the transition towards a *primal-dual* grid formulation. Recalling that  $\mathbb{M}^{(n)} [p]^{(n)} = [p]^{(0)}$  (2.55), it can be said that the variable  $p^{(0)}$  has been moved to the points of the dual grid.

Figure 3.2 shows the collocation of the primal (black) and dual (red) variables on the element. In this case the variable  $p^{(0)}$  is associated to dual points and equipped with an *inner* orientation.

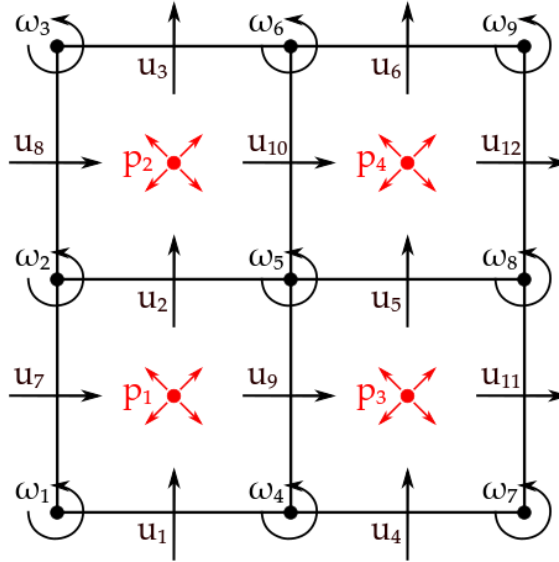


Figure 3.2: Continuous primal-dual element. The variables  $\omega^{(n-2)}$  and  $u^{(n-1)}$  are associated to the points and lines of the primal (black) grid, respectively. The variable  $p$  is associated to the dual (red) points. Black arrows denote an *outer orientation*, while the red ones an *inner orientation*.

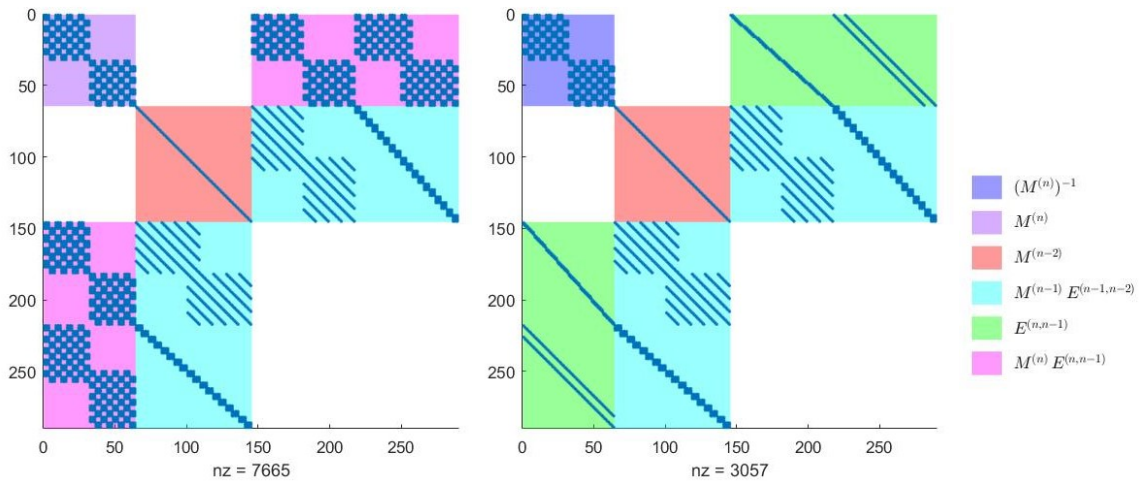


Figure 3.3: Sparsity structure of the LHS in (3.17) (left) and in (3.18) (right).  $2 \times 2$  grid,  $4^{th}$  order elements.

Figure 3.3 compares the matrix derived from the *primal* formulation (3.17) and the one from the

*primal-dual* (3.18) formulation. It can be seen that the *primal-dual* formulation leads to a matrix which is much more sparse. Considering a  $2 \times 2$  grid of  $4^h$  order elements, the non zero entries decrease from 7665 in the *primal* formulation to 3057 in the *primal-dual* one. This is beneficial for reducing the solution time and the computer memory needed to store such matrix.

As a result of the transition of the variable  $p$  from the primal outer-oriented surfaces to the dual inner-oriented points, a new weak formulation has to be derived. The updated weak formulation may be stated: for a given  $f \in L^2(\Omega)$ , find  $p \in L^2(\Omega)$ ,  $u \in H(\text{div}, \Omega)$  and  $\omega \in H(\text{curl}, \Omega)$ , such that:

$$\begin{aligned}
 \langle \epsilon^{(0)}, p^{(0)} \rangle & - \langle \epsilon^{(0)}, \nabla \cdot u^{(n-1)} \rangle & = & 0 \\
 \langle \epsilon^{(n-2)}, \omega^{(n-2)} \rangle & - \langle \nabla \times \epsilon^{(n-2)}, u^{(n-1)} \rangle & = & \int_{\partial\Omega} \epsilon^{(n-2)} u \cdot \vec{t} \, d\partial\Omega \\
 - \langle \nabla \cdot \epsilon^{(n-1)}, p^{(0)} \rangle & - \langle \epsilon^{(n-1)}, \nabla \times \omega^{(n-2)} \rangle & = & \langle \epsilon^{(n-1)}, f^{(n-1)} \rangle - \int_{\partial\Omega} \epsilon^{(n-1)} p^{(0)} \, d\partial\Omega
 \end{aligned} \quad , \tag{3.19}$$

$\forall \epsilon^{(0)} \in L^2(\Omega)$ ,  $\forall \epsilon^{(n-2)} \in H(\text{curl}, \Omega)$  and  $\forall \epsilon^{(n-1)} \in H(\text{div}, \Omega)$ .

The formulation (3.18) has been verified using the method of the manufactured solution. The verifications proved that it optimally converges to the exact solution as a function of the the number of elements.

In Appendix B contour plots of the variables  $p$ ,  $\omega$  and  $u$  will be shown together with  $h$ -convergence and  $p$ -convergence plots. Furthermore, a further analysis on the sparsity of the system as a function of the numerical computation of  $\mathbb{M}^{(n-2)}$  and  $\mathbb{M}^{(n-1)}$  has been conducted. As a result, it was proven that even though the matrix elements are not computed exactly, they are close enough to the exact ones to have an optimal convergence.



# 4

## Discontinuous approach

During the last years, several discontinuous finite element methods have been developed. Their advantages range from a higher degree of parallelism to the higher-order approximation in comparison with the standard Finite Volume methods. Furthermore, due to their discontinuity, different polynomial degrees may be used on different elements [10].

It is appropriate to mention, for their similarities with the method that will be developed along this thesis, the Interior Penalty method and the Mortar method. The former derives from the weakly imposition of the Diricklet boundary conditions developed by Lions [3] and then modified by Nitsche [4] to ensure consistency. Inter-element continuity can be obtained in the same fashion. The latter is described by D. A. Kopriva as the imposition of the continuity on conformal and non-conformal meshes through one-dimensional constructs called *mortars* [17]. This method was developed for staggered meshes in which only edges need a continuity constraint. Furthermore, it was underlined that *special corner algorithms must be devised to ensure correct propagation of waves through the corners* [18]. An attempt of doing so was performed by the same D. A. Kopriva using the multidomain Chebyshev spectral collocation method [16]. Three kind of point-intersections are studied (subdomain-subdomain point, subdomain-wall point and cross point) and treated differently in the numerical method.

A similar approach to the one that will be presented in this thesis was developed by B. Cockburn et. al. in 2000 [14]. Based on the traditional finite element method on triangular meshes, Cockburn et. al. wrote a mixed formulation for the Lagrange multipliers called tangential velocity-pressure

formulation. Analogously to the previous research, authors found difficulties in treating mesh corners. Their solution consists in the elimination of one edge for every vertex in order to generate a non-singular system. This method, therefore, sacrifices the topology equality of all elements.

The following chapter will describe the development of a fully discontinuous hybrid mimetic finite element method in which both edges and points are discontinuous.

### 4.1. The discontinuous element

In the previous chapter the mimetic finite element was shown which consist of a primal grid (depicted in black) and a dual one (red). The continuity of the elements did not require any particular treatment of the element boundary, which, in a discontinuous case, is vital to transfer information between elements.

For this purpose, the following element will be used:

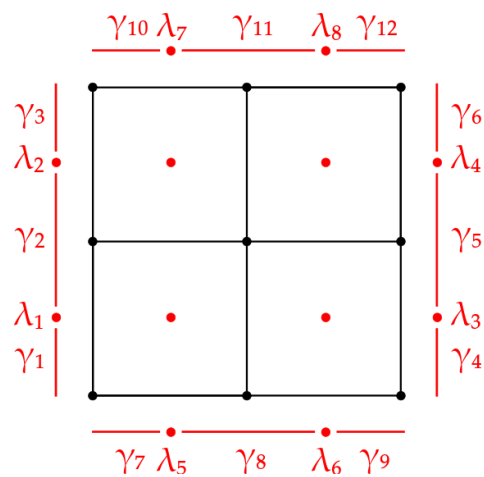


Figure 4.1: Element with embedded boundary.

Figure 4.1 shows the element used for the hybrid discontinuous approach in which degrees of freedom are added at the boundary. They are the dual (in a one-dimensional sense) of the (black) primal boundary considering the four boundaries (top, bottom, left and right) separately. Belonging to the dual grid, they are described by the sets of dual basis functions for points and edges, which will be called  $\lambda$  and  $\gamma$ , respectively. The development of the hybrid discontinuous finite element methods, therefore, comes down to the creation of a finite element method in which the boundary degrees of freedom are continuous.

It is fundamental to understand the function spaces in which the physical variables ( $u$ ,  $\omega$ ,  $p$ ) and the *Lagrange multipliers* ( $\lambda, \gamma$ ) lie.

Let  $\Omega_K$  being the partition into elements of the physical domain  $\Omega$ , such that  $\Omega = \bigcup_{i=1}^K \Omega_i$ . Analogously to the continuous case, using discontinuous elements,  $u^{(n-1)}$  belongs to a function space similar to  $H(\text{div})$ . In this case, a broken Sobolev space has to be defined:

$$H(\text{div}; \Omega_K) := \{u \mid u \in L^2(\Omega) \mid u|_{\Omega_i} \in H(\text{div}; \Omega_i), \forall \Omega_i\} \equiv \prod_{i=1}^K H(\text{div}; \Omega_i),$$

so that  $u \in H(\text{div}; \Omega_K)$ . The same reasoning may be applied to the variable  $\omega$

$$H(\text{curl}; \Omega_K) := \{\omega \mid \omega \in L^2(\Omega) \mid \omega|_{\Omega_i} \in H(\text{curl}; \Omega_i), \forall \Omega_i\} \equiv \prod_{i=1}^K H(\text{curl}; \Omega_i),$$

so that  $\omega \in H(\text{curl}; \Omega_K)$ , while  $p \in L^2(\Omega)$ .

More difficult is the definition of the function spaces in which the interface *Lagrange multipliers* lie. First, let's focus on  $\lambda$ , which is defined on the red boundary points in Figure 4.1. The theory developed in [7] suggests that the restriction on the boundary of  $H(\text{div}; \Omega_i)$  is  $H^{-\frac{1}{2}}(\partial\Omega_i)$ . Its dual counterpart,  $\lambda$ , lies in the dual space  $H^{\frac{1}{2}}(\partial\Omega_i)$ . Therefore, the following holds:

$$H^{\frac{1}{2}}(\partial\Omega_K) = \bigcup_{i=1}^K H^{\frac{1}{2}}(\partial\Omega_i).$$

Thus,  $\lambda \in H^{\frac{1}{2}}(\partial\Omega_K)$ . The (red) edge *Lagrange multiplier* called  $\gamma$ , instead, lies in the space  $H^{-\frac{1}{2}}(\partial\Omega_i)$  [13]. So the broken Sobolev space can be defined as follows:

$$H^{-\frac{1}{2}}(\partial\Omega_K) = \bigcup_{i=1}^K H^{-\frac{1}{2}}(\partial\Omega_i).$$

#### 4.1.1. Inter-element flux continuity

Recalling that the velocity fluxes are the degrees of freedom coupled to the edges of the primal grid, imposing the flux continuity geometrically means to impose the continuity between neighbouring edges. The dual element to the edges in the boundary, i.e. the red points depicted in the boundary of Figure 4.1, will be used to achieve this goal. A graphical representation can be seen in the following figure, in which the global numbering is used.

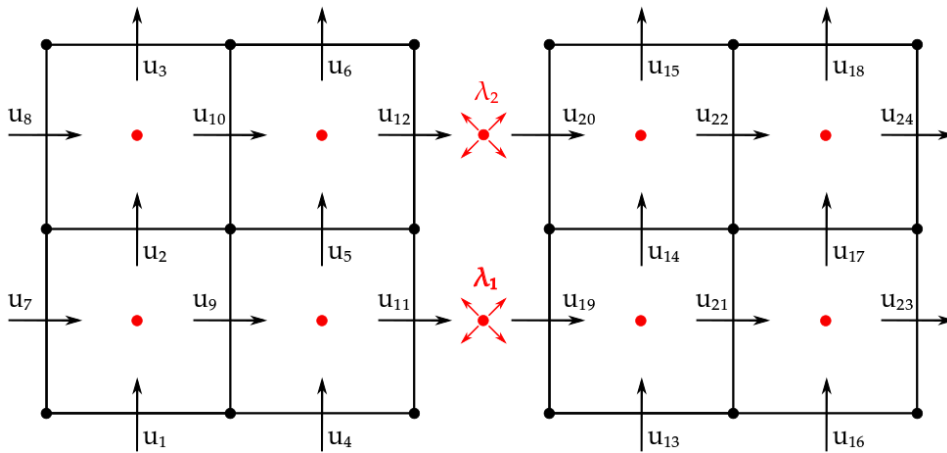


Figure 4.2: Flux continuity

For example the inter-element flux continuity is achieved when

$$u_{19} - u_{11} = 0 \quad . \quad (4.1)$$

The continuity constraint may be imposed using a boundary variable  $\lambda$  as *Lagrange multiplier* in the following way:

$$\int_{\partial K \setminus \partial \Omega} \lambda \llbracket u \rrbracket \, d\partial\Omega = 0 \quad , \quad (4.2)$$

where  $\llbracket \cdot \rrbracket$  indicates the jump between neighbouring edges (i.e.  $\llbracket u \rrbracket = u_R - u_L$ ). Applying (4.2) to the case in figure 4.2, two equations, as the number of *Lagrange multipliers*, may be written:

$$(-1)\lambda_1 u_{11} + (+1)\lambda_1 u_{19} = 0 \quad , \quad (4.3)$$

$$(-1)\lambda_1 u_{12} + (+1)\lambda_1 u_{20} = 0 \quad . \quad (4.4)$$

Analogously to the divergence theorem, the +1 and -1 coefficients may be written in matrix formulation. This will be called  $\mathbb{E}^{(\lambda, n-1)}$ , for this reason (4.2) may be written in the following matrix formulation:

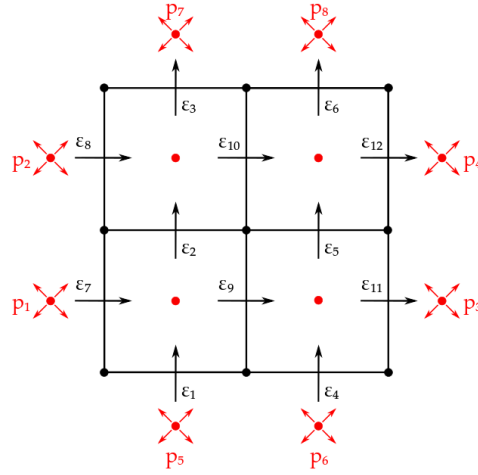
$$[\lambda] \mathbb{E}^{(\lambda, n-1)} [u] = 0 \quad . \quad (4.5)$$

The usage of the letter  $\mathbb{E}$  was not randomly chosen. The duality pairing between  $\lambda$  and  $u$  is metric free (topological).

Additionally, another physical interpretation of the matrix  $\mathbb{E}^{(\lambda, n-1)}$  can be found. The third equation of the mixed formulation (3.19) after the integration by parts can be modified for discontinuous elements:

$$-(\nabla \cdot \epsilon^{(n-1)}, p^{(0)}) - \langle \epsilon^{(n-1)}, \nabla \times \omega^{(n-2)} \rangle + \int_{\partial K \setminus \partial \Omega} \epsilon^{(n-1)} p^{(0)} = \langle \epsilon^{(n-1)}, f^{(n-1)} \rangle - \int_{\partial \Omega} \epsilon^{(n-1)} p^{(0)} \quad , \quad (4.6)$$

so that the resemblance between the third term and (4.2) may be seen. In this case, the basis functions,  $\epsilon$ , belong to the edges of the primal grid while  $p$  to the dual points on the boundary as shown in the following figure:

Figure 4.3: Lagrange multiplier  $\lambda$ : local numbering.

Using the local numbering of the *Lagrange multiplier* in Figure 4.3, the following local  $\mathbb{E}^{(p,n-1)}$  can be written:

$$\mathbb{E}^{(p,n-1)} = \begin{matrix} & \begin{matrix} \epsilon_1 & \epsilon_2 & \epsilon_3 & \epsilon_4 & \epsilon_5 & \epsilon_6 & \epsilon_7 & \epsilon_8 & \epsilon_9 & \epsilon_{10} & \epsilon_{11} & \epsilon_{12} \end{matrix} \\ \begin{matrix} p_1 \\ p_2 \\ p_3 \\ p_4 \\ p_5 \\ p_6 \\ p_7 \\ p_8 \end{matrix} & \begin{bmatrix} 0 & 0 & 0 & 0 & 0 & 0 & 1 & 0 & 0 & 0 & 0 & 0 \\ 0 & 0 & 0 & 0 & 0 & 0 & 0 & 1 & 0 & 0 & 0 & 0 \\ 0 & 0 & 0 & 0 & 0 & 0 & 0 & 0 & 0 & 0 & -1 & 0 \\ 0 & 0 & 0 & 0 & 0 & 0 & 0 & 0 & 0 & 0 & 0 & -1 \\ 1 & 0 & 0 & 0 & 0 & 0 & 0 & 0 & 0 & 0 & 0 & 0 \\ 0 & 0 & 0 & 1 & 0 & 0 & 0 & 0 & 0 & 0 & 0 & 0 \\ 0 & 0 & -1 & 0 & 0 & 0 & 0 & 0 & 0 & 0 & 0 & 0 \\ 0 & 0 & 0 & 0 & 0 & -1 & 0 & 0 & 0 & 0 & 0 & 0 \end{bmatrix} \end{matrix} . \quad (4.7)$$

which, rearranged in order to construct the global matrix, turns out to be equal to  $\mathbb{E}^{(\lambda,n-1)}$ . It follows that the third term in (4.6) can be written using the following matrix formulation:

$$\int_{\partial K \setminus \partial \Omega} \epsilon^{(n-1)} p = [\epsilon]^{(n-1)} (\mathbb{E}^{(\lambda,n-1)})^T [p] . \quad (4.8)$$

Therefore, the matrix  $\mathbb{E}^{(\lambda,n-1)}$  has two physical explanations. Comparing Figure 4.2 and 4.3 it can be noticed that both  $p$  and  $\lambda$  belong to the red points located in the boundary. This suggests that the *Lagrange multiplier*  $\lambda$  is not only a mathematical quantity but it has even a physical meaning:  $\lambda$  describes the variable  $p$  on the element boundaries.

This statement, which derives from the variable-geometry duality and the variational formulation in (4.6), will be numerically confirmed in Chapter 5.

### 4.1.2. Inter-element point continuity

Looking back at the continuous case, it is worth to recall that the vorticity,  $\omega$ , is the variable associated to the points of the primal mesh. Using the same procedure analysed in the previous section, dual boundary variables ( $\gamma$ ) are added at the boundary as it is depicted in the following figure:

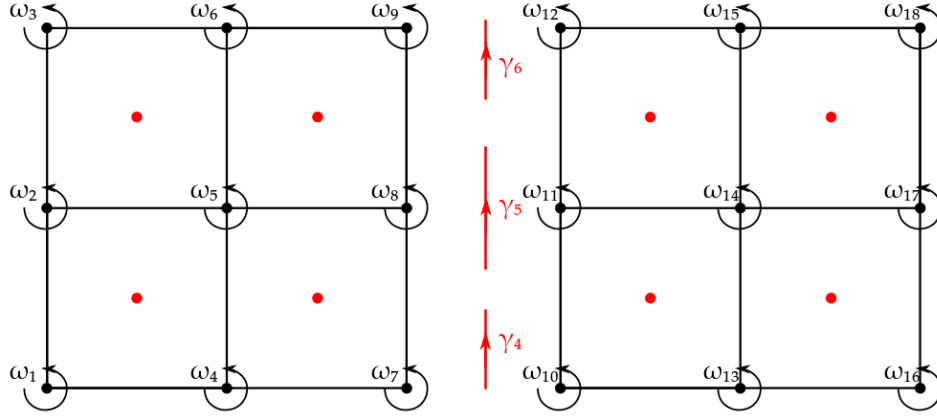


Figure 4.4: Point continuity.

The vorticity-continuity may be imposed using the following formula

$$\int_{\partial K \setminus \partial \Omega} \gamma [\omega] \, d\partial \Omega = 0 \quad , \quad (4.9)$$

which, for the case depicted in Figure 4.4, originates three equations as the number of  $\gamma$  Lagrange multipliers:

$$(+1)\gamma_4\omega_7 + (-1)\gamma_4\omega_{10} = 0 \quad (4.10)$$

$$(+1)\gamma_5\omega_8 + (-1)\gamma_5\omega_{11} = 0 \quad (4.11)$$

$$(+1)\gamma_6\omega_9 + (-1)\gamma_6\omega_{12} = 0 \quad . \quad (4.12)$$

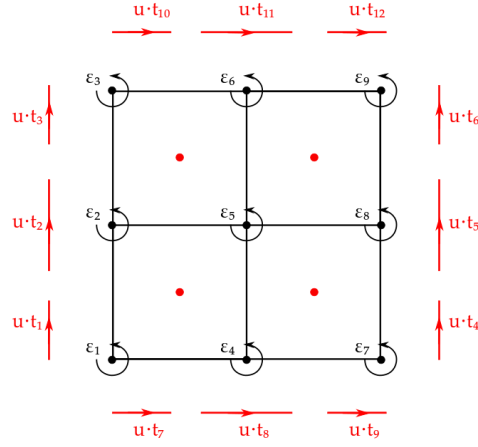
which can be translated into the following matrix formulation:

$$\int_{\partial K \setminus \partial \Omega} \gamma [\omega] \, d\partial \Omega = [\gamma] \mathbb{E}^{(\gamma, n-2)} [\omega] \quad . \quad (4.13)$$

The matrix  $\mathbb{E}^{(\gamma, n-2)}$  arises even in the mixed formulation of the *vector Laplace* equation. After the integration by parts and the modification for discontinuous elements, the second equation of the mixed formulation (3.19) leads to the following:

$$\langle \epsilon^{(n-2)}, \omega^{(n-2)} \rangle - \langle \nabla \times \epsilon^{(n-2)}, u^{(n-1)} \rangle - \int_{\partial K \setminus \partial \Omega} \epsilon^{(n-2)} u \cdot \vec{t} \, d\partial \Omega = \int_{\partial \Omega} \epsilon^{(n-2)} u \cdot \vec{t} \, d\partial \Omega \quad . \quad (4.14)$$

The third term resembles (4.9) where  $\epsilon^{(n-2)}$  belongs to the points of the primal grid (as  $\omega$ ) and  $u \cdot \vec{t}$  belongs to the dual edges in the boundary (as  $\gamma$ ). Using the following local numbering for  $u \cdot \vec{t}$ , the matrix (4.15) may be written.

Figure 4.5: Lagrange multiplier  $\gamma$ : local numbering.

$$\mathbb{E}(u \cdot \vec{t}, n-2) = \begin{matrix} & \epsilon_1^{(n-2)} & \epsilon_2^{(n-2)} & \epsilon_3^{(n-2)} & \epsilon_4^{(n-2)} & \epsilon_5^{(n-2)} & \epsilon_6^{(n-2)} & \epsilon_7^{(n-2)} & \epsilon_8^{(n-2)} & \epsilon_9^{(n-2)} \\ \begin{matrix} u \cdot \vec{t}_1 \\ u \cdot \vec{t}_2 \\ u \cdot \vec{t}_3 \\ u \cdot \vec{t}_4 \\ u \cdot \vec{t}_5 \\ u \cdot \vec{t}_6 \\ u \cdot \vec{t}_7 \\ u \cdot \vec{t}_8 \\ u \cdot \vec{t}_9 \\ u \cdot \vec{t}_{10} \\ u \cdot \vec{t}_{11} \\ u \cdot \vec{t}_{12} \end{matrix} & \begin{bmatrix} -1 & 0 & 0 & 0 & 0 & 0 & 0 & 0 & 0 & 0 \\ 0 & -1 & 0 & 0 & 0 & 0 & 0 & 0 & 0 & 0 \\ 0 & 0 & -1 & 0 & 0 & 0 & 0 & 0 & 0 & 0 \\ 0 & 0 & 0 & 0 & 0 & 0 & 1 & 0 & 0 & 0 \\ 0 & 0 & 0 & 0 & 0 & 0 & 0 & 1 & 0 & 0 \\ 0 & 0 & 0 & 0 & 0 & 0 & 0 & 0 & 1 & 0 \\ 1 & 0 & 0 & 0 & 0 & 0 & 0 & 0 & 0 & 0 \\ 0 & 0 & 0 & 1 & 0 & 0 & 0 & 0 & 0 & 0 \\ 0 & 0 & 0 & 0 & 0 & 0 & 1 & 0 & 0 & 0 \\ 0 & 0 & -1 & 0 & 0 & 0 & 0 & 0 & 0 & 0 \\ 0 & 0 & 0 & 0 & 0 & -1 & 0 & 0 & 0 & 0 \\ 0 & 0 & 0 & 0 & 0 & 0 & 0 & 0 & 0 & -1 \end{bmatrix} \end{matrix} \quad (4.15)$$

$\mathbb{E}(u \cdot \vec{t}, n-2)$  turns out to be equal to  $\mathbb{E}(\gamma, n-2)$ . The inter-element boundary term in (4.14) may be written using the following matrix formulation:

$$\int_{\partial K \setminus \partial \Omega} \epsilon^{(n-2)} u \cdot \vec{t} \, d\partial \Omega = [\epsilon]^{(n-2)} (\mathbb{E}(\gamma, n-2))^T [u \cdot \vec{t}] \quad . \quad (4.16)$$

Therefore, analogously to the *Lagrange multiplier*  $\lambda$ , even  $\gamma$  has an associated physical meaning, which is the tangential velocity to the element boundary,  $u \cdot \vec{t}$ . Assuming an orthogonal grid,  $\gamma$ , in order to comply to the above mentioned physical meaning, should converge to  $u_x$  for the top and bottom boundaries and to  $u_y$  for the left and the right ones.

## 4.2. Variational formulation: discontinuous elements

Starting from (3.7), multiplying by the correct test function and integration by parts, the following variational formulation may be written for discontinuous elements:

$$\begin{aligned}
\langle \epsilon^{(0)}, p^{(0)} \rangle & - (\epsilon^{(0)}, \nabla \cdot u^{(n-1)}) & = & 0 \\
\langle \epsilon^{(n-2)}, \omega^{(n-2)} \rangle & - \langle \nabla \times \epsilon^{(n-2)}, u^{(n-1)} \rangle & - \int_{\partial K \setminus \partial \Omega} \epsilon^{(n-2)} u \cdot \vec{t} \, d\partial \Omega & = & \int_{\partial \Omega} \epsilon^{(n-2)} u \cdot \vec{t} \, d\partial \Omega \\
-(\nabla \cdot \epsilon^{(n-1)}, p^{(0)}) & - \langle \epsilon^{(n-1)}, \nabla \times \omega^{(n-2)} \rangle & + \int_{\partial K \setminus \partial \Omega} \epsilon^{(n-1)} p^{(0)} \, d\partial \Omega & = & \langle \epsilon^{(n-1)}, f^{(n-1)} \rangle - \int_{\partial \Omega} \epsilon^{(n-1)} p^{(0)} \, d\partial \Omega
\end{aligned} \tag{4.17}$$

Taking into account that  $p^{(0)} = \lambda$  and  $u \cdot \vec{t} = \gamma$  in  $\partial K \setminus \partial \Omega$ , two additional boundary variables born. To ensure the resolvability of the system of equations, as many equations as the number of  $\lambda$  and  $\gamma$  have to be appended to the system. These are (4.2) and (4.9). Adding them to (4.17), leads to the variational formulation for fully discontinuous elements:

$$\begin{aligned}
\langle \epsilon^{(0)}, p^{(0)} \rangle & - (\epsilon^{(0)}, \nabla \cdot u^{(n-1)}) & = & 0 \\
\langle \epsilon^{(n-2)}, \omega^{(n-2)} \rangle & - \langle \nabla \times \epsilon^{(n-2)}, u^{(n-1)} \rangle & - \int_{\partial K \setminus \partial \Omega} \epsilon^{(n-2)} \gamma \, d\partial \Omega & = & \int_{\partial \Omega} \epsilon^{(n-2)} u \cdot \vec{t} \, d\partial \Omega \\
-(\nabla \cdot \epsilon^{(n-1)}, p^{(0)}) & - \langle \epsilon^{(n-1)}, \nabla \times \omega^{(n-2)} \rangle & + \int_{\partial K \setminus \partial \Omega} \epsilon^{(n-1)} \lambda \, d\partial \Omega & = & \langle \epsilon^{(n-1)}, f^{(n-1)} \rangle - \int_{\partial \Omega} \epsilon^{(n-1)} p^{(0)} \, d\partial \Omega \\
& & + \int_{\partial K \setminus \partial \Omega} \lambda \llbracket u \rrbracket \, d\partial \Omega & = & 0 \\
& & - \int_{\partial K \setminus \partial \Omega} \gamma \llbracket \omega \rrbracket \, d\partial \Omega & = & 0
\end{aligned} \tag{4.18}$$

The variational formulation (4.18) can be translated into the following matrix formulation using the inner product, the wedge product (discussed in Chapter 2) and the boundary integrals discussed in the previous sections:

$$\begin{bmatrix} (\mathbb{M}^{(n)})^{-1} & 0 & -\mathbb{E}^{(n,n-1)} & 0 & 0 \\ 0 & \mathbb{M}^{(n-2)} & -(\mathbb{M}^{(n-1)}\mathbb{E}^{(n-1,n-1)})^T & 0 & -(\mathbb{E}^{\gamma^{n-2}})^T \\ -(\mathbb{E}^{(n,n-1)})^T & -\mathbb{M}^{(n-1)}\mathbb{E}^{(n-1,n-2)} & 0 & (\mathbb{E}^{\lambda^{n-1}})^T & 0 \\ 0 & 0 & \mathbb{E}^{\lambda^{n-1}} & 0 & 0 \\ 0 & -\mathbb{E}^{\gamma^{n-2}} & 0 & 0 & 0 \end{bmatrix} \begin{pmatrix} [p]^{(0)} \\ [\omega]^{(n-2)} \\ [u]^{(n-1)} \\ [\lambda] \\ [\gamma] \end{pmatrix} = \begin{pmatrix} 0 \\ [\gamma_B] \\ \mathbb{M}^{(n-1)} [f]^{(n-1)} - [\lambda_B] \\ 0 \\ 0 \end{pmatrix} \quad (4.19)$$

The matrix formulation (4.19) is singular, as Cockburn et. al. [14] found, and the number of singular modes is coincident with the number of points where four or more elements come together. In the following section, an innovative way to deal with this problem will be presented.

### 4.3. Cross-intersections: a non-singular system

Completely discontinuous elements create cross-intersections (shown in Figure 4.6) which, if not treated correctly, generate a singular system. Contrary to Cockburn et. al. [14] (Appendix E), in this thesis singularities are avoided adding a new *Lagrange multiplier* ( $\theta$ ) in the middle of each cross-intersection. Its graphical representation and sign convention can be seen in Figure 4.6.

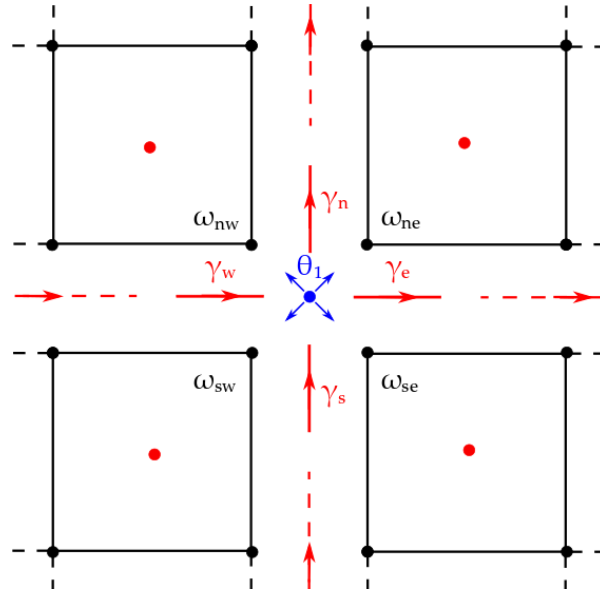


Figure 4.6: Cross-intersection: local numbering.

The idea is that  $\theta$ , instead of being a point singularity in which information born (source) or die (sink), is a non-singular point in which information are transferred. Influx and outflux must balance

each other. This idea leads to the following equation (using the sign convention in Figure 4.6):

$$(-1)\gamma_n + (+1)\gamma_e + (-1)\gamma_s + (+1)\gamma_w = 0 \quad , \quad (4.20)$$

which, multiplied by a test function  $\theta$  and integrated along the element boundary, yields the following integral equation:

$$\int_C \theta \llbracket \gamma \rrbracket = 0 \quad , \quad (4.21)$$

where  $\llbracket \gamma \rrbracket$  indicates the LHS of (4.20) and  $C$  is the cross-intersection point depicted in Figure 4.6. Analogously to the previous cases, taking into account that  $\theta$  is a 0-dimensional volume in the primal grid and that  $\lambda$  is the described by the perfect dual functions, (4.21) can be written using the following matrix formulation:

$$\int_C \theta \llbracket \gamma \rrbracket = [\theta] \mathbb{E}^{(\theta\gamma)} [\gamma] \quad , \quad (4.22)$$

where  $\mathbb{E}^{(\theta\gamma)}$  is the topological matrix that takes into account the coefficients in (4.20).

In order to maintain the symmetry of the numerical method, (4.9) has to be modified in the following way:

$$\int_{\partial K \setminus \partial \Omega} \gamma \llbracket \omega \rrbracket d\partial\Omega - \int_C \gamma \theta = 0 \quad . \quad (4.23)$$

The *Lagrange multiplier*  $\theta$  differs from  $\lambda$  and  $\gamma$  because it does not appear in the variational formulation of the physical equations (4.17). This makes the physical interpretation of  $\theta$  quite difficult. An attempt in this direction can be made looking at the equations (4.23) using the numbering in Figure 4.6:

$$\begin{aligned} \gamma_n (\omega_{nw} - \omega_{ne}) + \gamma_n \theta_1 &= 0 \\ \gamma_e (\omega_{ne} - \omega_{se}) + \gamma_e \theta_1 &= 0 \\ \gamma_s (\omega_{sw} - \omega_{se}) + \gamma_s \theta_1 &= 0 \\ \gamma_w (\omega_{nw} - \omega_{sw}) + \gamma_w \theta_1 &= 0 \end{aligned} \quad . \quad (4.24)$$

From (4.24) we can conclude that the *Lagrange multiplier*  $\theta$  will not effect the continuity of the vorticity in the intersection points only if it will be equal or it will converge to zero. The value of  $\theta$  and its effects on the overall solution will be analysed in the next chapter.

#### 4.4. Domain discretization

In the previous sections it has been explained how the *Lagrange multipliers*,  $\lambda$  and  $\gamma$ , have been used to impose the continuity between elements.

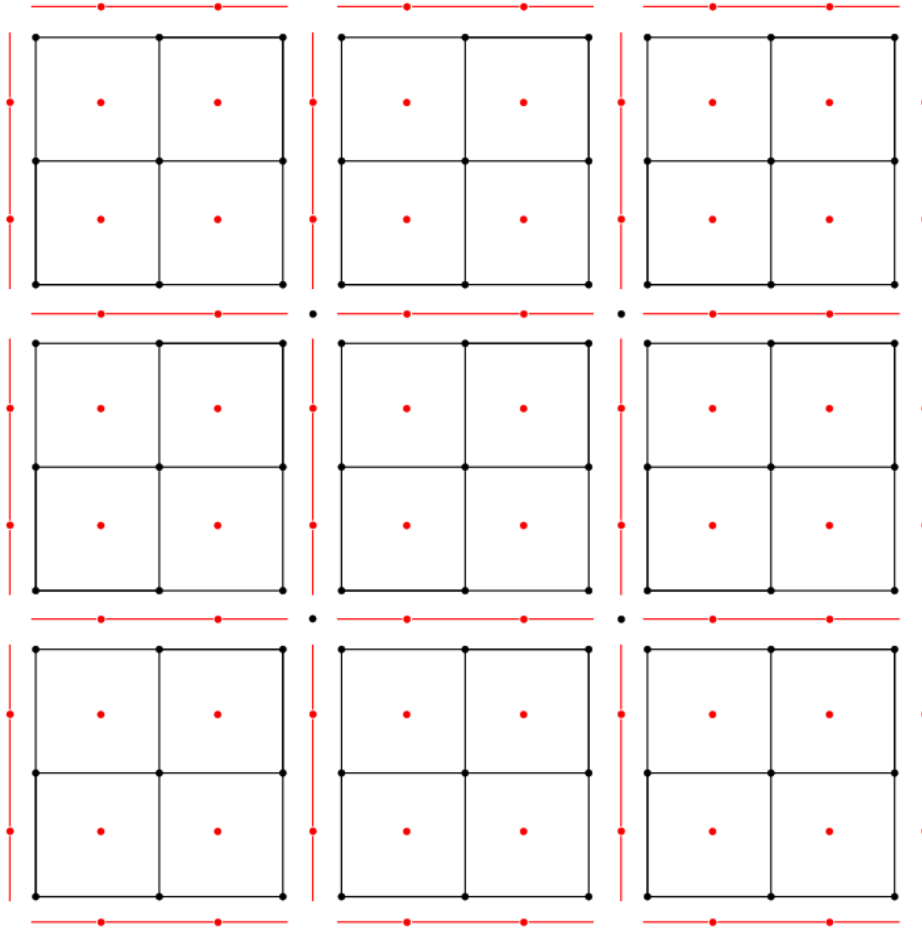


Figure 4.7: Position of the *Lagrange multipliers* on a  $3 \times 3$  grid of  $2^{nd}$  order elements.  $\lambda$  is represented by red points on the boundary of the elements,  $\gamma$  by the red lines and  $\theta$  by the black points in the intersections. Each element may be seen in Figure 4.1.

Figure 4.7 shows the discretization of a squared physical domain with a  $3 \times 3$  grid of  $2^{nd}$ -order elements. The figure underlines the location of the *Lagrange multipliers* which are positioned along horizontal and vertical lines. This explains why in Chapter 5 and 6 *Lagrange multipliers* are reconstructed along horizontal and vertical lines.

## 4.5. Non-singular variational formulation

Adding (4.21) and its transposed term (4.23) into the variational formulation (4.18), the final variational problem, which takes into account the discontinuities among elements and the use of *Lagrange multipliers*, may be stated as follows: for a given  $f \in L^2(\Omega_K)$ , find  $u \in H(div; \Omega_K)$ ,  $p \in L^2(\Omega)$ ,  $\omega \in H(curl; \Omega_K)$ ,  $\lambda \in H^{\frac{1}{2}}(\partial\Omega_K)$  and  $\gamma \in H^{-\frac{1}{2}}(\partial\Omega_K)$ , such that:

$$\begin{aligned}
\langle \epsilon^{(0)}, p^{(0)} \rangle &= -(\epsilon^{(0)}, \nabla \cdot u^{(n-1)}) &= 0 \\
\langle \epsilon^{(n-2)}, \omega^{(n-2)} \rangle &= -\langle \nabla \times \epsilon^{(n-2)}, u^{(n-1)} \rangle - \int_{\partial K \setminus \partial \Omega} \epsilon^{(n-2)} \gamma \, d\partial \Omega &= \int_{\partial \Omega} \epsilon^{(n-2)} u \cdot \vec{i} \, d\partial \Omega \\
-(\nabla \cdot \epsilon^{(n-1)}, p^{(0)}) + \langle \epsilon^{(n-1)}, \nabla \times \omega^{(n-2)} \rangle &= + \int_{\partial K \setminus \partial \Omega} \epsilon^{(n-1)} \lambda \, d\partial \Omega &= \langle \epsilon^{(n-1)}, f^{(n-1)} \rangle - \int_{\partial \Omega} \epsilon^{(n-1)} p^{(0)} \, d\partial \Omega \\
&= + \int_{\partial K \setminus \partial \Omega} \epsilon^\lambda \llbracket u \rrbracket \, d\partial \Omega &= 0 \\
&= - \int_{\partial K \setminus \partial \Omega} \epsilon^\gamma \llbracket \omega \rrbracket \, d\partial \Omega &= 0 \\
&= + \int_C \epsilon^\gamma \theta &= 0 \\
&= + \int_C \epsilon^\theta \llbracket \gamma \rrbracket &= 0
\end{aligned} \tag{4.25}$$

$\forall \epsilon^{(0)} \in L^2(\Omega)$ ,  $\forall \epsilon^{(n-2)} \in H(\text{curl}; \Omega_K)$ ,  $\forall \epsilon^{(n-1)} \in H(\text{div}; \Omega_K)$ ,  $\forall \epsilon^\lambda \in H^{\frac{1}{2}}(\partial \Omega_K)$  and  $\forall \epsilon^\gamma \in H^{-\frac{1}{2}}(\partial \Omega_K)$ .

The variational formulation above (4.25) can be translated into the following matrix formulation:

$$\begin{bmatrix}
(\mathbb{M}^{(n)})^{-1} & 0 & -\mathbb{E}^{(n,n-1)} & 0 & 0 & 0 \\
0 & \mathbb{M}^{(n-2)} & -(\mathbb{M}^{(n-1)} \mathbb{E}^{(n-1,n-1)})^T & 0 & -(\mathbb{E}^{\gamma,n-2})^T & 0 \\
-(\mathbb{E}^{(n,n-1)})^T & -\mathbb{M}^{(n-1)} \mathbb{E}^{(n-1,n-2)} & 0 & (\mathbb{E}^{\lambda,n-1})^T & 0 & 0 \\
0 & 0 & \mathbb{E}^{\lambda,n-1} & 0 & 0 & 0 \\
0 & -\mathbb{E}^{\gamma,n-2} & 0 & 0 & 0 & (\mathbb{E}^{\theta,\gamma})^T \\
0 & 0 & 0 & 0 & \mathbb{E}^{\theta,\gamma} & 0
\end{bmatrix}
\begin{pmatrix}
[p]^{(0)} \\
[\omega]^{(n-2)} \\
[u]^{(n-1)} \\
[\lambda] \\
[\gamma] \\
[\theta]
\end{pmatrix}
=
\begin{pmatrix}
0 \\
[\gamma_B] \\
\mathbb{M}^{(n-1)} [f]^{(n-1)} - [\lambda_B] \\
0 \\
0 \\
0
\end{pmatrix} \tag{4.26}$$



Figure 4.8 compares the sparsity structure of the matrices in (4.26) (left) and in (4.27) (right). Both matrices have 3388 non-zero entries underlying the fact that the difference, among the two, lies only in the global numbering. Two main advantages arise using the block diagonal configuration: on one hand only the three matrices connected to the *Lagrange multipliers* needs to be assembled to the global configuration (in the previous case all seven matrices needed to be assembled), on the other hand  $\mathbb{A}$ , being an element block diagonal matrix, can be inverted very efficiently.

At this point, it is worth to recall what has been already done. In Chapter 3 the continuous formulation was derived while in this chapter the hybridized system was formulated. This was achieved adding the *Lagrange multipliers* which increase the number of degrees of freedom of the problem and so the size of the matrix in (4.27) with respect to (3.18). Therefore, even though the definition of the non-singular system is a result per se, the numerical advantage of the hybrid formulation has not been shown. This will be elaborated in the following section.

#### 4.6. The *Lagrange multipliers*' system

In Sections 4.1.1 and 4.1.2 it was explained the fact that the *Lagrange multipliers*  $\lambda$  and  $\gamma$  can be seen as boundary conditions for each element. Once the value of the *Lagrange multipliers* is known, the solution within each element can be computed locally, independent of each other. Using this solution path, we aim to reduce the computational time required for the solution of the physical variables  $-p, \omega, u-$  in the whole domain.

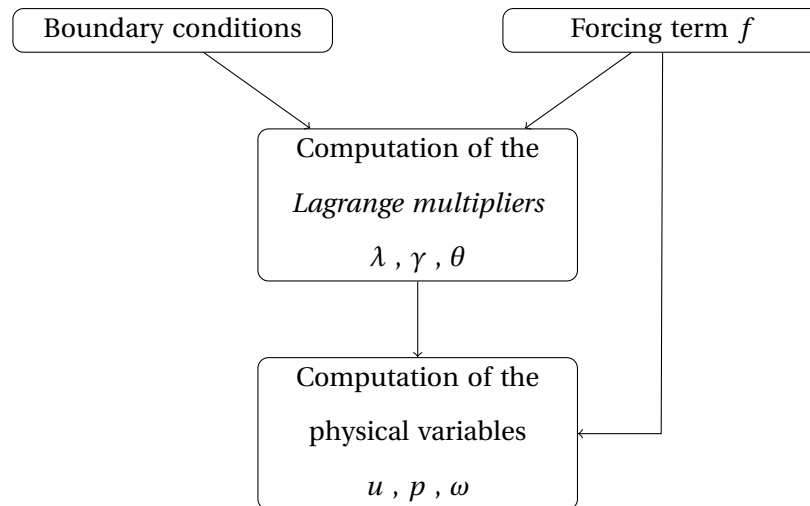


Figure 4.9: Solution flowchart

The solution flowchart may be seen in Figure 4.9. The first step is the computation of the *Lagrange multipliers* on the elements boundaries. For this purpose a dedicated system of equation has

to be written and will be called *reduced system* due to the fewer number of unknowns in comparison to the *full system* in (4.26) and in (4.27).

The reduced system is the following:

$$\begin{bmatrix} \nabla_{\lambda\lambda}^2 & \nabla_{\lambda\gamma}^2 & 0 \\ \nabla_{\gamma\lambda}^2 & \nabla_{\gamma\gamma}^2 & (\mathbb{E}^{\gamma\theta})^T \\ 0 & \mathbb{E}^{\gamma\theta} & 0 \end{bmatrix} \begin{pmatrix} [\lambda] \\ [\gamma] \\ [\theta] \end{pmatrix} = \begin{pmatrix} F^\lambda \\ F^\gamma \\ 0 \end{pmatrix}, \quad (4.29)$$

where the four matrices  $\nabla_{\cdot\cdot}^2$  and the two vectors  $F^\cdot$  can be computed using the algebraic elimination method:

$$\nabla_{\lambda\lambda}^2 = \mathbb{E}^{1\lambda} [(\mathbb{E}^{21})^T \mathbb{M}^2 \mathbb{E}^{21} + \mathbb{M}^1 \mathbb{E}^{10} (\mathbb{M}^0)^{-1} (\mathbb{M}^1 \mathbb{E}^{10})^T]^{-1} (\mathbb{E}^{1\lambda})^T, \quad (4.30)$$

$$\nabla_{\lambda\gamma}^2 = \mathbb{E}^{1\lambda} [(\mathbb{E}^{21})^T \mathbb{M}^2 \mathbb{E}^{21} + \mathbb{M}^1 \mathbb{E}^{10} (\mathbb{M}^0)^{-1} (\mathbb{M}^1 \mathbb{E}^{10})^T]^{-1} \mathbb{M}^1 \mathbb{E}^{10} (\mathbb{M}^0)^{-1} \mathbb{E}^{0\gamma}, \quad (4.31)$$

$$\nabla_{\gamma\lambda}^2 = (\nabla_{\lambda\gamma}^2)^T, \quad (4.32)$$

$$\begin{aligned} \nabla_{\gamma\gamma}^2 = & -\mathbb{E}^{0\gamma} (\mathbb{M}^0)^{-1} (\mathbb{E}^{0\gamma})^T - (\mathbb{M}^1 \mathbb{E}^{10} (\mathbb{M}^0)^{-1} \mathbb{E}^{0\gamma})^T [(\mathbb{E}^{21})^T \mathbb{M}^2 \mathbb{E}^{21} \\ & + \mathbb{M}^1 \mathbb{E}^{10} (\mathbb{M}^0)^{-1} (\mathbb{M}^1 \mathbb{E}^{10})^T]^{-1} (\mathbb{M}^1 \mathbb{E}^{10} (\mathbb{M}^0)^{-1} \mathbb{E}^{0\gamma}), \end{aligned} \quad (4.33)$$

$$F^\lambda = \mathbb{E}^{1\lambda} [(\mathbb{E}^{21})^T \mathbb{M}^2 \mathbb{E}^{21} + \mathbb{M}^1 \mathbb{E}^{10} (\mathbb{M}^0)^{-1} (\mathbb{M}^1 \mathbb{E}^{10})^T]^{-1} \mathbb{M}^1 f^{(1)}, \quad (4.34)$$

$$F^\gamma = -(\mathbb{M}^1 \mathbb{E}^{10} (\mathbb{M}^0)^{-1} \mathbb{E}^{0\gamma})^T [(\mathbb{E}^{21})^T \mathbb{M}^2 \mathbb{E}^{21} + \mathbb{M}^1 \mathbb{E}^{10} (\mathbb{M}^0)^{-1} (\mathbb{M}^1 \mathbb{E}^{10})^T]^{-1} \mathbb{M}^1 f^{(1)}. \quad (4.35)$$

After having solved the *reduced system* (4.29) in the whole domain, the *Lagrange multipliers*  $\lambda$  and  $\gamma$  are used as boundary conditions for the computation of the physical variables  $-p$ ,  $u$ ,  $\omega$ - in each element ( $\Omega_i$ ) using (4.36):

$$\begin{bmatrix} (\mathbb{M}_{\Omega_i}^{(n)})^{-1} & 0 & -\mathbb{E}_{\Omega_i}^{(n,n-1)} \\ 0 & \mathbb{M}^0 & -(\mathbb{M}_{\Omega_i}^{(n-1)} \mathbb{E}_{\Omega_i}^{(n-1,n-2)})^T \\ -(\mathbb{E}_{\Omega_i}^{(n,n-1)})^T & -\mathbb{M}_{\Omega_i}^{(n-1)} \mathbb{E}_{\Omega_i}^{(n-1,n-2)} & 0 \end{bmatrix} \begin{pmatrix} [p_{\Omega_i}]^{(0)} \\ [\omega_{\Omega_i}]^{(n-2)} \\ [u_{\Omega_i}]^{(n-1)} \end{pmatrix} = \begin{pmatrix} 0 \\ (\mathbb{E}^{\gamma,n-2})^T \gamma_{\Omega_i} \\ \mathbb{M}^{(n-1)} [f_{\Omega_i}]^{(n-1)} - (\mathbb{E}^{\lambda,n-1})^T \lambda_{\Omega_i} \end{pmatrix}. \quad (4.36)$$

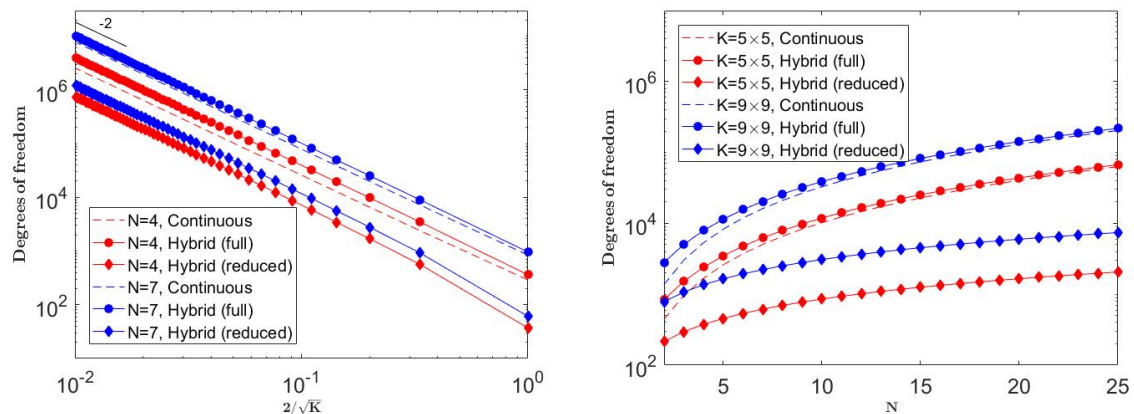


Figure 4.10: Number of degrees of freedom of the continuous, the full hybrid and the reduced formulation varying the number of elements (left) and the polynomial degree (right).

Figure 4.10 shows the number of unknowns for the continuous, the hybrid and the reduced formulation as a function of the number of elements (left) and the polynomial degree (right). It can be seen that the number unknowns for the hybrid and the full hybrid formulations converges, while the ones in the reduced system is considerably lower for any number of elements and polynomial degree.

As the original matrix (4.27), even the reduced system (4.29) maintains the positiveness and symmetric properties of the *Vector Laplacian* operator. This suggest (4.29) may be the matrix formulation of the *Laplacian operator* for another set of basis and test functions.

The following section is therefore dedicated to find this new, unknown set.

## 4.7. A new set of basis functions

It is easy to show that the number of the degrees of freedom of  $u^{(n-1)}$ ,  $p^{(0)}$  and  $\omega^{(n-2)}$  is generally higher than the number of the *Lagrange multipliers* ( $\lambda$ ,  $\gamma$ ,  $\theta$ ). Due to the fact that the solution is only in function of the latter, it is easy to conclude that the solution lies in a space smaller than the initial one:

$$(p, \omega, u) \in H(\text{div}; \Omega_K) \times L^2(\Omega) \times H(\text{curl}; \Omega_K) \quad . \quad (4.37)$$

B. Cockburn et. al. [11] computed the new set of basis functions for the scalar Poisson equation by solving the discontinuous system for the original variables when each *Lagrange multiplier* was equal to one. The solution was one set of functions of the unknown function space. In this thesis, dealing with the *vector Laplace* equation, two sets of basis functions (one for  $\lambda$  and the second for  $\gamma$ ), which will be respectively called  $p_{\lambda_i}$ ,  $\omega_{\lambda_i}$ ,  $u_{\lambda_i}$  and  $p_{\gamma_i}$ ,  $\omega_{\gamma_i}$ ,  $u_{\gamma_i}$ . They have been computed using the following systems of equation (the difference between the two lies in the RHS):

$$\begin{bmatrix} (\mathbb{M}^{(n)})^{-1} & 0 & -\mathbb{E}^{(n,n-1)} \\ 0 & \mathbb{M}^0 & -(\mathbb{M}^{(n-1)}\mathbb{E}^{(n-1,n-2)})^T \\ -(\mathbb{E}^{(n,n-1)})^T & -\mathbb{M}^{(n-1)}\mathbb{E}^{(n-1,n-2)} & 0 \end{bmatrix} \begin{pmatrix} [p_{\lambda_i}]^{(0)} \\ [\omega_{\lambda_i}]^{(n-2)} \\ [u_{\lambda_i}]^{(n-1)} \end{pmatrix} = \begin{pmatrix} 0 \\ 0 \\ -(\mathbb{E}^{\lambda n-1})^T \lambda_i \end{pmatrix}, \quad (4.38)$$

$$\begin{bmatrix} (\mathbb{M}^{(n)})^{-1} & 0 & -\mathbb{E}^{(n,n-1)} \\ 0 & \mathbb{M}^0 & -(\mathbb{M}^{(n-1)}\mathbb{E}^{(n-1,n-2)})^T \\ -(\mathbb{E}^{(n,n-1)})^T & -\mathbb{M}^{(n-1)}\mathbb{E}^{(n-1,n-2)} & 0 \end{bmatrix} \begin{pmatrix} [p_{\gamma_i}]^{(0)} \\ [\omega_{\gamma_i}]^{(n-2)} \\ [u_{\gamma_i}]^{(n-1)} \end{pmatrix} = \begin{pmatrix} 0 \\ (\mathbb{E}^{\gamma^{n-2}})^T \gamma_i \\ 0 \end{pmatrix}. \quad (4.39)$$

where  $\lambda_i$  (and  $\gamma_i$ ) refers to the boundary conditions in which one  $\lambda$  (or one  $\gamma$ ) on the boundary ( $p_i$  in Figure 4.3,  $u \cdot t_i$  in Figure 4.5) is equal to one and the others equal to zero.

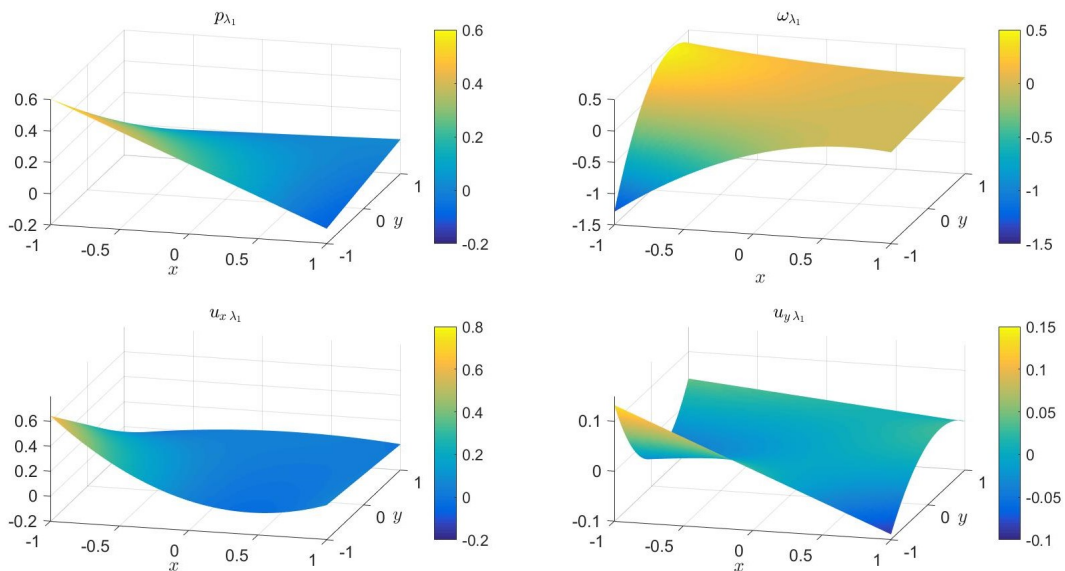


Figure 4.11:  $p_{\lambda_1}$  (top-left),  $\omega_{\lambda_1}$  (top-right),  $u_{\lambda_1}$  (bottom). Solution of (4.38) for  $\lambda_1 = 1$ . Single element of  $2^{nd}$ -order degree.

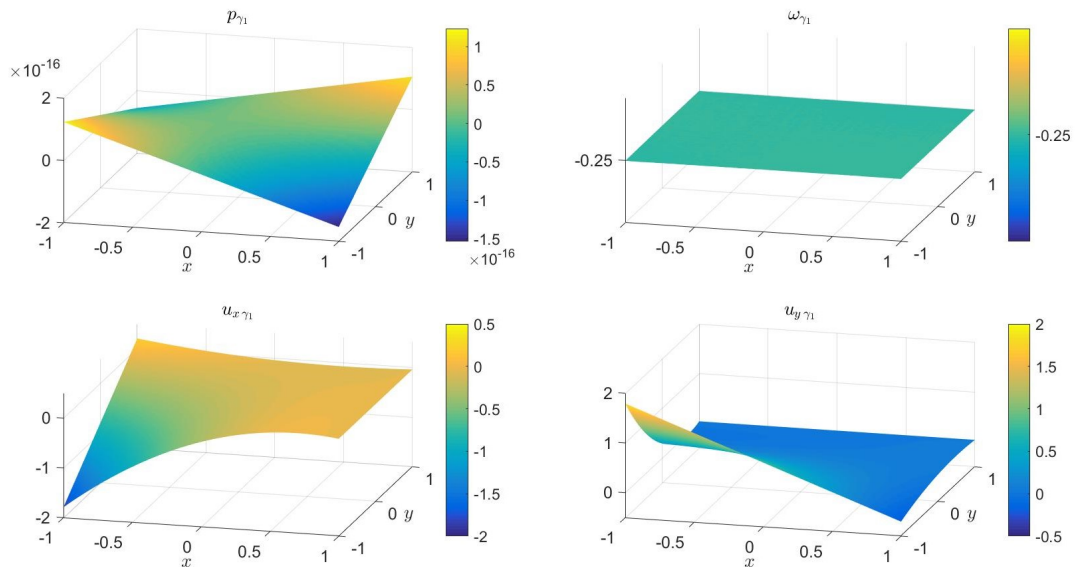


Figure 4.12:  $p_{\gamma_1}$  (top-left),  $\omega_{\gamma_1}$  (top-right),  $u_{\gamma_1}$  (bottom). Solution of (4.39) for  $\lambda_1 = 1$ . Single element of  $2^{nd}$ -order degree.

Figure 4.11 shows the solution on a single  $2^{nd}$ -degree element of (4.38) supposing  $p_1 = 1$  ( $p$  numbering in Figure 4.3). Immediately, it can be seen that even though  $p$  is equal to 1 in one part of the boundary, the maximum value of  $p_{\lambda_1}$  is 0.6. This suggests the weak imposition of the *Dirichlet* boundary condition, which will be further analysed in Chapter 6. Furthermore, considering the velocity flux ( $u_{x\lambda_1}$  for  $x = -1$  and  $x = 1$ ,  $u_{y\lambda_1}$  for  $y = -1$  and  $y = 1$ ) and the vorticity,  $\omega_{\lambda_1}$ , restricted to the boundary, this procedure is analogous to the (Neumann-Dirichlet) *Steklov-Poincaré operator* which maps Neumann interface variables ( $p = \nabla \cdot u \in \partial\Omega$ ) to Dirichlet interface variables ( $u \cdot n$  and  $\omega \in \partial\Omega$ ) [29]. Analogously, Figure 4.12 shows the solution of (4.39) considering  $\gamma_1 = 1$  ( $u \cdot t_1$  in Figure 4.5). In this case  $p_{\gamma_1}$  is equal to zero up to machine precision and  $\omega_{\gamma_1}$  is constant and equal to  $-0.25$  in the whole domain. Furthermore,  $u_{y\gamma_1}$  is positive in  $(x, y) = (-1, -1)$  which was expected imposing the tangential velocity equal to 1 on the leftward vertical boundary.

At this point, having the *basis functions*  $p_{\lambda_i}$ ,  $\omega_{\lambda_i}$ ,  $u_{\lambda_i}$  and  $p_{\gamma_i}$ ,  $\omega_{\gamma_i}$ ,  $u_{\gamma_i}$ , it is interesting to combine them in order to compute the *reduced system* (4.29) in an alternative way. Considering that the inner product between the velocity  $u^{(n-1)}$  and the *vector Laplace* of the velocity is equal to the following (using the integration by parts)

$$\begin{aligned} \langle u, \nabla^2 u \rangle_{\Omega} &= \langle u, \nabla(\nabla \cdot u) \rangle_{\Omega} - \langle u, \nabla \times \nabla \times u \rangle_{\Omega} \\ &= \langle \nabla \cdot u, \nabla \cdot u \rangle_{\Omega} + \langle u \cdot n, \nabla \cdot u \rangle_{\partial\Omega} - \langle \nabla \times u, \nabla \times u \rangle_{\Omega} + \langle u \cdot t, \nabla \times u \rangle_{\partial\Omega} \quad , \end{aligned} \quad (4.40)$$

the matrix  $\nabla_{\lambda\lambda}^2$  can be computed even in the following way:

$$\nabla_{\lambda\lambda}^2 = (u_{\lambda}^{(n-1)}, (E^{21})^T p_{\lambda}) + \langle u_{\lambda}, E^{10} \omega_{\lambda} \rangle \quad . \quad (4.41)$$

Looking at (4.41), someone may disagree with the first term being actually a duality pairing and not an

inner-product. In fact, looking more carefully at it, it can be noticed that  $u^{(n-1)}$  and  $(E^{21})^T p_\lambda^{(0)}$  belong to the primal and the dual grid, respectively. In Chapter 2, it was proved that a variable  $\psi^{(1)}$  and its dual,  $\psi^{(n-1)}$ , are mutually connected by the following formula [15]:

$$\psi^{(n-1)} = (\mathbb{M}^{(n-1)})^I \psi^{(1)} \quad . \quad (4.42)$$

Therefore, the inner product between  $u_\lambda^{(n-1)}$  and  $(\mathbb{M}^{(n-1)})^I (E^{21})^T p_\lambda$  can be computed in the following way:

$$\begin{aligned} \langle u_\lambda^{(n-1)}, (\mathbb{M}^{(n-1)})^I (E^{21})^T p_\lambda \rangle &= u_\lambda^{(n-1)} \mathbb{M}^{(n-1)} (\mathbb{M}^{(n-1)})^I (E^{21})^T p_\lambda \\ &= u_\lambda^{(n-1)} (E^{21})^T p_\lambda \\ &= (u_\lambda^{(n-1)}, (E^{21})^T p_\lambda) \quad , \end{aligned} \quad (4.43)$$

which completes the proof that (4.41) is equal to  $\langle u_\lambda^{(n-1)}, \nabla^2 u_\lambda^{(n-1)} \rangle$ .

Using the same reasoning, the following identities were found:

$$\nabla_{\gamma\lambda}^2 = \langle u_\gamma, \text{curl } \omega_\lambda \rangle \quad , \quad (4.44)$$

$$\nabla_{\gamma\gamma}^2 = \langle \omega_\gamma, \omega_\gamma \rangle \quad , \quad (4.45)$$

proving that the reduced system is actually the *Vector Laplace operator* on a different test and basis function, called  $p_\lambda, \omega_\lambda, u_\lambda$  and  $p_\gamma, \omega_\gamma, u_\gamma$ .

Even simpler are the explicit formulas for the computation of the known terms  $F^\lambda$  and  $F^\gamma$ . As in the full system formulation, the RHS is the inner product  $\langle e^{(1)}, f^{(1)} \rangle$ . It follows that the formulas for the *Lagrange multiplier's* system will be the following:

$$F^\lambda = \langle u_\lambda^{(n-1)}, f^{(n-1)} \rangle \quad , \quad (4.46)$$

$$F^\gamma = \langle u_\gamma^{(n-1)}, f^{(n-1)} \rangle \quad . \quad (4.47)$$



# 5

## Model Verification

The verification procedure of a newly-developed numerical method is defined as the *process of determining that a model implementation accurately represents the developer's conceptual description of the model and the solution to the model* [22].

For simple domains  $\Omega$ , such as a square in 2D, the *manufactured solution* is the easiest and fastest method to be used for verifying that the numerical scheme, developed in the previous chapters, actually solves the *Laplace equation*.

The domain used for the verification is the following:

$$\Omega = \{ \forall (x, y) \in \mathbb{R}^2 \mid -1 \leq x \leq 1 \ \& \ -1 \leq y \leq 1 \} \quad . \quad (5.1)$$

### 5.1. Divergence-free manufactured solution

In order to verify the scheme and to test the exactness of the imposition of the incompressibility constraint, a divergence-free solution was chosen with  $p = 0$  &  $\vec{u} \cdot \vec{\tau} = 0$  along  $\partial\Omega$ <sup>1</sup>. In light of the above, the following manufactured solution has been used as model verification test:

$$u = \begin{pmatrix} \cos(\pi x) \sin(\pi y) \\ -\sin(\pi x) \cos(\pi y) \end{pmatrix} \quad . \quad (5.2)$$

The curl of the vector field  $u$ ,  $\omega$ , is the following:

$$\omega = -2\pi \cos(\pi x) \cos(\pi y) \quad . \quad (5.3)$$

---

<sup>1</sup> $p = 0$  &  $\vec{u} \cdot \vec{\tau} = 0$  are the *natural* boundary conditions.

Furthermore, the *source term* can be computed from the manufactured solution, which is necessary to construct the RHS of the numerical method. Therefore  $f$  is equal to the following:

$$f = \begin{pmatrix} -2\pi^2 \cos(\pi x) \sin(\pi y) \\ 2\pi^2 \sin(\pi x) \cos(\pi y) \end{pmatrix}. \quad (5.4)$$

## 5.2. Qualitative analysis

Substituting  $f$  in the RHS of the numerical scheme, (4.27) can be solved. In order to qualitatively analyse the solution, a  $5 \times 5$  square grid of  $2^{nd}$  order discontinuous elements was chosen.

Following the solution procedure, at first the reconstruction of the *Lagrange multipliers* will be shown in Figures 5.1 and 5.2. For clarity, Figures 5.1 and 5.2 show the reconstruction of  $\lambda$  and  $\gamma$  only along the horizontal and vertical internal elements boundaries (i.e.  $\partial K \setminus \partial\Omega$ ) in which the value of  $\gamma$  is not zero.

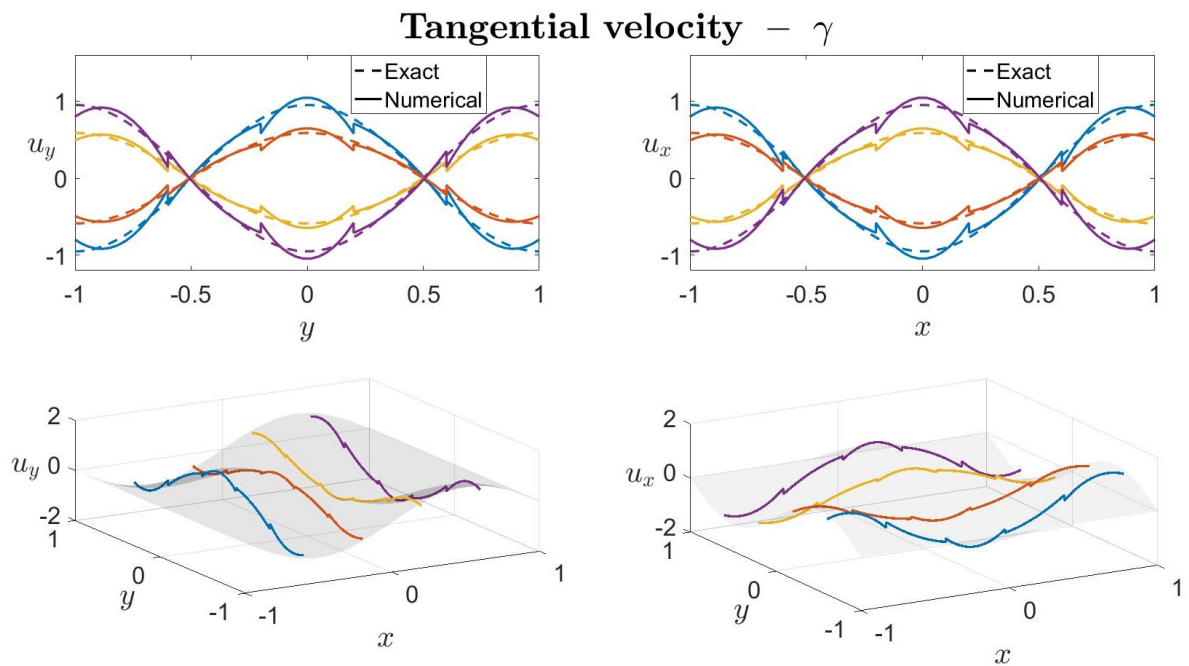


Figure 5.1: Comparison of the reconstruction of the *Lagrange multiplier*  $\gamma$  along internal element boundaries (coloured full lines) with the tangential part of the solution (dashed lines, grey shadow). The reconstruction on vertical lines is compared to  $u_y$  (left) while the one on horizontal lines to  $u_x$  (right).  $5 \times 5$  grid,  $2^{nd}$  order elements.

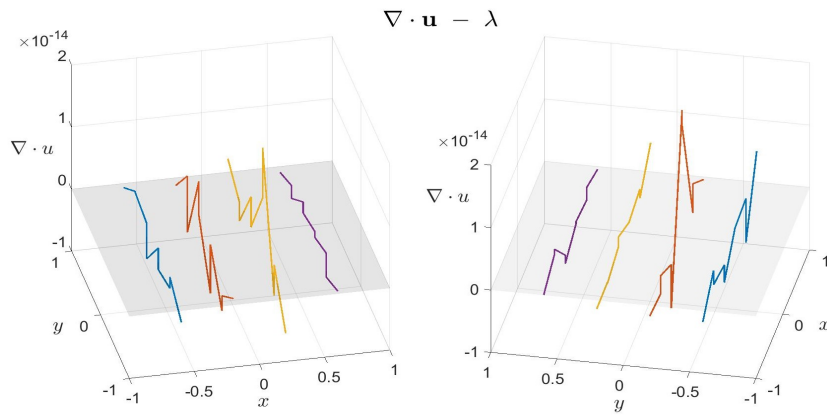


Figure 5.2: Comparison of the reconstruction of the Lagrange multiplier  $\lambda$  along internal element boundaries (coloured full lines) with the divergence of the solution (dashed lines, grey shadow).  $5 \times 5$  grid,  $2^{nd}$  order elements.

Figure 5.1 (bottom) visually compares the coloured reconstruction of  $\gamma$  with the tangential velocity between the elements of the manufactured solution (5.2) depicted as a grey shadow. The latter is equal to  $u_y$  for the vertical boundaries (left) and to  $u_x$  for the horizontal ones (right). Figure 5.1 (top) shows the comparison between the numerical solution (solid lines) and the exact one (dashed lines). It can be seen that  $\gamma$ , which represents the tangential velocity, is not continuous between the elements. Analogously, Figure 5.2 shows the agreements between the reconstruction of  $\lambda$  and the divergence of the solution. As can be seen, the reconstruction of  $\lambda$  is always lower than  $10^{-14}$  which already suggests the exactness of the incompressibility constraint ( $\nabla \cdot u = 0$ ).

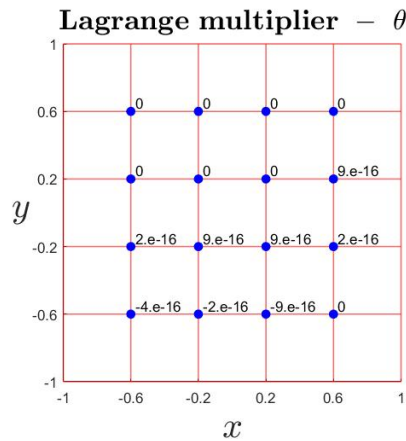


Figure 5.3: Reconstruction of the *Lagrange multiplier*  $\theta$  on the point intersection of more than two elements.  $5 \times 5$  grid,  $2^{nd}$  order elements.

Figure 5.3 shows the value of the *Lagrange multiplier*  $\theta$  on the point intersections. At first look, it is clearly visible the fact that  $\theta$  is equal to zero up to machine precision in every point of the domain in which it

is defined. Starting from (4.24) and imposing  $\theta = 0$  yields:

$$\begin{aligned}
 \omega_{nw} - \omega_{ne} &= 0 \quad , \\
 \omega_{ne} - \omega_{se} &= 0 \quad , \\
 \omega_{sw} - \omega_{se} &= 0 \quad , \\
 \omega_{nw} - \omega_{sw} &= 0 \quad .
 \end{aligned}
 \tag{5.5}$$

Equation (5.5) implies the correct imposition of the continuity of the vorticity in the corner points which is described by the following formula:

$$\omega_{nw} = \omega_{ne} = \omega_{se} = \omega_{sw} \quad .
 \tag{5.6}$$

Leaving behind the analysis of the *Lagrange multipliers* and moving to the one of the physical variables, Figures 5.4, 5.5 and 5.6 compare the exact and the numerical solution of the vorticity,  $\omega$ , horizontal,  $u_x$ , and vertical,  $u_y$ , velocity computed on an element-by-element fashion.

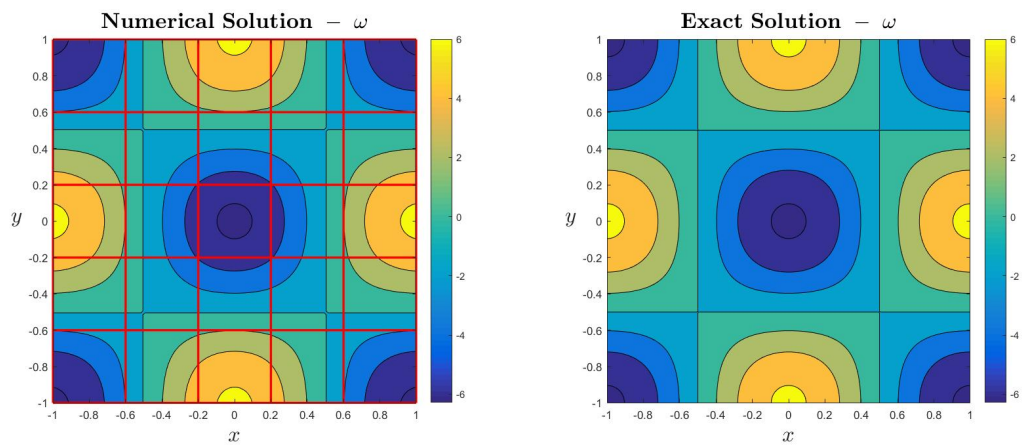


Figure 5.4: Comparison between the numerical (left) and the exact solution (right) of the vorticity ( $\omega$ ).  $5 \times 5$  grid,  $2^{nd}$  order elements.

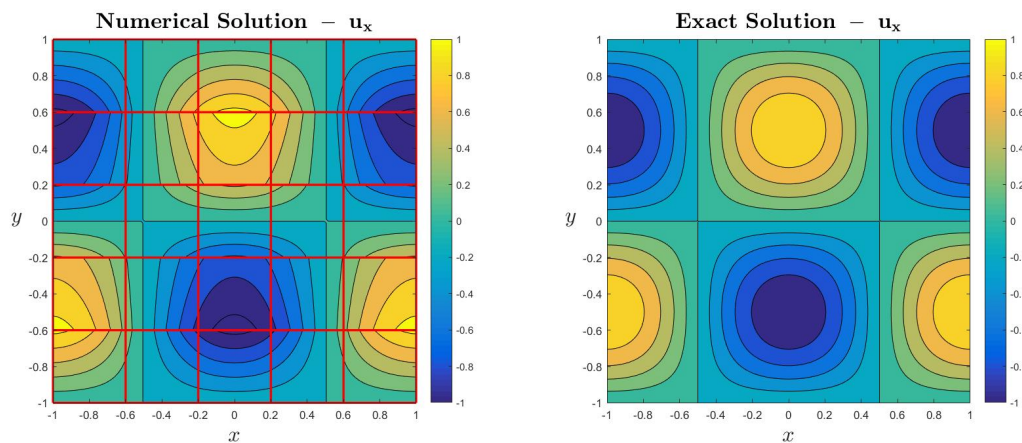


Figure 5.5: Comparison between the numerical (left) and the exact solution (right) of the horizontal velocity ( $u_x$ ).  $5 \times 5$  grid,  $2^{nd}$  order elements.

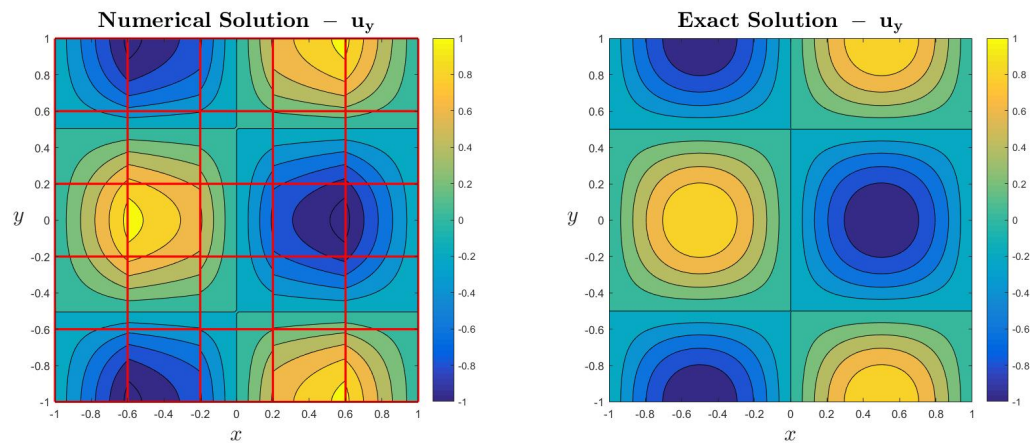


Figure 5.6: Comparison between the numerical (left) and the exact solution (right) of the vertical velocity ( $u_x$ ).  $5 \times 5$  grid,  $2^{nd}$  order elements.

As can be seen, although the mesh is coarse and the polynomial degree low, the numerical solutions (right) resemble the exact ones (left). However, while  $\omega$  is continuous in Figure 5.4,  $u_x$  shows discontinuities in the y-direction in Figure 5.5 while  $u_y$  in the x-direction in Figure 5.6. These discontinuities can be clearly seen by looking at the reconstruction of  $u_x$  and  $u_y$  in prospective view in Figure 5.7.

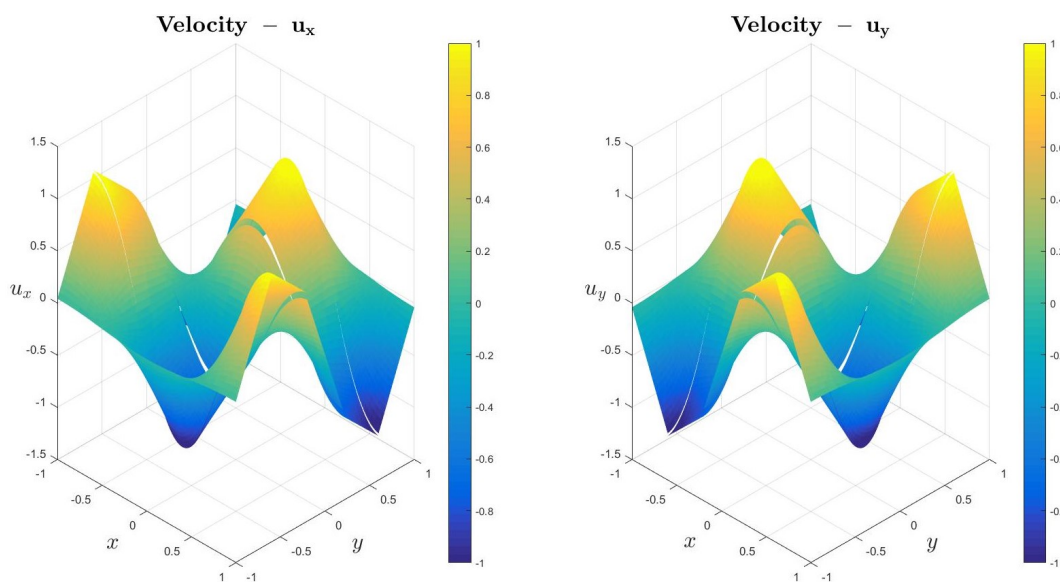


Figure 5.7: Reconstruction of the vertical velocity,  $u_x$ , (left) and the horizontal velocity,  $u_y$ , (right) in prospective view.  $5 \times 5$  grid,  $2^{nd}$  order elements.

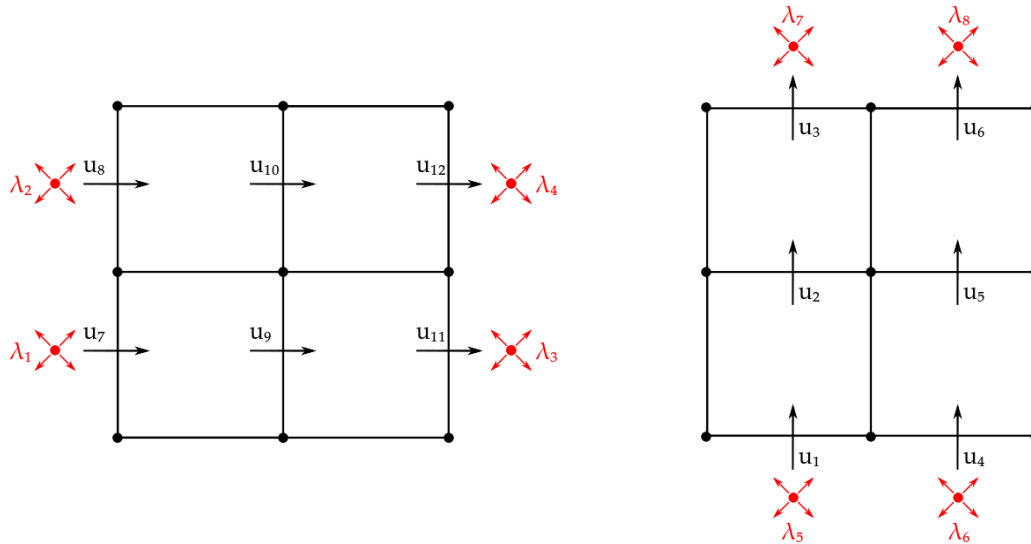


Figure 5.8: Position of the degrees of freedom of  $u_x$  (left) and  $u_y$  (right) and the *Lagrange multipliers*  $\lambda$  which respectively impose their continuity.

Figure 5.8 explicitly indicates the location of the degrees of freedom which describe the horizontal velocity,  $u_x$ , on the left and the vertical velocity,  $u_y$ , on the right. Furthermore,  $\lambda$  *Lagrange multipliers* are divided into the ones which impose the continuity on  $u_x$  and  $u_y$ , respectively<sup>2</sup>. As can be seen, the continuity of the horizontal component of the velocity is imposed by  $\lambda$  *Lagrange multipliers* on the right and left boundaries of the elements while  $\lambda$  on top and bottom boundaries impose the continuity on  $u_y$ . These are the reasons why  $u_x$  is continuous in the x-direction and discontinuous along y. The opposite reasoning may be used to explain the discontinuities in the reconstruction of  $u_y$ . Increasing the degrees of freedom (increasing the number of elements or the polynomial degree) these discontinuities reduce.

The fact that the  $\gamma$  *Lagrange multiplier* converges to the expected quantity gives a positive indication of the successful implementation of the *Lagrange multipliers* and suggests that they have a physical meaning. Furthermore, the fact that  $\lambda$  is close to the machine precision suggests that the method is able to compute exactly divergence-free solutions. This can be seen even in Figure 5.9 where the numerical solution of  $p$  is shown. It has to be noted that  $p$  is equal to zero, up to machine precision, in the whole domain.

<sup>2</sup>It is worth to point out that this is only an alternative way to see Figure 4.3 which can be considered as the summation between Figures 5.8 (left) and (right).

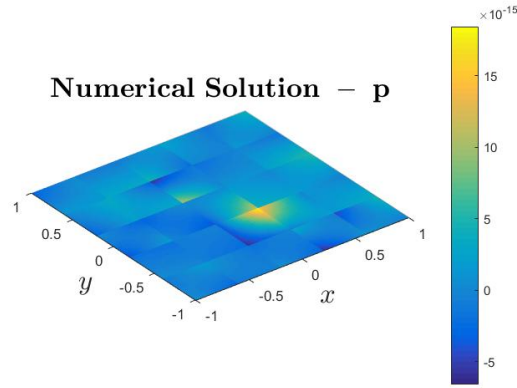


Figure 5.9: Reconstruction of the variable  $p$ , which is equal to  $\nabla \cdot u$ , on the domain  $\Omega$ .  $5 \times 5$  grid,  $2^{nd}$  order elements.

In order to unequivocally prove the quality of the numerical method, the convergence rate will be studied.

### 5.3. h-Convergence rate analysis

When engineers and mathematicians study the quality of a new numerical method, they do not only focus on the error as an absolute value, but they even analyse how fast (i.e. at which rate) the error converges to zero increasing the number of elements. In contrast to before, initially the attention will be given to the relevant physical variables  $p$ ,  $\omega$  and  $u$  and only afterwards to the *Lagrange multipliers*  $\lambda$  and  $\gamma$ .

The  $L^2$ -error, naturally derived from the  $L^2(\Omega)$  norm, will be computed and the convergence rate calculated. Calling  $\phi$  the variable for which the error has to be computed, the following formula will be used:

$$\|\phi^e - \phi^h\|_{L^2(\Omega)} = \sqrt{\int_{\Omega} (\phi^e - \phi^h)^2} \quad , \quad (5.7)$$

where  $\phi^e$  indicates the exact solution and  $\phi^h$  the reconstruction of the numerical solution.

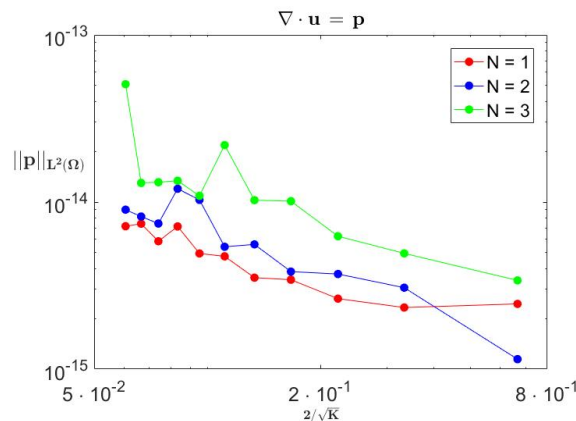


Figure 5.10: h-Convergence plot of  $L^2(\Omega)$ -error of the divergence of  $u$ ,  $p$ .  $K = \{3^2, 6^2, \dots, 33^2\}$ .

Figure 5.10 shows the convergence analysis of the variable  $p = \nabla \cdot u$ . It can be seen that the divergence

of  $u$  is exact up to machine precision even with very coarse meshes ( $K = 2^2$ ) and low polynomial degree ( $N = \{1, 2, 3\}$ ). Increasing  $K$ , the error increases up to  $O(10^{-14})$ . This is caused partially by the the increase of the *condition number*, and partially by the fact that  $[p]^0$  is equal to  $10^{-15}$  but, decreasing the element size, the edge basis functions grows, increasing the error. This indicates that the divergence-free constraint can be imposed exactly using discontinuous elements equipped with *Lagrange multipliers* at the element boundary. Once this is established, it is worth to analyse if this constraint compromises the convergence of the other variables or not.

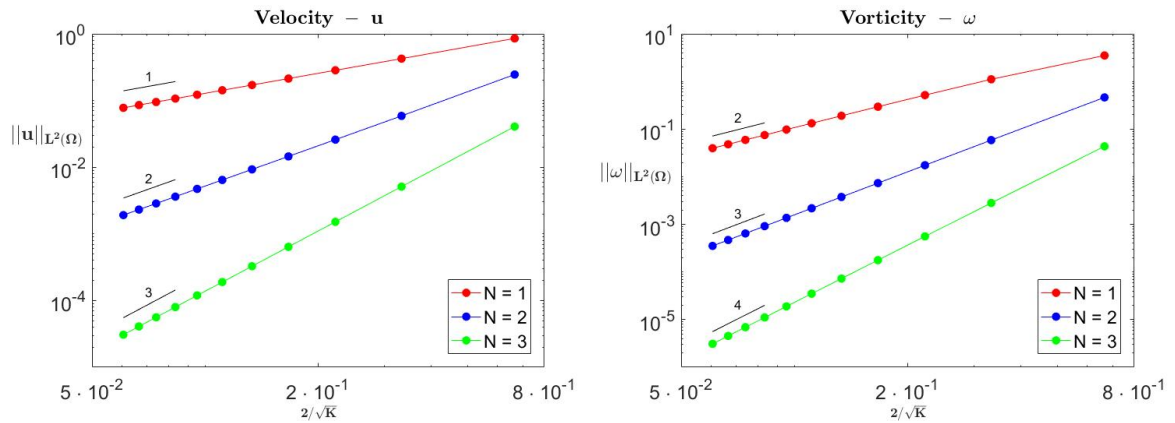


Figure 5.11:  $h$ -convergence of  $L^2(\Omega)$ -error of the velocity  $u$  (left) and the vorticity (right).  $K = \{3^2, 6^2, \dots, 33^2\}$ .

Figure 5.11 shows the  $h$ -convergence analysis of the  $L^2$ -error of  $\omega$  and  $u$  using elements of degrees 1, 2 and 3 as depicted in the legend. The black number above each line indicates the rate of convergence.

The *optimal convergence rate* is achieved when the error is proportional to  $h^{\mathcal{P}+1}$  for sufficiently smooth problems, where  $h$  is the element size ( $h = 2/\sqrt{K}$ ),  $K$  denotes the number of elements) and  $\mathcal{P}$  the minimum degree of the basis functions that describe the variable.

| $N$ | $\omega$ | $u_x$ | $u_y$ | $p$   |
|-----|----------|-------|-------|-------|
| 1   | (1,1)    | (1,0) | (0,1) | (0,0) |
| 2   | (2,2)    | (2,1) | (1,2) | (1,1) |
| 3   | (3,3)    | (3,2) | (2,3) | (2,2) |

Table 5.1: Polynomial degree in the horizontal ( $\cdot$ ,) and vertical ( $\cdot$ ,) direction of the basis functions associated to the variables  $\omega$ ,  $u$ , and  $p$  in relation to the element degree ( $N$ ).

Table 5.1 shows the degrees of the basis functions in which each variable is discretized. Comparing the table and the figure, it is possible to notice that both  $u$  and  $\omega$  converge optimally with decreasing element size. An interesting example is the velocity variable ( $u$ ), for which the basis functions have different polynomial degrees in  $x$  and  $y$ -directions: in this case, the convergence is determined by the lowest polynomial degree.

Focusing the attention on the *Lagrange multipliers*  $\lambda$  and  $\gamma$ , it is interesting to see how fast they converge to  $p$  and the tangential velocities respectively.

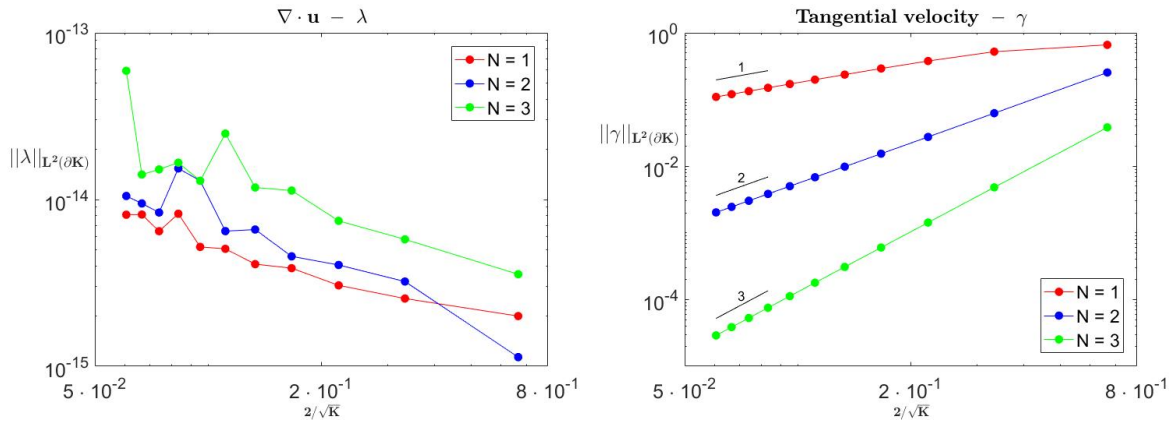


Figure 5.12: h-Convergence plot of  $L^2(\partial K)$ -error of  $\lambda$  (left) and  $\gamma$  (right).  $K = \{3^2, 6^2, \dots, 33^2\}$ .

Figure 5.12 (left) shows the convergence rate of  $\lambda$ . Recalling that it is equal to the divergence of  $u$  on the boundary it does not surprise that it is equal to zero up to machine precision for every domain discretization and polynomial degree. Figure 5.12 (right) shows the convergence of  $\gamma$  increasing the number of elements. Recalling that it is defined on the dual counterpart of the primal points (in which  $\omega$  is defined)  $\gamma$  does not converge optimally but with the same rate as  $u$ .

### 5.4. p-Convergence rate

Using the  $L^2$ -error previously defined, it is possible to compute the convergence of the three variables  $p$ ,  $\omega$  and  $u$  varying the degree ( $N$ ) of the elements used

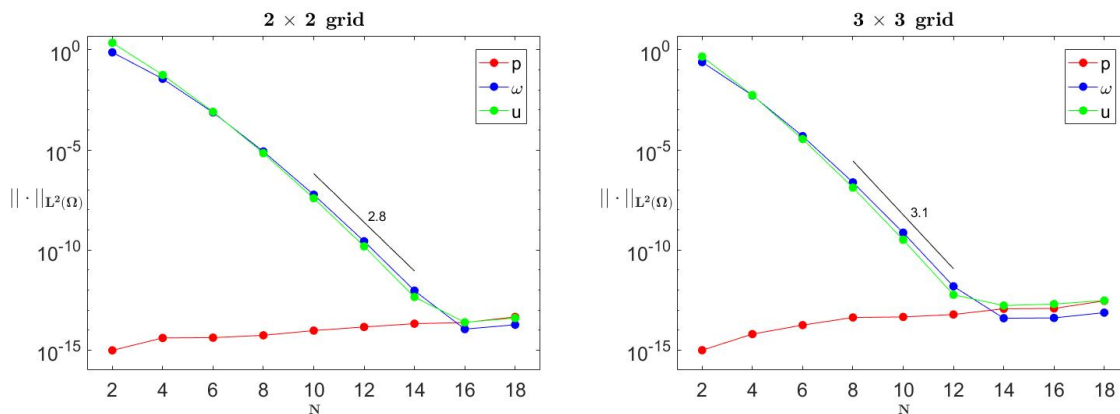


Figure 5.13:  $N$ -Convergence plot of  $L^2(\Omega)$ -error of  $p$ ,  $\omega$  and  $u$ .  $2 \times 2$  grid (left) and  $3 \times 3$  grid (right).

Figure 5.13 shows the convergence on a  $2 \times 2$  (left) and  $3 \times 3$  grid (right). The linear trend on a semi logarithmic plot proves the exponential convergence for the variables  $\omega$  and  $p$  which is equal to 2.8 and 3.1

for the  $2 \times 2$  (left) and  $3 \times 3$  grid, respectively. The exponential convergence rate,  $\alpha$ , is defined as follows:

$$y = C \cdot e^{-\alpha N} \quad . \quad (5.8)$$

It is to be noted that even in this case  $p$  is equal to zero up to machine precision and that the error only slightly increases with  $N$ . In both graphs the errors of  $\omega$  and  $u$  reach the numerical precision and then follow the same trend as  $p$ .

## 5.5. Computation time

In the introduction of Chapter 4 it was pointed out that the usage of discontinuous elements leads to a higher degree of parallelism of the computational method.

Therefore, it is interesting to understand if and how much computational time can be saved passing from the continuous formulation to the newly developed hybrid discontinuous method.

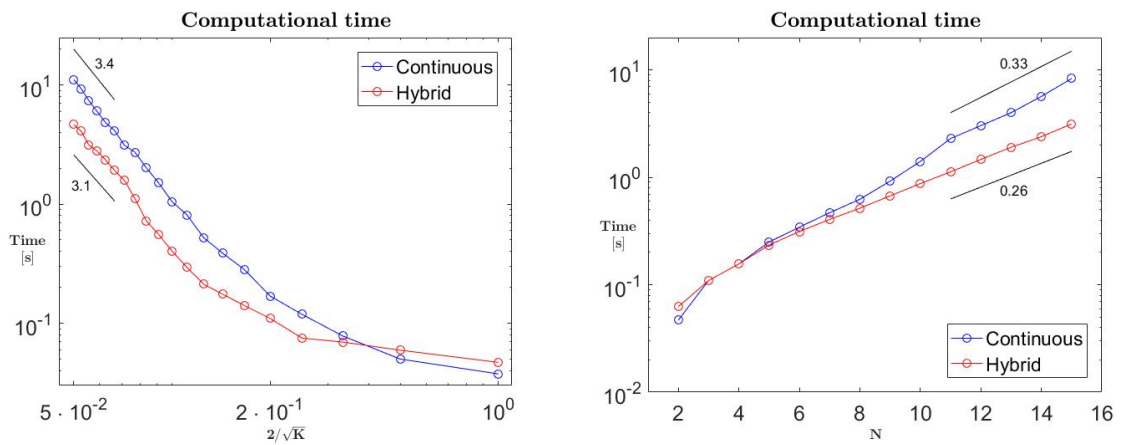


Figure 5.14: Computational time [s] for  $K = \{2^2, 4^2, \dots, 40^2\}$ ,  $N = 2$  (left) and for  $K = 3^2$ ,  $N = \{2, 3, \dots, 15\}$  (right).

Figure 5.14 (left) shows the computational time required for the computation of the physical time varying the number of elements for a  $2^{nd}$ -degree element. For the continuous case, it refers to the time needed for assembling the matrices and the solution of the full system, instead the time of the hybrid formulation refers to the summation of the time needed to assemble the matrices, the computation of the *reduced system* and the computation of the physical variables on one element. It can be noticed that, apart from a very coarse mesh, the time required by the hybrid formulation is lower than the one required by the continuous method. Furthermore, for finer meshes, a linear trend is identified in the logarithmic plot which is lower for the hybrid formulation. Similar conclusions can be made looking at the plot in Figure 5.14 (right) in which, for a 3 by 3 grid, the degree of the element is increased.

This confirms that the hybrid approach is interesting for the reduced computational time derived by its usage.

# 6

## Lid-driven cavity Stokes-flow

The lid-driven cavity Stokes flow is a unique test case for numerical methods applied to fluid dynamics. It combines the geometrical simplicity and the numerical complexity of flows with singularities.

This particular test case deals with a zero-Reynolds number flow in a square domain, in which the upper boundary moves with a unit velocity to the right. On the one hand, the geometrical simplicity is derived by the square fluid domain which is very easy to discretize. On the other hand, the numerical complexity derives from the fact that the solution becomes singular in the two upper vertices (both vorticity ( $\omega$ ) and pressure ( $p$ ) become infinity), due to the discontinuities of the velocity [19].

### 6.1. Incompressible Stokes equations: from the variational to the matrix formulation

Assuming the square domain  $\Omega$  described in (5.1), the lid-driven cavity Stokes flow is described by the following mixed formulation (3.6, with  $\mu = 1$ ) and boundary conditions:

$$\left\{ \begin{array}{l} \nabla \cdot \vec{u} = 0 \\ \omega \quad -\nabla \times \vec{u} = 0 \\ -\nabla p \quad -\nabla \times \omega = 0 \end{array} \right. \quad \text{and} \quad \left\{ \begin{array}{l} u \cdot \vec{n} = 0 \quad \text{on } \Gamma \\ u \cdot \vec{t} = 0 \quad \text{on } \Gamma_l \cup \Gamma_r \cup \Gamma_b \\ u \cdot \vec{t} = 1 \quad \text{on } \Gamma_t \end{array} \right. . \quad (6.1)$$

where  $\Gamma = \partial\Omega = \bigcup_{i=l,r,t,b} \Gamma_i$ <sup>1</sup>.

The same variable collocation described in Chapter 3 is used according to which the velocity ( $u$ ) is associated to the primal edges, the vorticity ( $\omega$ ) to the primal points and the pressure ( $p$ ), which represents the

---

<sup>1</sup> $l,r,t,b$  stand for left, right, top and bottom boundary.

pressure of the fluid, to the dual points. Due to the boundary conditions in (6.1), the *Lagrange multipliers* need to be positioned as per requirement of boundary conditions.

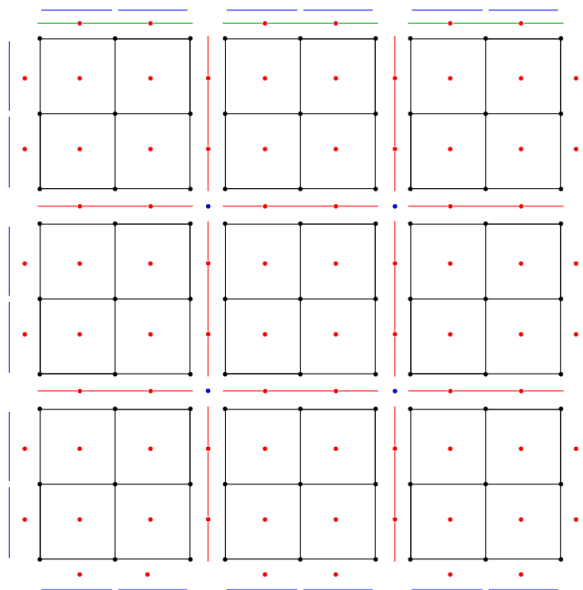


Figure 6.1: Lid-driven cavity Stokes flow: discretization of the physical domain.

$u$  and  $\omega$  are described by the primal black edges and points while the internal dual red points describe the position of  $p$ . The red points and lines in the element boundaries shows the *Lagrange multipliers*  $\lambda$  and  $\gamma$ , respectively. The blue points represents the location of  $\theta$ . On the boundary blue primal edges impose the impermeability condition while the green edges, on the top boundary, impose the unitary tangential velocity boundary condition.

Figure 6.1 shows the positioning of the *Lagrange multipliers* for a  $3 \times 3$  grid of  $2^{nd}$  order elements. It can be seen that in the physical boundary ( $\partial\Omega$ ) blue edge are added to strongly impose the non-permeability condition ( $u \cdot \vec{n} = 0$ ). Tangential boundary conditions are applied using  $\gamma$ . Green  $\gamma$  *Lagrange multipliers* are added to the top boundary to impose  $u \cdot \vec{t} = 1$  while on the other boundaries  $\Gamma_{l,r,b}$  zero tangential velocity has been imposed and are, therefore, left out of the figure.

Taking into account the variable-geometry coupling, (6.1) and the usage of *Lagrange multipliers* to impose the continuity among discontinuous elements and the boundary conditions on the physical domain, the variational formulation may be stated as follows: for a given  $f \in L^2(\Omega)$ , find  $u \in H(div; \Omega_K)$ ,  $p \in L^2(\Omega)$ ,  $\omega \in H(curl; \Omega_K)$ ,  $\lambda \in H^{\frac{1}{2}}(\partial\Omega_K)$  and  $\gamma \in H^{-\frac{1}{2}}(\partial\Omega_K)$ , such that:

$$\begin{aligned}
& (\epsilon^{(0)}, \nabla \cdot \mathbf{u}^{(n-1)}) & & = & 0 \\
\langle \epsilon^{(n-2)}, \omega^{(n-2)} \rangle & - \langle \nabla \times \epsilon^{(n-2)}, \mathbf{u}^{(n-1)} \rangle & - \int_{\partial K \setminus \partial \Omega} \epsilon^{(n-2)} \gamma \, d\partial \Omega & = & \int_{\partial \Omega} \epsilon^{(n-2)} \mathbf{u} \cdot \vec{\mathbf{i}} \, d\partial \Omega \\
(\nabla \cdot \epsilon^{(n-1)}, \mathbf{p}^{(0)}) & - \langle \epsilon^{(n-1)}, \nabla \times \omega^{(n-2)} \rangle & - \int_{\partial K \setminus \partial \Omega} \epsilon^{(n-1)} \lambda \, d\partial \Omega & = & \langle \epsilon^{(n-1)}, \mathbf{f}^{(n-1)} \rangle \\
& & - \int_{\partial K \setminus \partial \Omega} \epsilon^\lambda \llbracket \mathbf{u} \rrbracket \, d\partial \Omega & = & 0 \\
& & - \int_{\partial K \setminus \partial \Omega} \epsilon^\gamma \llbracket \omega \rrbracket \, d\partial \Omega & = & 0 \\
& & & & - \int_{\partial K \setminus \partial \Omega} \epsilon^\gamma \theta & = & 0 \\
& & & & - \int_{\partial K \setminus \partial \Omega} \epsilon^\theta \llbracket \gamma \rrbracket & = & 0
\end{aligned} \tag{6.2}$$

Using the definition of the inner product defined in Chapter 2 and the *Lagrange multipliers'* matrices in Chapter 4, the variational formulation (6.2) can be translated into the following matrix formulation:

$$\begin{bmatrix}
\mathbb{A} & -(\mathbb{E}^{\lambda, n-1})^T & -(\mathbb{E}^{\gamma, n-2})^T \\
-\mathbb{E}^{\lambda, n-1} & & \\
-\mathbb{E}^{\gamma, n-2} & & \\
& & & \mathbb{E}^{\theta, \gamma}
\end{bmatrix}
(\mathbb{E}^{\theta, \gamma})^T
\begin{pmatrix}
\mathbf{X} \\
[\lambda] \\
[\gamma] \\
[\theta]
\end{pmatrix}
=
\begin{pmatrix}
\mathbf{F} \\
\mathbb{E}_B^{\lambda, n-1} [\mathbf{u}_B^{(n-1)}] \\
0 \\
0
\end{pmatrix} \tag{6.3}$$

where  $\mathbb{A}$ ,  $\mathbf{X}$  and  $\mathbf{F}$  are equal to the following<sup>2</sup>:

<sup>2</sup> $\cdot_{\Omega_i}$  indicates the local matrix associated to the element  $\Omega_i$ .

$$\mathbf{A} = \begin{bmatrix} 0 & 0 & \mathbb{E}_{\Omega_1}^{(n,n-1)} \\ 0 & \mathbb{M}_{\Omega_1}^{(n-2)} & -\left(\mathbb{M}_{\Omega_1}^{(n-1)} \mathbb{E}_{\Omega_1}^{(n-1,n-1)}\right)^T \\ \left(\mathbb{E}_{\Omega_1}^{(n,n-1)}\right)^T & -\mathbb{M}_{\Omega_1}^{(n-1)} \mathbb{E}_{\Omega_1}^{(n-1,n-2)} & 0 \\ \vdots & \vdots & \vdots \\ 0 & 0 & \mathbb{E}_{\Omega_K}^{(n,n-1)} \\ 0 & \mathbb{M}_{\Omega_K}^{(n-2)} & -\left(\mathbb{M}_{\Omega_K}^{(n-1)} \mathbb{E}_{\Omega_K}^{(n-1,n-1)}\right)^T \\ \left(\mathbb{E}_{\Omega_K}^{(n,n-1)}\right)^T & -\mathbb{M}_{\Omega_K}^{(n-1)} \mathbb{E}_{\Omega_K}^{(n-1,n-2)} & 0 \end{bmatrix}, \quad (6.4)$$

$$\mathbf{X} = \prod_{i=1}^K \begin{pmatrix} [\tilde{p}^{(0)}] \\ [\omega^{(n-2)}] \\ [u^{(n-1)}] \end{pmatrix}_{\Omega_i} \quad \text{and} \quad \mathbf{F} = \prod_{i=1}^K \begin{pmatrix} 0 \\ (\mathbb{E}^{\gamma,n-2})^T [\gamma_B] \\ \mathbb{M}^{(n-1)} [f^{(n-1)}] \end{pmatrix}_{\Omega_i}.$$

The boundary conditions in (6.1) are represented in the matrix formulation:  $[u_B^{(n-1)}] = 0$  and  $\gamma_B = \mathbb{M}_1^{(n-2)} [u_x(x, 1)^{(n-2)}]$ .  $\mathbb{M}_1^{(n-2)}$  is the mass matrix associated to the primal points considering the boundary as a one-dimensional domain and  $[u_x(x, 1)^{(n-2)}]$  is the value of the tangential velocity on the upper boundary in the primal points.

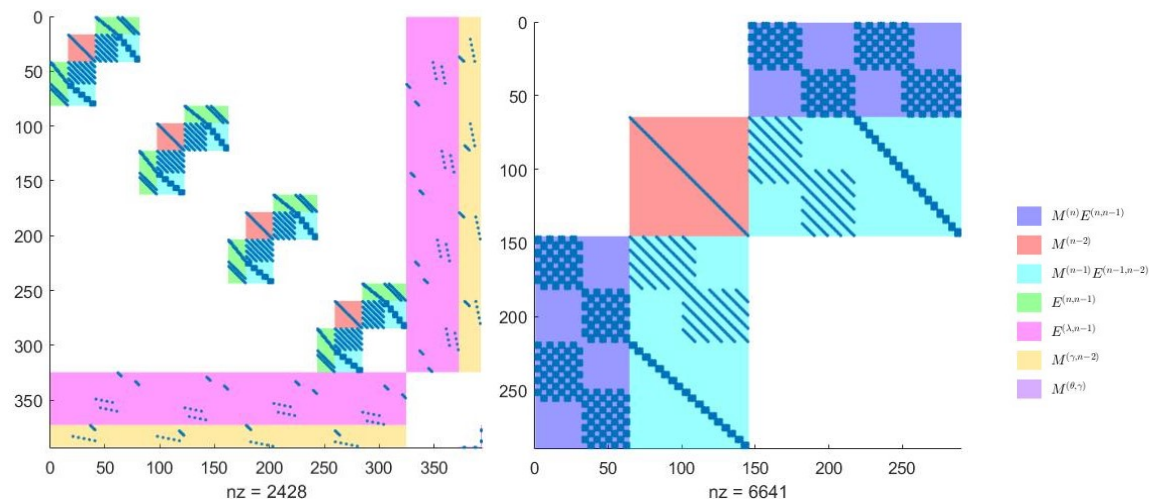


Figure 6.2: Sparsity structure of the LHS in (6.3) (left) and mixed method presented by J.Kreft et. al. in [19] (right).  $2 \times 2$  grid,  $4^{th}$  order elements.

In Figure 6.2 we show the sparsity structure of the matrix resulting from the primal-dual hybrid formulation<sup>3</sup> (left) with the continuous primal formulation developed by J.Kreft et. al. in [19] (right). For cleanness, plots in Figure 6.2 were originated by a  $2 \times 2$  grid of  $4^{th}$  order elements. It can be seen that even though the total number of unknowns in the hybrid formulation is higher, 393 degrees of freedom versus 289 for the continuous formulation, the number of non zero entries in the sparse matrix of the hybrid formulation is roughly one third (2428 versus 6641).

<sup>3</sup>Matrix in 6.3.

It has to be noted that due to the mimetic structure of the finite element method presented, no other changes, concerning the singularities on the upper corners, are needed, which is in contrast to the common nodal finite elements methods [8]. Another solution to overcome this problem is the transition to the *regularized driven cavity problem*, which has qualitatively the same dynamical properties as the lid-driven cavity flow [23].

## 6.2. Numerical solution

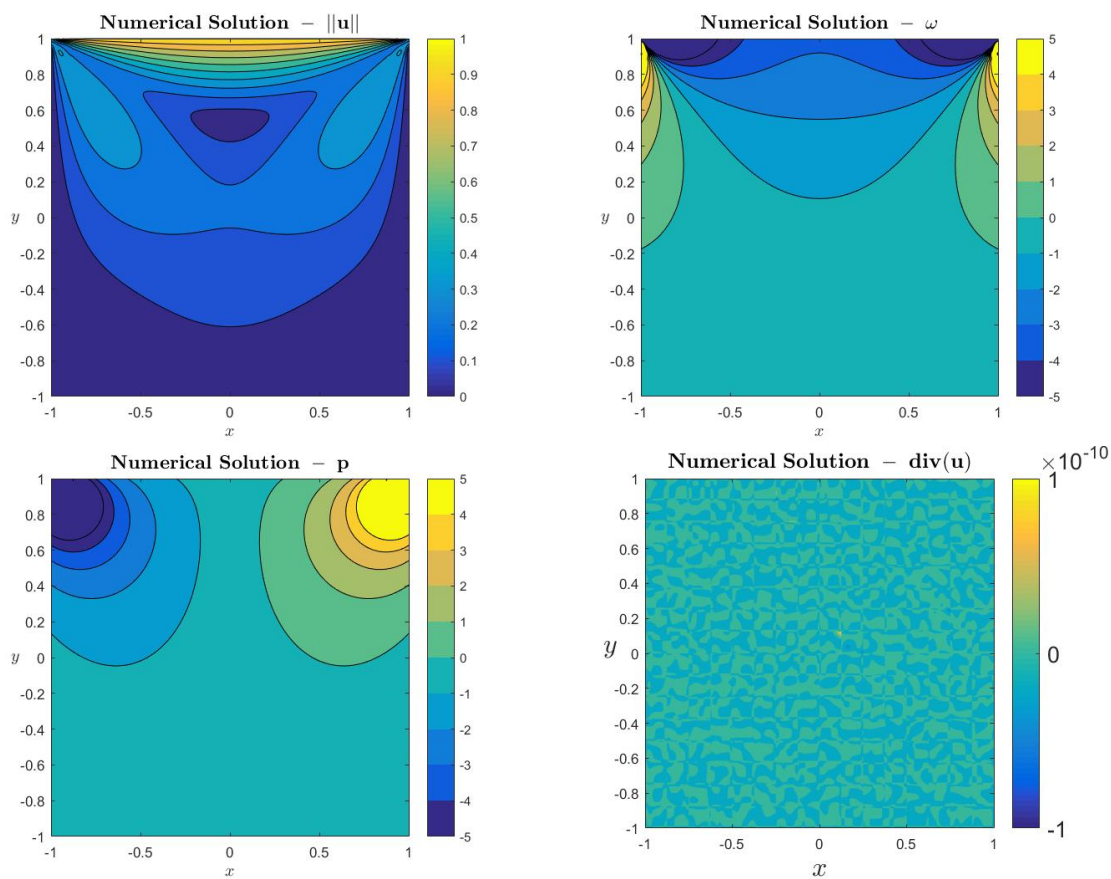


Figure 6.3: Numerical solution of the lid-driven Stokes flow: velocity magnitude (top-left), vorticity (top-right), pressure (bottom-left) and the divergence of the velocity (bottom-right).  $16 \times 16$  grid,  $4^{th}$  order elements.

Figure 6.3 shows the velocity magnitude, vorticity and pressure distribution of the lid-driven cavity Stokes flow computed using (6.3). At the bottom-left image the two singularities on the pressure field are clearly visible on the upper corners. The pressure converges to minus and plus infinity on the upper left and right corner, respectively. A  $16 \times 16$  grid and  $4^{th}$  order elements were used. It is worth to underline that this solution is in perfect agreement with the one in [23] for  $Re = 0$ , in which the effects of the singularities are visible in the pressure and vorticity distribution. The absence of discontinuities proves the successful application of the *Lagrange multipliers* for the imposition of the continuity among elements, while the overall agreement

indicates the correct implementation of the Dirichlet boundary conditions in  $\partial\Omega$ . To validate further the correctness of the implementation of the *Lagrange multipliers*, Figure 6.4 and Figure 6.5 show the reconstruction of  $\lambda$  and  $\gamma$ , respectively. Even in this case, both have a physical meaning:  $\lambda$  converges to the pressure while  $\gamma$  to  $u_y$  along the vertical element boundaries and to  $u_x$  on the horizontal ones.

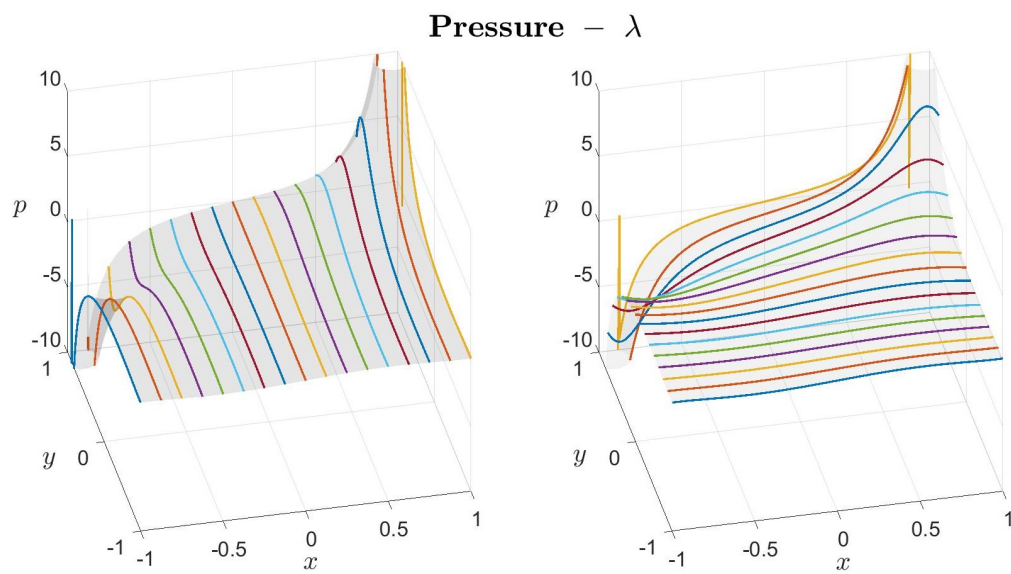


Figure 6.4: Comparison of the reconstruction of the Lagrange multiplier  $\lambda$  along internal element boundaries (colored lines) with the pressure (grey shadow).  $16 \times 16$  grid,  $4^{th}$  order elements.



gence of the velocity, which demonstrates the fact that it is equal to zero up to machine precision. Furthermore, Figure 6.7 shows the  $L^2$ -error for the divergence of the velocity ( $\mathbb{E}^{(n,n-1)}[u^{n-1}]$ ). Being at maximum  $O(10^{-11})$ , it can be stated that the incompressibility constraint is exactly satisfied using discontinuous elements even for very coarse meshes and low polynomial degree.

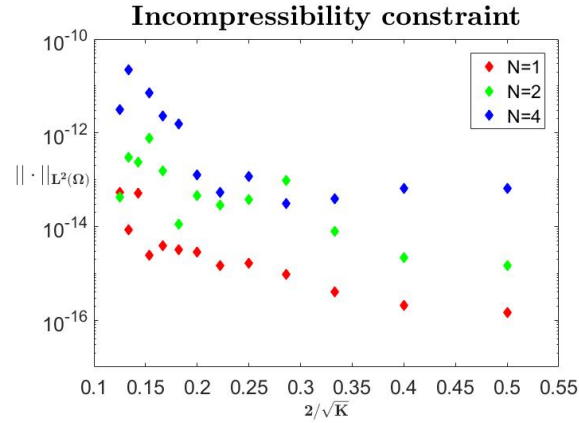


Figure 6.7: Incompressibility constraint.  $N = 1, 2, 4$  and  $K = \{4^2, 5^2, \dots, 16^2\}$ .

After having analysed the solution in the overall domain, it is interesting to have a direct comparison with the reference solution [23]. Generally, lid driven cavity flow solutions were compared looking at the horizontal velocity,  $u_x$ , on the vertical centreline and the vertical velocity,  $u_y$ , on the horizontal centreline.

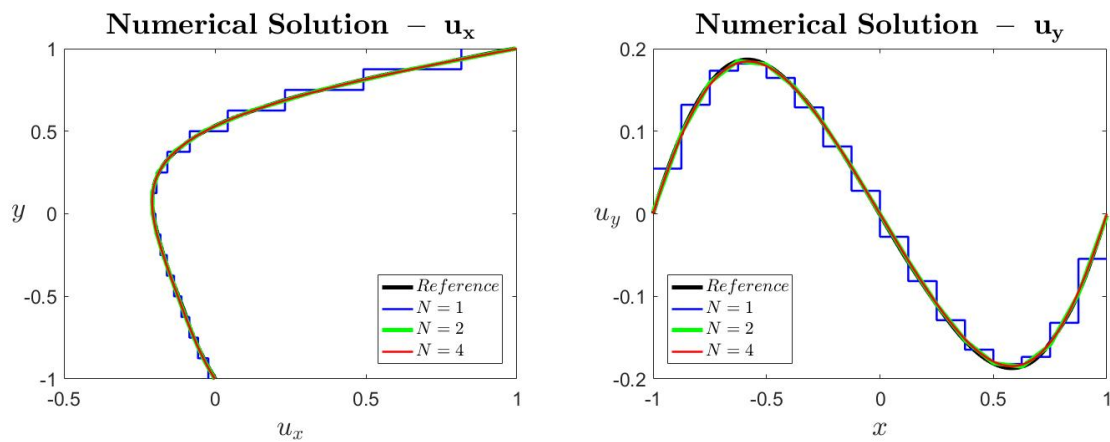


Figure 6.8: Comparison of horizontal velocity ( $u_x$ ) on the vertical centreline (left) and vertical velocity ( $u_y$ ) on the horizontal centreline. Reference solution [23].  $16 \times 16$  grid,  $1^{st}$ ,  $2^{nd}$  and  $4^{th}$  order elements.

These comparisons may be seen in Figure 6.8 (left) and (right), respectively. As can be seen, the numerical solutions for  $N$  equal to 2 and 4 overlap each other and the reference solution (in black). Obviously, the solution using the  $1^{st}$  order element degree, in which it is worth to recall that the velocity through the edges is described by constant basis functions, is the farthest from the reference solution. Furthermore, it can be seen that the horizontal and the vertical velocity do not match the boundary conditions ( $u_x(x, 1) = 1$ ,  $u_x(x, -1)$ ,  $u_y(-1, y)$ ,  $u_y(1, y) = 0$ ). So it is fundamental to understand if the velocity solution converges to the above-

mentioned boundary conditions.

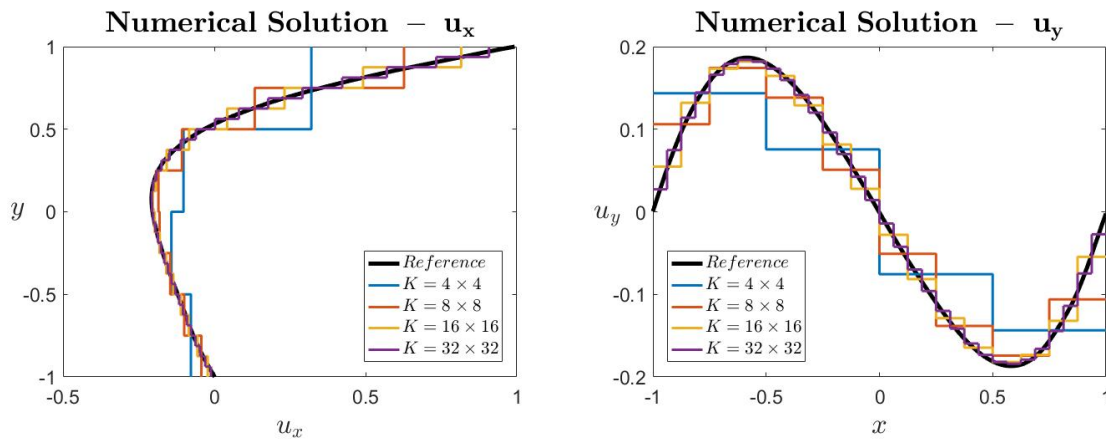


Figure 6.9: Horizontal velocity ( $u_x$ ) on the vertical centreline (left) and vertical velocity ( $u_y$ ) on the horizontal centreline. Reference solution [23].  $K = \{ 4^2, 8^2, 16^2, 32^2 \}$ ,  $1^{st}$  order elements.

To clearly show the solution’s convergence behaviour decreasing the element size,  $1^{st}$  degree elements were used in Figure 6.9 (left) and (right). In both graph the velocity solution on the boundary converges to the tangential boundary conditions increasing the number of element from  $4 \times 4$  to  $32 \times 32$ . We recall that the *Lagrange multiplier*  $\gamma$  strongly couples the nearest mesh points in the element boundaries (4.10,4.11,4.12,5.6). Furthermore, Figure 6.9 proves that it weakly imposes the tangential velocity’s boundary condition on the physical boundaries.

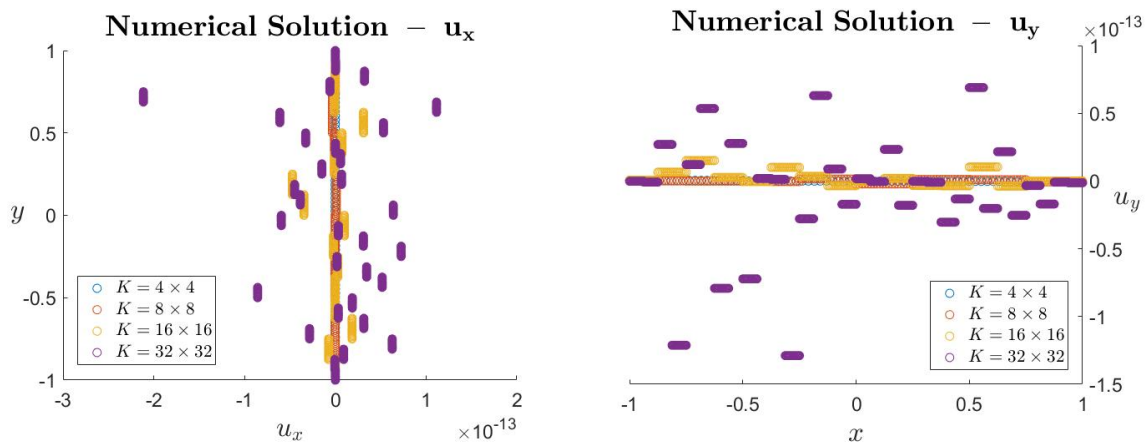


Figure 6.10: Horizontal velocity ( $u_x$ ) on the vertical centreline (left) and vertical velocity ( $u_y$ ) on the horizontal centreline.  $K = \{ 4^2, 8^2, 16^2, 32^2 \}$ ,  $1^{st}$  order elements.

In Figure 6.10 we show how well the impermeability boundary condition ( $\vec{u} \cdot \vec{n} = 0$  on  $\partial\Gamma$ ) is imposed. In Figure 6.1 blue primal edges were added at the boundary of the domain to impose this condition. The solution, restricted on the boundaries, can be seen in Figure 6.10, which proves that the velocity, normal to the boundary, is equal to zero up to machine precision for any element size (for clarity  $N = 1$  was chosen).

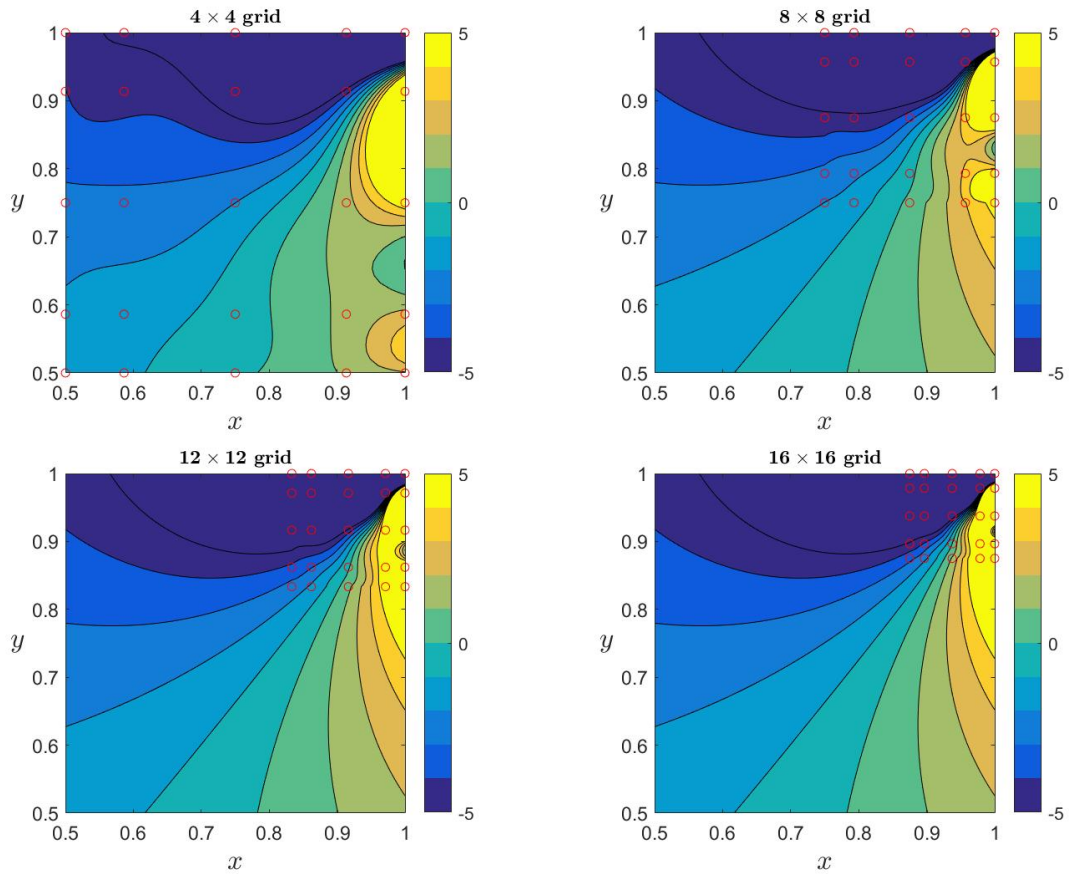


Figure 6.11: Effect of the  $h$ -convergence on the solution of the top-right vorticity ( $\omega$ ) singularity. Red empty circles show the primal points of the most upper-left element.

Figure 6.11 shows the solution of the vorticity,  $\omega$ , on the top-right corner of the domain ( $\Omega$ ) varying the number of elements. The primal points of the upper-right element are shown as empty red circles. Theory suggests that the point  $(1, 1)$  in  $\Omega$  is a singular point. The solution plots in Figure 6.11 shows that the contour lines does not intersect the boundary exactly in the vertex, but they approach it as much as the second primal point from the top on the right boundary, approach the previous-mentioned vertex. This ensures that the vorticity in  $(1, 1)$  has a finite value and that, increasing the number of elements and/or the polynomial degree, the solution approaches the theoretical one.

## Conclusions and further developments

This thesis has described the development of an hybrid mimetic formulation of the *vector Laplace* equation and its modification to solve *Stokes flow*. The motivations for studying such numerical method have been derived from the literature: coupling *mimetic* and hybrid methods combines the conservation properties of the former and the computational advantages of the latter. The difficulties hidden in the development of the hybrid formulation of the *vector Laplace* equation, noticed among the others by Cockbunn et. al. [14], are the spurious modes arising in the corner points.

Chapter 3 focused on the development of a continuous mimetic finite element method for the *Laplace equation*. In Chapter 4, the new hybrid mimetic method, derived by geometrical considerations, has been presented. Three different *Lagrange multipliers*  $(\lambda, \gamma, \theta)$  have been used and geometrically represented in the physical domain  $(\Omega)$ . It has been shown how, adding the third *Lagrange multiplier*  $\theta$ , the matrix formulation becomes non-singular. This eliminates the spurious modes and so affirmatively answers to the research question stated at the beginning of this thesis.

Furthermore, it has been shown that the *Lagrange multipliers* may be computed first and then used as boundary condition for the computation of the physical variables in each single element. This solution procedure has been proved to be faster than the solution of the continuous case, proving that the usage of discontinuous element of the hybrid approach can be an effective way to reduce the computational time of CFD calculations.

The numerical method has been verified using a divergence free manufactured solution on a square domain. The reconstructions of the *Lagrange multipliers* along the element boundaries have proved to converge to the physical variables predicted from the mixed formulation. Indeed,  $\lambda$  and  $\gamma$ , which are used to impose the continuity between nearest mesh edges and points respectively, converge to the divergence and the tangential velocity solution. Differently,  $\theta$  turns out to be equal to zero, up to machine precision, for any mesh

size and element degree. As expected from a mimetic method, the divergence of the solution is zero up to machine precision. Furthermore, the optimal  $h$ -convergence of the physical variables ( $p$ ,  $\omega$  and  $u$ ) has been demonstrated and the exponential  $p$ -convergence shown. Optimal convergence has been shown even for the *Lagrange multiplier*  $\lambda$ , while an expected sub-optimal convergence rate has been shown regarding  $\gamma$ .

At the end, in Chapter 6, the hybrid mimetic method has been modified to solve the Stokes equations. The matrix formulation has been compared to the continuous one developed by J.Kreeft et. al. [19] showing the fewer non-zero entries for the method developed in this thesis. The physical variables have been compared to a reference solution and the point-wise divergence free constraint has been shown. Doing so, the correct usage of the *Lagrange multipliers* and the imposition of the boundary condition have been proven. In conclusion, the weak imposition of the tangential boundary condition and the strong imposition of the normal boundary condition have been shown for different element sizes.

## 7.1. Further developments

In this thesis, while replying to the research question, weak points have been found and underlined. Aiming to solve them, further developments are suggested. They focus on:

- a physical meaning for the *Lagrange multiplier*  $\theta$ ;
  
- the possibility of an  $h$  or  $p$  refinement to be included in the development of the hybrid formulation.

In the next two sections, ideas that will help the numerical development of the above-mentioned tasks will be presented.

### 7.1.1. A physical meaning for $\theta$

Aiming to understand the physical meaning of  $\theta$ , which is the *Lagrange multiplier* arising in the intersection point of four elements, we look back at the hybrid element. In this respect, recalling Section 4.1, it is worth to recall that the red *Lagrange multipliers* on the boundary of the element in Figure 4.1 are not the perfect dual of the complete black boundary. Instead, the perfect duality may be seen in Figure 7.1.

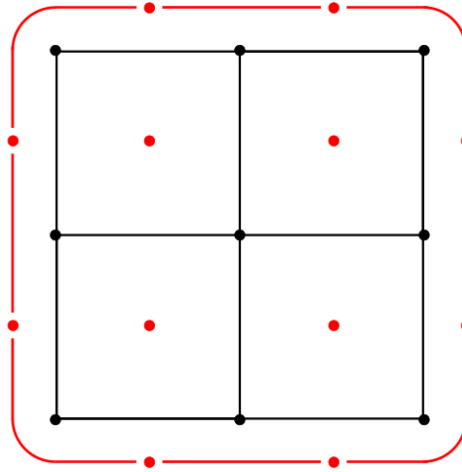


Figure 7.1: Element with embedded dual boundary.

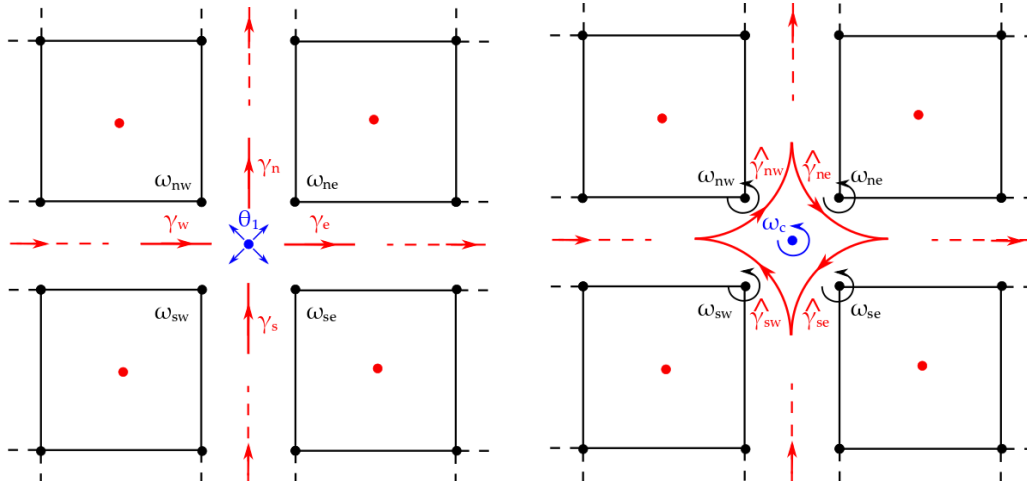


Figure 7.2: Comparison of the *Lagrange multipliers*' location on the intersection of four elements: numerical method developed along this thesis (left) and its possible improvement (right).

From Figure 7.1 a new configuration for the *Lagrange multipliers* may be created around the intersection of more than two elements<sup>1</sup>. This new configuration can be seen in Figure 7.2 (right) and can be compared to the one used in Chapter 4 (left). Differences are not only the curved *Lagrange multipliers*  $\gamma$  around the element corner, but even the sign convention of the *Lagrange multiplier* in the middle: in Chapter 4,  $\theta$  has been described as a 0-dimensional volume (source), while the correspondent *Lagrange multiplier* in this new approach, called  $\omega_c$ , is an outer oriented point as  $\omega$ .

Starting from the Lagrange functional for the *vector Laplace* equation defined as follows:

$$\begin{aligned} \mathcal{L}(u, p, \omega, \lambda, \gamma, \omega_c; f) = & \int_{\Omega_K} \frac{1}{2} \omega^2 d\Omega_K - \int_{\Omega_K} \frac{1}{2} p^2 d\Omega_K - \int_{\Omega_K} \text{div}(u) p d\Omega_K + \\ & + \int_{\Omega_K} u(-\text{curl}(\omega) - f) d\Omega_K + \int_{\partial\Omega_K} u \lambda d\partial\Omega_K + \int_{\partial\Omega_K} (\omega_c - \omega) \gamma d\partial\Omega_K \quad , \end{aligned} \tag{7.1}$$

<sup>1</sup>Having changed only the *Lagrange multipliers* in the corners, the hybridization of straight interfaces remain unchanged.

the variational problem may be computed taking variations around  $u, p, \omega, \lambda, \gamma, \omega_c$ . The equations arising from the variations around  $p, \omega, u$  and  $\lambda$  are equal to the first four of the variational formulation in (4.25). Instead, the last two equations of the system change around the intersections points. From the variational formulation:

$$\int_{\partial\Omega_K} \gamma (\omega_c - \omega) \, d\partial\Omega_K = 0 \quad , \quad (7.2)$$

$$\int_{\partial\Omega_K} \omega_c \gamma \, d\partial\Omega_K = 0 \quad , \quad (7.3)$$

and Figure 7.2 (right) a new set of equations may be written for each corner point:

$$\begin{aligned} \gamma_{ne} (\omega_{ne} - \omega_c) &= 0 \\ \gamma_{se} (\omega_{se} - \omega_c) &= 0 \\ \gamma_{sw} (\omega_{sw} - \omega_c) &= 0 \quad . \\ \gamma_{nw} (\omega_{nw} - \omega_c) &= 0 \\ \omega_c (-\gamma_{ne} - \gamma_{se} - \gamma_{sw} - \gamma_{nw}) &= 0 \end{aligned} \quad (7.4)$$

This new reasoning should maintain the non-singularity of the numerical method and, at the same time, assign to the *Lagrange multiplier* in the middle of the corner ( $\omega_c$ ) a physical meaning:  $\omega_c$  should converge to the vorticity of the solution in the intersection point.

### 7.1.2. $h$ and $p$ local refinement

Although it was not mentioned explicitly, all along the thesis, meshes were uniform and composed of elements of the same degree.  $h$  or  $p$  local refinements may be useful in physical application when gradients in the physical variables change on the fluid domain. As example, in the lid-driven cavity Stokes-flow, refinements would be useful in the corners of the domain where gradients are high, while the rest of the domain, characterized by lower gradients, may be solved accurately with a coarser mesh and lower polynomial degree.

In Chapter 4, *Lagrange multipliers* have been used to impose the continuity constraint between conformal meshes (Figures 4.2 and 4.4) in which the mesh points (and so the mesh edges) match up along the element boundary.

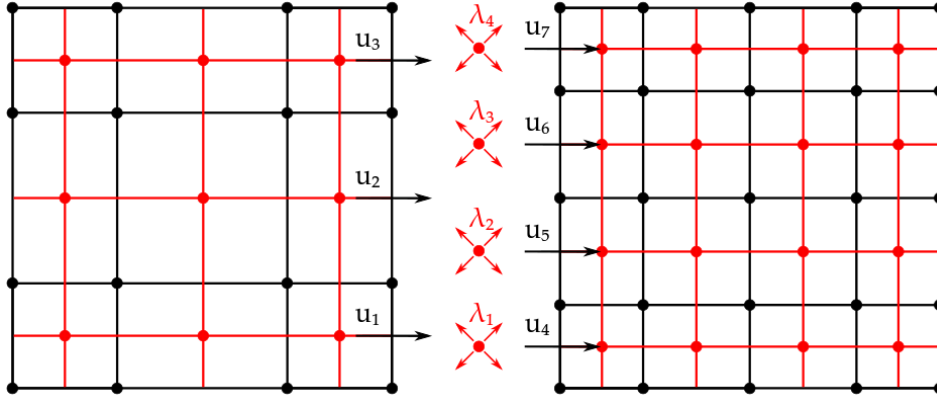
Figure 7.3: Graphical representation of a  $p$ -refinement.

Figure 7.3 shows the non-conformal boundary interfaces derived by a  $p$  refinement. *Lagrange multipliers*,  $\lambda$ , are added to impose the continuity between nearest edges. They are considered as the dual of the most refined side of interface (in Figure 7.3 it is the right side). The continuity may be imposed between edges modifying (4.2) in the following way:

$$\int_{\partial K \setminus \partial \Omega} \lambda (\sum u_R - \sum u_L) d\partial \Omega = 0 \quad . \quad (7.5)$$

|       | $\lambda_1$ | $\lambda_2$ | $\lambda_3$ | $\lambda_4$ |
|-------|-------------|-------------|-------------|-------------|
| $u_1$ | 0.763621    | 0.361379    | -0.174335   | 0.049335    |
| $u_2$ | -0.116326   | 0.616326    | 0.616326    | -0.116326   |
| $u_3$ | 0.049335    | -0.174335   | 0.361379    | 0.763621    |
| $u_4$ | 1           | 0           | 0           | 0           |
| $u_5$ | 0           | 1           | 0           | 0           |
| $u_6$ | 0           | 0           | 1           | 0           |
| $u_7$ | 0           | 0           | 0           | 1           |

Table 7.1: Value of  $\int_{\partial K \setminus \partial \Omega} u_i \lambda_j d\partial \Omega$ 

The table above shows the value of the integral  $\int_{\partial K \setminus \partial \Omega} u_i \lambda_j dl$ . It is worth to point out that this integral is metric independent. Furthermore, from the table, it is clearly visible that the *Lagrange multipliers* are the dual of the right interface: for this reason the value of the integrals can be only 0 or 1. From (7.5) and the Table 7.1, four equations may be written. The one related to  $\lambda_1$  is the following:

$$(+1)u_4 - (+0.763621)u_1 - (-0.116326)u_2 - (+0.049335)u_3 = 0 \quad , \quad (7.6)$$

and the other equations may be written accordingly. This idea was not tested numerically and consequently further developments are needed. However, one of the problems that will arise is the increase of the non-zero entry in the matrix  $\mathbb{E}^{\lambda, n-1}$  which may effect the sparsity structure of the system.

Analogously, Figure 7.4 shows an  $h$ -refinement.

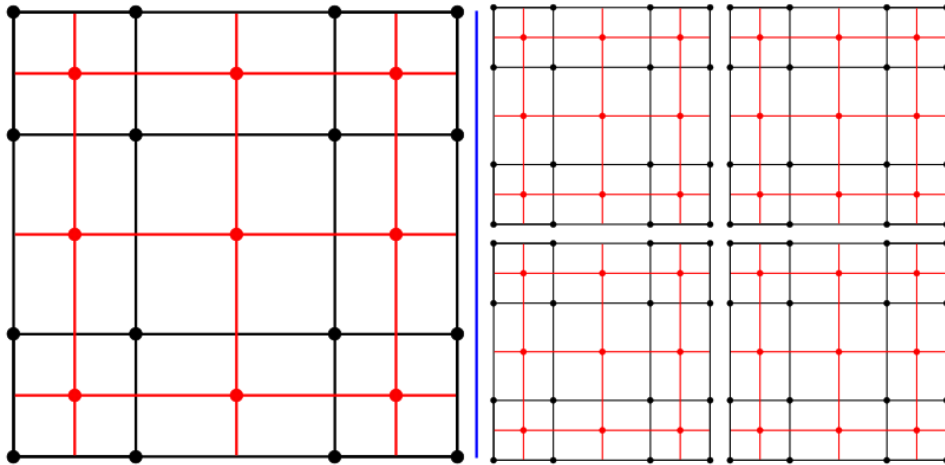


Figure 7.4: Graphical representation of an  $h$ -refinement.

Looking at the figure, it is clear an  $h$ -refinement not only disjoint points and edges as the  $p$ -refinements, but originates even a corner point in which 3 elements come together. Further developments are needed to understand if an additional *Lagrange multiplier*, such as  $\theta$  or  $\omega_c$  is needed in this case or not.

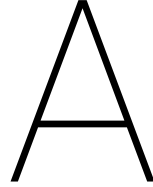
# Bibliography

- [1] D. N. Arnold, R. S. Falk, and R. Winther. Finite element exterior calculus: from Hodge theory to numerical stability. *Bull. Amer. Math. Soc.*, 47:281–354, 2010.
- [2] D. N. Arnold, R. S. Falk, and J. Gopalakrishnan. Mixed finite element approximation of the vector Laplacian with Dirichlet boundary conditions. *Mathematical Models and Methods in Applied Sciences*, 22, 2012.
- [3] D. N. Arnold, F. Brezzi, B. Cockburns, and L. D. Marini. Unified analysis of discontinuous Galerkin methods for elliptic problems. *SIAM J. Numer. Anal.*, 39:1749–1779, 2018.
- [4] R. Baumann and T. P. Wihler. A nitsche finite element approach for elliptic problems with discontinuous Dirichlet boundary conditions. *Computational Methods in Applied Mathematics*, 18(3):373–381, 2017.
- [5] P. Bochev and M. Gerritsma. A spectral mimetic least-squares method. *Computers and Mathematics with Applications*, 68:1480–1502, 2014.
- [6] P. B. Bochev and J. M. Hyman. Principles of mimetic discretizations of differential operators. *The IMA Volumes in Mathematics and its Applications*, 142:89–119, 2006.
- [7] D. Boffi, F. Brezzi, and M. Fortin. Mixed finite element methods and applications. *Springer Series in Computational Mathematics*, 44, 2013.
- [8] O. Bottella and R. Peyret. Benchmark spectral results on the lid-driven cavity flow. *Computers and Fluids*, 27:421–433, 1998.
- [9] H. C. Brinkman. A calculation of the viscous force exerted by a flowing fluid on a dense swarm of particles. *Appl. Sci. Res.*, A1:27–34, 1947.
- [10] P. Castillo. Performance of discontinuous Galerkin methods for elliptic PDEs. *SIAM J. Sci. Comput.*, 24: 524–547, 2002.
- [11] B. Cockburn and J. Gopalakrishnan. A characterization of hybridized mixed methods for second order elliptic problems. *SIAM J. Numer. Anal.*, 42:283–301, 2004.
- [12] M. Gerritsma. Edge functions for spectral element methods. *Spectral and High Order Methods for Partial Differential Equations*, page 199–208, 2010.

- [13] M. Gerritsma, V. Jain, Y. Zhang, and A. Palha. Algebraic dual polynomials for the equivalence of curl-curl problems. *arXiv preprint arXiv:1805.00114*, 2018.
- [14] B. Cockburn J. Gopalakrishnan. Incompressible finite elements via hybridization. Part I: The Stokes system in two space dimensions. *SIAM J. Numer. Anal.*, 43:1627–1650, 2005.
- [15] V. Jain, Y. Zhang, A. Palha, and M. Gerritsma. Construction and application of an algebraic dual polynomial representation for finite element methods. *ArXiv*, 2017.
- [16] D. A. Kopriva. Multidomain spectral solution of the euler gas-dynamics. *J. Comput. Phys.*, 96:428–450, 1991.
- [17] D. A. Kopriva. A staggered-grid multidomain spectral method for the compressible Navier–Stokes equations. *J. Comput. Phys.*, 143:125–158, 1998.
- [18] D. A. Kopriva and J. H. Kolas. A conservative staggered-grid chebyshev multidomain method for compressible flows. *SIAM J. Numer. Anal.*, 43, 1996.
- [19] J. Kreeft and M. Gerritsma. Mixed mimetic spectral element method for Stokes flow: A pointwise divergence-free solution. *Journal of Computational Physics*, 240:284–309, 2013.
- [20] J. Kreeft, A. Palha, and M. Gerritsma. Mimetic framework on curvilinear quadrilaterals of arbitrary order. *submitted to FoCM*, Arxiv preprint arXiv:1111.4304:1–69, 2010.
- [21] K. Lipnikov, G. Manzini, and M. Shashkov. Mimetic finite difference method. *Journal of Computational Physics*, 257:1163–1227, 2014.
- [22] W. L. Oberkampf and T. G. Trucano. Verification and validation in computational fluid dynamics. *Progress in Aerospace Sciences*, 38:209–272, 2002.
- [23] M. Sahin and R. G. Owens. A novel fully implicit finite volume method applied to the lid-driven cavity problem—part I: High reynolds number flow calculations. *Int. J. Numer. Meth. Fluids*, 42:57–77, 2003.
- [24] V. Subramanian and J. B. Perot. Higher-order mimetic methods for unstructured meshes. *J. Comput. Phys.*, 219:68–85, 2006.
- [25] T. Tarhasaari, L. Kettunen, and A. Bossavit. Some realizations of a discrete Hodge operator: a reinterpretation of finite element techniques. *IEEE Transactions on magnetics*, 35:1494–1497, 1999.
- [26] E. Tonti. On the mathematical structure of a large class of physical theories. *Rend. Acc. Lincei*, 52:48–56, 1972.
- [27] E. Tonti. The reason for analogies between physical theories. *Appl. Math. Modelling*, 1:36–50, 1976.
- [28] E. Tonti. Why starting from differential equations for computational physics? *J. Comput. Phys.*, 257:1260–1290, 2014.

- 
- [29] Y. Zhang, V. Jain, A. Palha, and M. Gerritsma. The discrete Steklov-Poincaré operator using algebraic dual polynomials. *Computational Methods in Applied Mathematics*, 2018.





## 2-dimensional basis functions

In Chapter 2 *primal* and *dual* basis functions have been constructed using the 1-dimensional *nodal* and *edge* polynomials.

In this appendix, all the *basis functions* belonging to the  $3^{rd}$  element in Figure 2.4 have been shown. It is worth to remember that each variable is approximated as a finite weighted sum of basis functions

$$\xi^{(k)} = \sum [\xi]^{(k)} e^{(k)} \quad . \quad (\text{A.1})$$

The weights,  $[\xi]^{(k)}$ , are called *cochain*.

The element size is the following:

$$\Omega_K = \left\{ \forall (x, y) \in \mathbb{R}^2 \mid -1 \leq x \leq 1 \& -1 \leq y \leq 1 \right\} \quad . \quad (\text{A.2})$$

### A.1. Primal basis functions

Starting from the primal basis functions, figure A.1 shows  $\epsilon^{(n-2)}$ , which are the basis functions associated to the points of the element. In the same figure, the point in which  $\epsilon_i^{(n-2)} = 1$  is shown in red to emphasize the connection between basis functions and geometry.

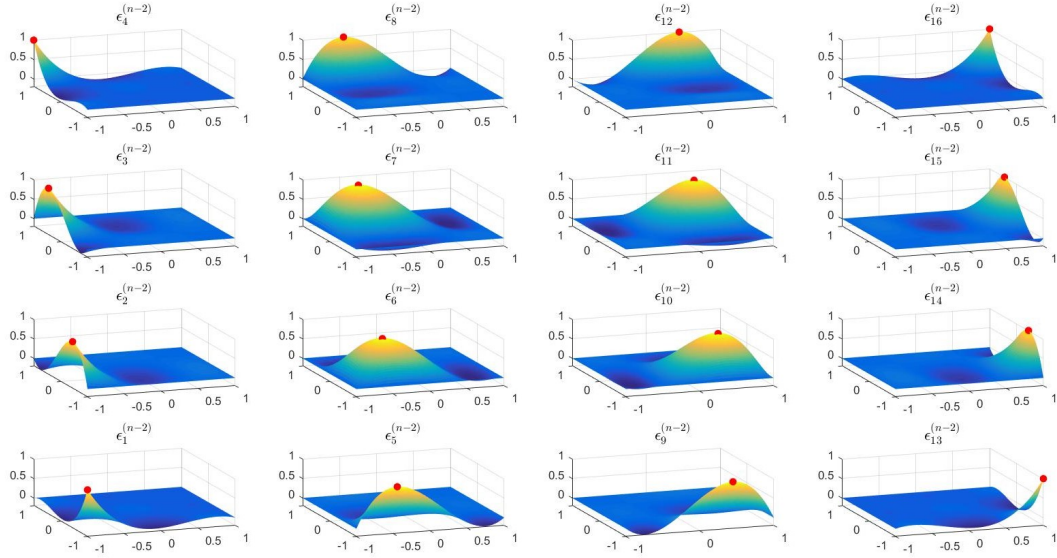


Figure A.1:  $\epsilon^{(n-2)}$  on a  $3^{rd}$  order element (Figure 2.4) in the domain  $\Omega_k$  (A.2).

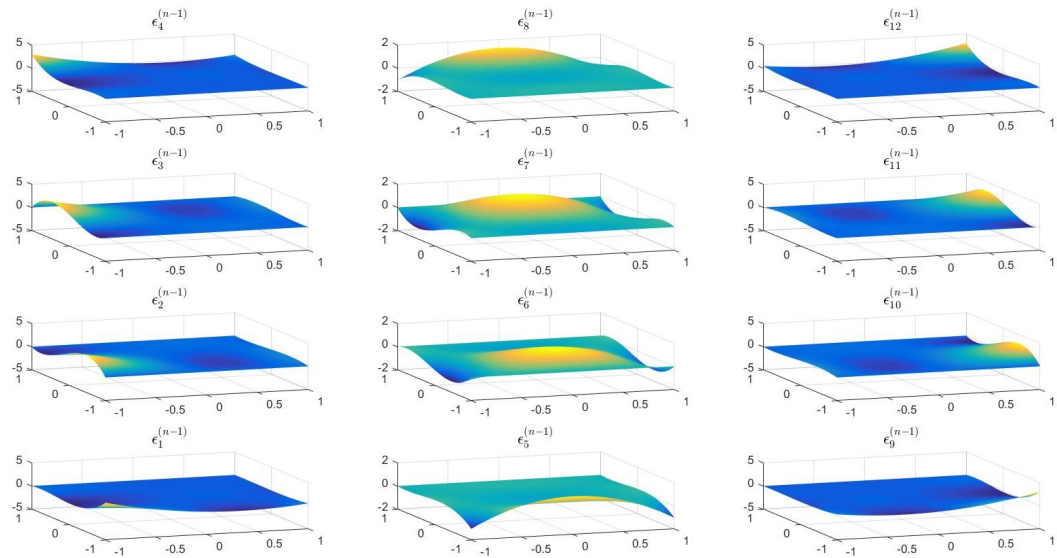


Figure A.2: Horizontal  $\epsilon^{(n-1)}$  on a  $3^{rd}$  order element (Figure 2.4) in the domain  $\Omega_k$  (A.2).

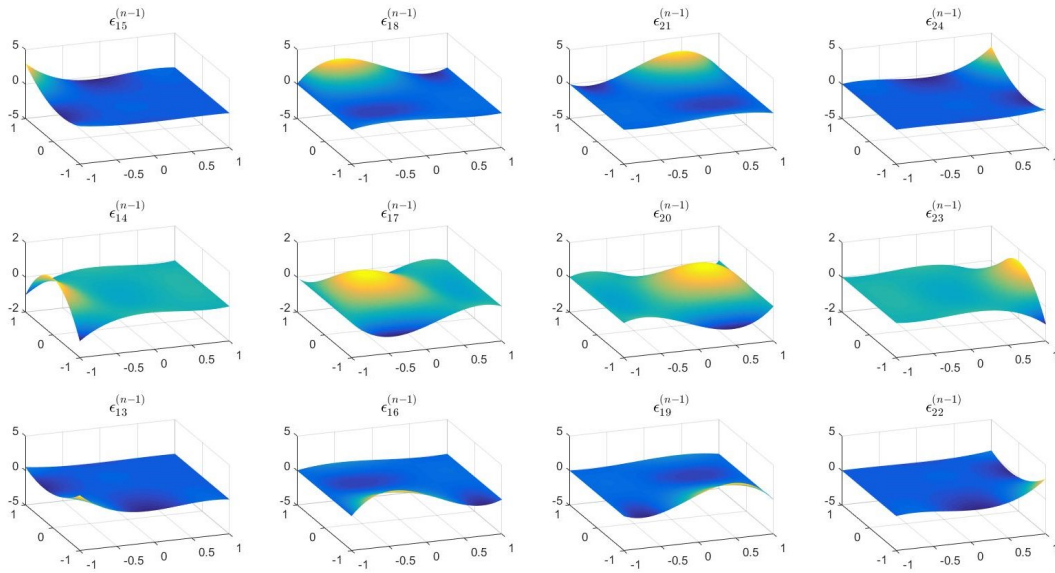


Figure A.3: Vertical  $\epsilon^{(n-1)}$  on a  $3^{rd}$  order element (Figure 2.4) in the domain  $\Omega_k$  (A.2).

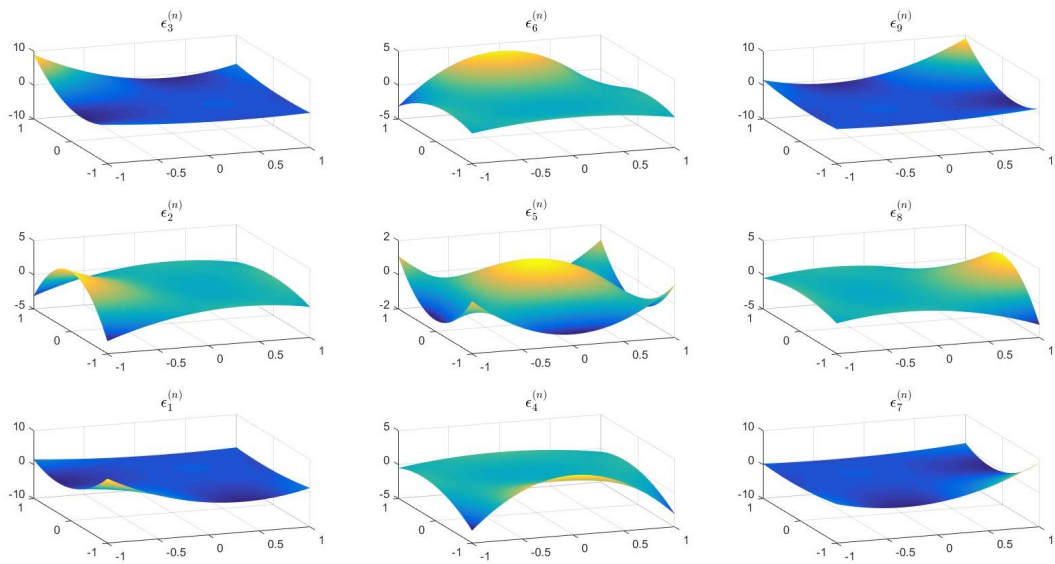


Figure A.4:  $\epsilon^{(n)}$  on a  $3^{rd}$  order element (Figure 2.4) in the domain  $\Omega_k$  (A.2).

## A.2. Perfect-dual basis functions

As it was already underlined in chapter 2, only the *perfect dual basis functions* will be used in this thesis and for this reason simply called *dual basis functions*. Contrarily to the primal basis functions, the *perfect-dual basis functions* have lost the connection to the geometry.

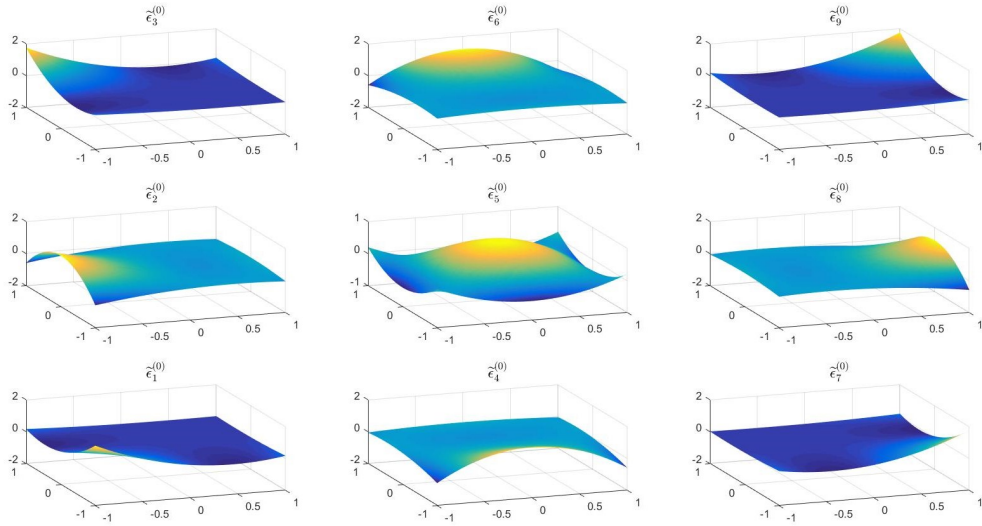


Figure A.5:  $\tilde{\epsilon}^{(0)}$  on a  $3^{rd}$  order element (Figure 2.4) in the domain  $\Omega_k$  (A.2).

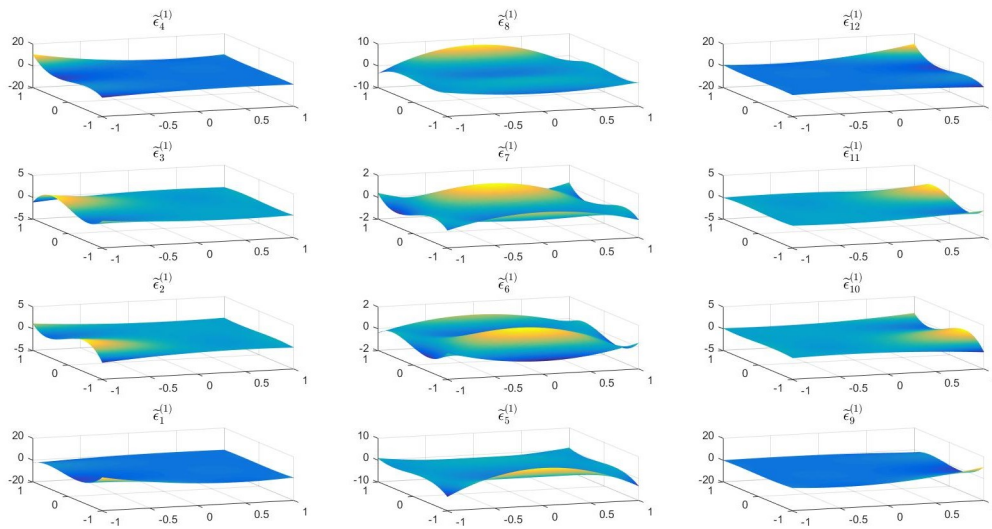


Figure A.6: Vertical  $\tilde{\epsilon}^{(1)}$  on a  $3^{rd}$  order element (Figure 2.4) in the domain  $\Omega_k$  (A.2)

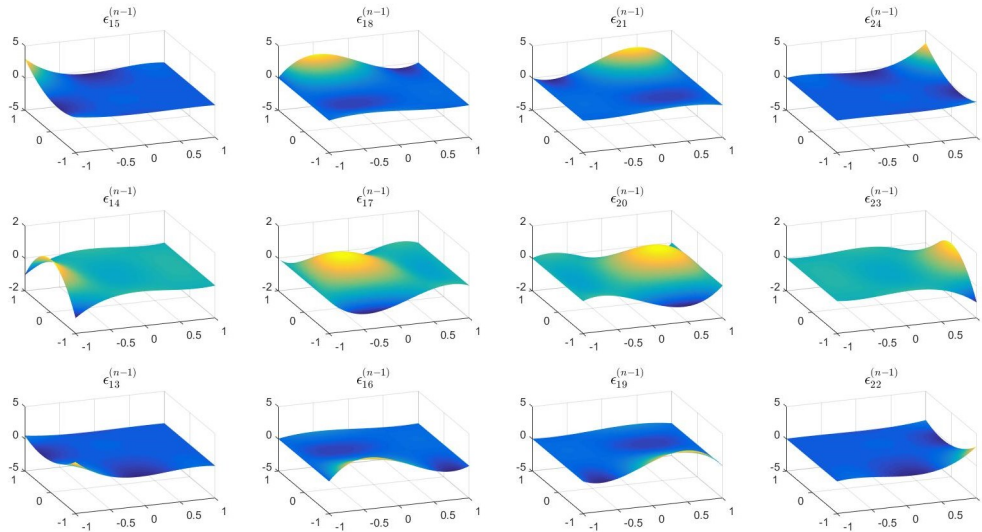


Figure A.7: Horizontal  $\tilde{\epsilon}^{(1)}$  on a  $3^{rd}$  order element (Figure 2.4) in the domain  $\Omega_k$  (A.2)

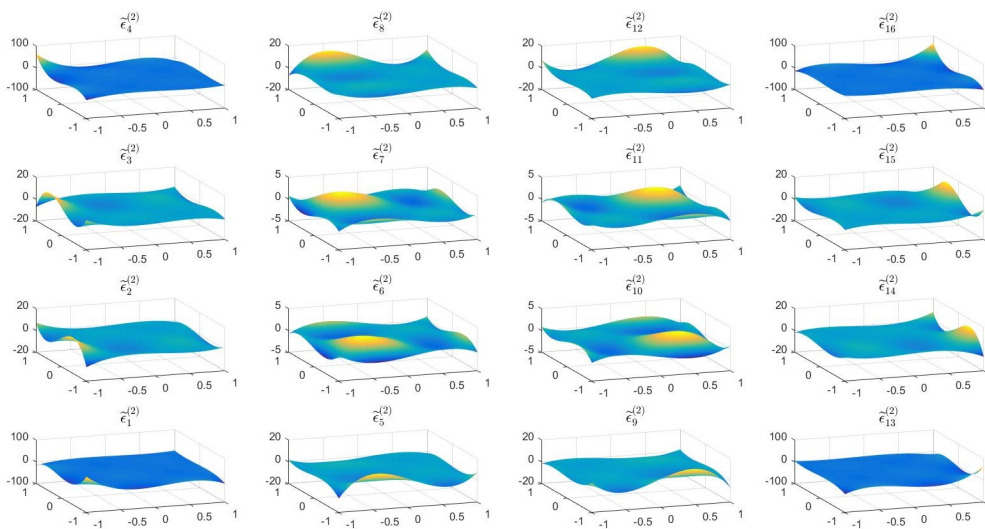


Figure A.8:  $\tilde{\epsilon}^{(2)}$  on a  $3^{rd}$  order element (Figure 2.4) in the domain  $\Omega_k$  (A.2)



# B

## Verification: continuous formulation

The continuous primal-dual formulation (3.18) has been verified using the method of the *manufactured solution* on the following domain:

$$\Omega = \{ \forall (x, y) \in \mathbb{R}^2 \mid -1 \leq x \leq 1 \ \& \ -1 \leq y \leq 1 \} . \quad (\text{B.1})$$

### B.1. Manufactured solution

In order to compare the continuous and the hybrid formulation (Chapter 5), the same divergence free manufactured solution has been chosen in order to verify the continuous formulation:

$$u = \begin{pmatrix} \cos(\pi x) \sin(\pi y) \\ -\sin(\pi x) \cos(\pi y) \end{pmatrix} . \quad (\text{B.2})$$

The curl of the vector field  $u$  is the following:

$$\omega = -2\pi \cos(\pi x) \cos(\pi y) , \quad (\text{B.3})$$

and the RHS,  $f$ , is equal to

$$f = \begin{pmatrix} -2\pi^2 \cos(\pi x) \sin(\pi y) \\ 2\pi^2 \sin(\pi x) \cos(\pi y) \end{pmatrix} . \quad (\text{B.4})$$

It has to be noted that  $\nabla \cdot \vec{u} = 0$  and  $\vec{u} \cdot \vec{\tau} = 0$  in  $\partial\Omega$ , so no boundary terms have to be computed.

### B.2. Qualitative analysis

Using the continuous primal dual formulation (3.18) and substituting the cochain  $[f]^{(n-1)}$  on the RHS, the solution can be computed.

Figures B.1, B.2 and B.3 compare the exact and the numerical solution of the vorticity,  $\omega$ , horizontal,  $u_x$ , and vertical,  $u_y$ , velocity. As it can be seen, the numerical solution (left) resemble the exact one (right). Furthermore, comparing figures B.1, B.2 and B.3 to 5.4, 5.5 and 5.6, it can be seen that the hybrid (discontinuous) formulation is as good as the continuous one.

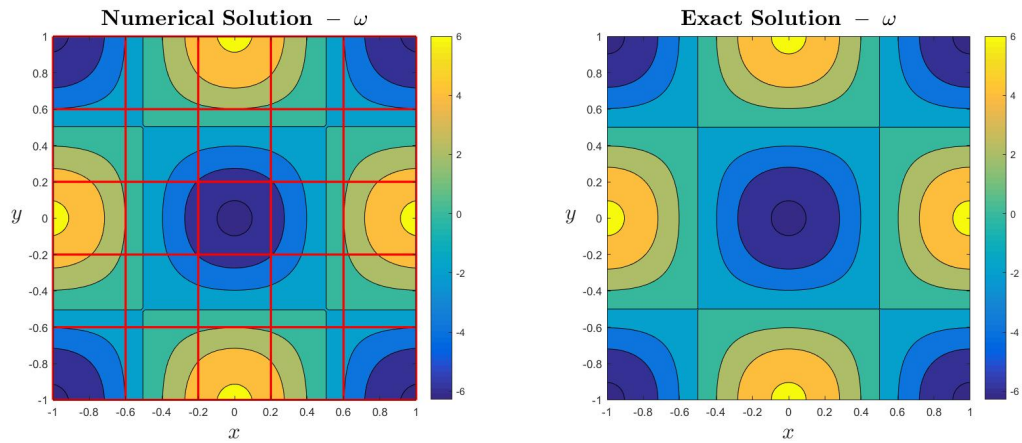


Figure B.1: Comparison between the numerical (left) and the exact solution (right) of the vorticity ( $\omega$ ).  $5 \times 5$  grid,  $2^{nd}$  order elements.

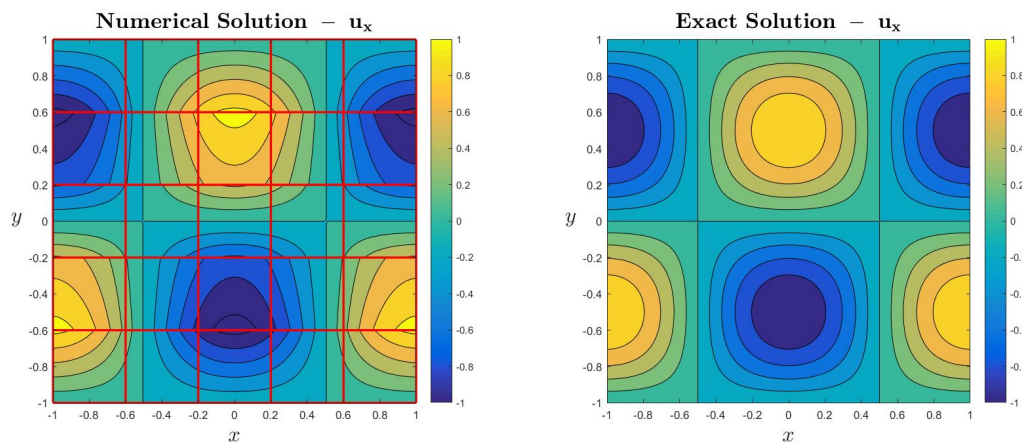


Figure B.2: Comparison between the numerical (left) and the exact solution (right) of the horizontal velocity ( $u_x$ ).  $5 \times 5$  grid,  $2^{nd}$  order elements.

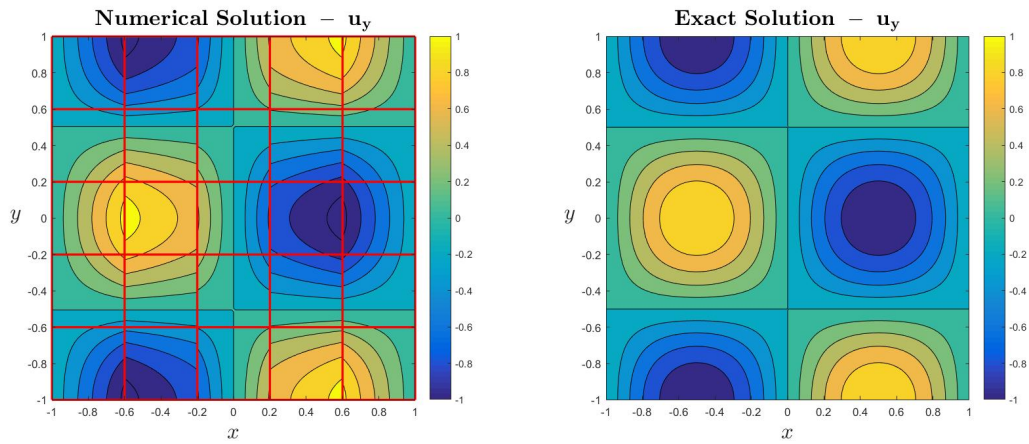


Figure B.3: Comparison between the numerical (left) and the exact solution (right) of the vertical velocity ( $u_x$ ).  $5 \times 5$  grid,  $2^{nd}$  order elements.

### B.3. Convergence analysis

In order to unequivocally prove that the numerical solution of the continuous formulation converges to the exact mathematical solution, an error analysis has to be conducted. Figures B.4 and B.5 show the convergence of the error increasing the number of elements, for element degree 1, 2 and 3. The error has been computed using the following formula:

$$\| \phi^e - \phi^h \|_{L^2(\Omega)} = \sqrt{\int_{\Omega} (\phi^e - \phi^h)^2} \quad , \quad (B.5)$$

where  $\phi^e$  indicates the exact solution and  $\phi^h$  the reconstruction of the numerical solution.

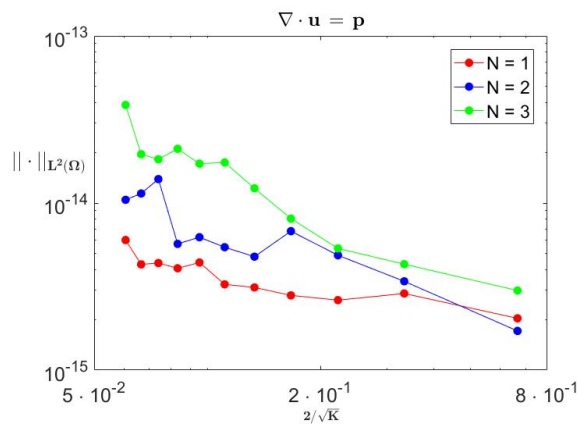


Figure B.4: h-Convergence plot of  $L^2(\Omega)$ -error of the divergence of  $u, p$ .  $K = \{ 3^2, 6^2, \dots, 33^2 \}$ .

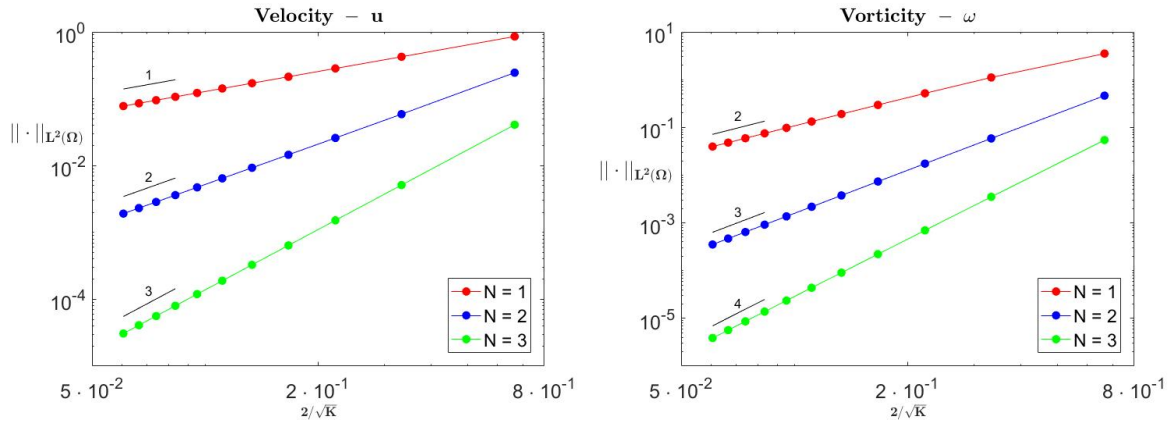


Figure B.5:  $h$ -convergence of  $L^2(\Omega)$ -error of the velocity  $u$  (left) and the vorticity (right).  $K = \{3^2, 6^2, \dots, 33^2\}$ .

Figure B.4 shows the error on the divergence of the velocity ( $\nabla \cdot \vec{u} = 0$ ) in function of the the element size. It can be seen that the error increases increasing the element size  $2/\sqrt{K}$ , but it is always lower than  $10^{-13}$ . This proves that the solution is exactly divergence free for any element degree and size. Furthermore, the  $h$ -convergence rate of the velocity  $-u-$  (left) and vorticity  $-\omega-$  (right) may be seen in figure B.5. Calling  $N$  the element degree,  $\omega$  is described by a function of degree  $N$  in both direction, while  $u_x$  and  $u_y$  are described by a 2-dimensional function of degree  $N$  in one direction and  $N - 1$  in the other one. This explains why the convergence rates, depicted in B.5, are *optimal*.

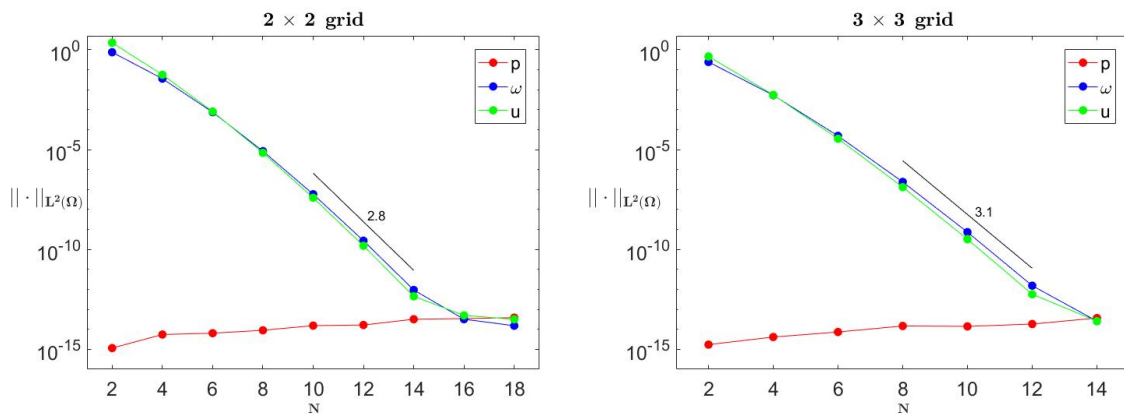


Figure B.6:  $p$ -convergence of  $L^2(\Omega)$ -error of the  $p$ ,  $u$  and  $\omega$ .  $2 \times 2$  grid (left)  $3 \times 3$  grid (right).

Figure B.6 shows the exponential convergence of the velocity  $-u-$  and the vorticity  $-\omega-$  increasing the element degree. Furthermore, it can be seen that  $p$  is equal to zero up to machine precision for any element degree.

## B.4. Analysis on the sparsity structure

In Chapter 3 it has been underlined how the primal-dual formulation, although it dissociates the dual variable from the dual grid, leads to a matrix formulation with fewer non-zero entries. In this section, we would like to

analyse the sparsity structure of the matrix as a function of the method used to compute the mass matrices. We will focus on the the outer ones  $\mathbb{M}^{(n-2)}, \mathbb{M}^{(n-1)}$  and  $\mathbb{M}^{(n)}$ , which appear in the matrix formulation.

Recalling that the mass matrices are defined in the following way:

$$\mathbb{M}^{(n-k)} = \int_{\Omega} \epsilon_i^{(n-k)} \epsilon_j^{(n-k)} d\Omega \quad , \quad (\text{B.6})$$

it hasn't been explained how the integral is numerically computed.

Methods able to numerically compute integrals are a key part of the numerical analysis. In this thesis, the Lobatto-Quadrature rule has been chosen for the evaluation of the integral regarding the primal basis functions, which are defined on a grid based on the Lobatto points.

Calling  $x_i$  the Lobatto points<sup>1</sup>, the integral of a function  $\psi$  over a 1-dimensional domain  $\Omega$ , may be computed using the following formula:

$$\int_{\Omega} \psi d\Omega = \sum_{i=1}^N \psi(x_i) w_i \quad , \quad (\text{B.7})$$

where the weights  $w_i$  are equal to:

$$w_i = \frac{2}{N(N-1)(L_{N-1}(x_i))^2} \quad . \quad (\text{B.8})$$

( $L_{N-1}$  indicates the Legendre polynomial of degree  $N-1$ .)

The mass matrices associated to the primal points  $\mathbb{M}^{(n-2)}$ , are the integral of the product of 2 basis functions  $\epsilon^{(n-2)}$  each having degree  $N-1$  (in each direction), where  $N$  in the number of the primal points in the horizontal or vertical direction. This means that the integrand has degree  $(N-1)^2$ .

The Lobatto-Quadrature integration is exact up to degree  $2N-3$  where  $N$  in the number of the Lobatto points used in the quadrature rule, which may be different from the primal points in the mesh.

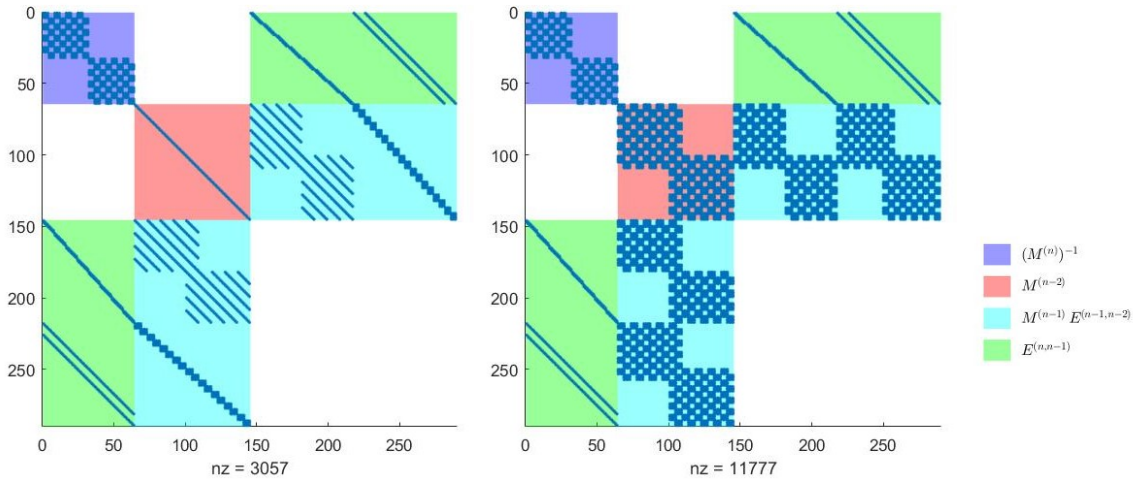


Figure B.7: Sparsity structure of the LHS in (3.17) computed using  $N$  (left) and  $2 * N$  Lobatto points (right).  $2 \times 2$  grid,  $4^{th}$  order elements.

Figure B.7 shows the sparsity structure of (3.17) computed using  $N$  (left) and  $2 * N$  (right) Lobatto points. It can be seen that only in the first case the matrix is very sparse but, being  $(N-1)^2 > 2N-3$  (if  $N > 2$ ), the

<sup>1</sup>Lobatto points are the roots of (2.18).

integration is not exact. In the second case, using  $2N$  points in the computation of the integral, the integration is exact but the matrix has almost 3 times more non-zero entries (3057 *vs* 11777).

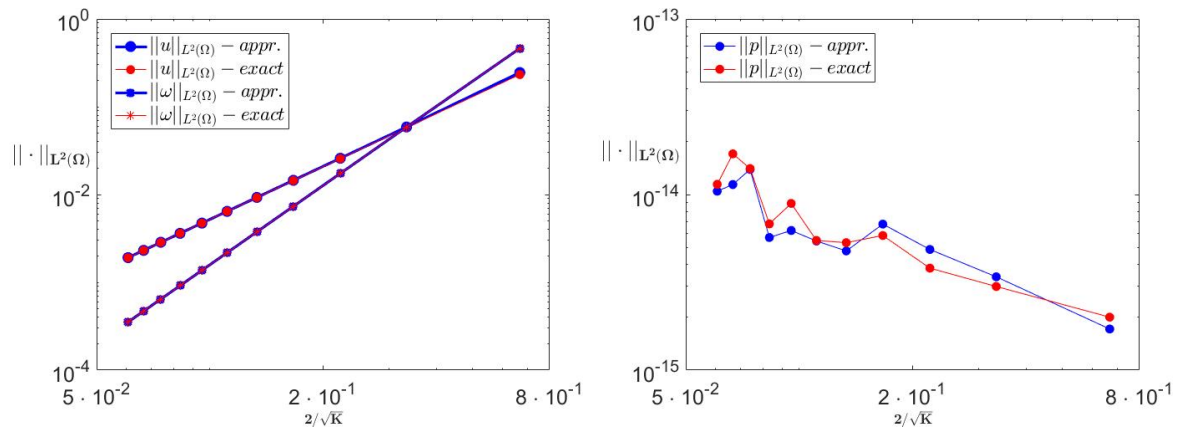


Figure B.8:  $h$ -convergence of  $L^2(\Omega)$ -error of  $u$  and  $\omega$  (left) and  $p$  (right) using the approximated matrix (figure B.7-left) and the exact one (figure B.7-right).

Figure B.8 shows the convergence error using the approximated (appr.) integration and the exact one. The error computed with the approximated sparse matrix is overlapping the ones computed with the exact full matrix.

Considering the fact that the approximated matrix returns the same solution as the exact one but, having fewer non-zero entries, requires less memory and allows a faster computation of the linear system, it has been used throughout this thesis.

# C

## Vector calculus

$$\begin{aligned}
 \int_{\Omega} \epsilon \nabla^* \times \vec{u} d\Omega &= \int_{\Omega} \epsilon \left( \frac{\partial \vec{u}_y}{\partial x} - \frac{\partial \vec{u}_x}{\partial y} \right) d\Omega \\
 &= \int_{\Omega} \epsilon \frac{\partial \vec{u}_y}{\partial x} d\Omega + \int_{\Omega} -\epsilon \frac{\partial \vec{u}_x}{\partial y} d\Omega \\
 &= \int_y \left[ \epsilon \vec{u}_y \Big|_{x=-1}^{x=1} - \int_x \frac{\partial \epsilon}{\partial x} \vec{u}_y dx \right] dy + \int_x \left[ -\epsilon \vec{u}_x \Big|_{y=-1}^{y=1} + \int_y \frac{\partial \epsilon}{\partial y} \vec{u}_x dy \right] dx \\
 &= \int_y \epsilon (\vec{u}_y(x, 1) - \vec{u}_y(x, -1)) dy + \int_x \epsilon (\vec{u}_x(-1, y) - \vec{u}_x(1, y)) dx + \\
 &\quad + \int_{\Omega} \left( \frac{\partial \epsilon}{\partial y}, -\frac{\partial \epsilon}{\partial x} \right) \cdot \vec{u} d\Omega \\
 &= \int_{\Omega} \nabla \times \epsilon \cdot \vec{u} + \int_{\partial\Omega} \epsilon \vec{u} \cdot \vec{\tau}
 \end{aligned} \tag{C.1}$$

$$\begin{aligned}
 \int_{\Omega} \vec{\epsilon} \nabla^* p d\Omega &= \int_{\Omega} \vec{\epsilon} \left( \frac{\partial p}{\partial x}, \frac{\partial p}{\partial y} \right) d\Omega \\
 &= \int_{\Omega} \vec{\epsilon}_x \frac{\partial p}{\partial x} d\Omega + \int_{\Omega} \vec{\epsilon}_y \frac{\partial p}{\partial y} d\Omega \\
 &= \int_y \left[ \vec{\epsilon}_y p \Big|_{x=-1}^{x=1} - \int_x \frac{\partial \vec{\epsilon}_x}{\partial x} p dx \right] dy + \int_x \left[ \vec{\epsilon}_x p \Big|_{y=-1}^{y=1} - \int_y \frac{\partial \vec{\epsilon}_y}{\partial y} p dy \right] dx \\
 &= \int_y \vec{\epsilon}_x (p(x, 1) - p(x, -1)) dy + \int_x \vec{\epsilon}_y (p(1, y) - p(-1, y)) dx + \\
 &\quad - \int_{\Omega} \left( \frac{\partial \vec{\epsilon}_x}{\partial x} + \frac{\partial \vec{\epsilon}_y}{\partial y} \right) p d\Omega \\
 &= - \int_{\Omega} \nabla \cdot \vec{\epsilon} p + \int_{\partial\Omega} \vec{\epsilon} \cdot \vec{n} p
 \end{aligned} \tag{C.2}$$





## Condition number and error propagation

Summing up the results, in Chapter 5, it was mentioned that the incompressibility constraint was exactly satisfied even when the error was  $O(10^{-12})$ . It was mentioned that this was due to the increase in the *condition number* of the matrix.

Assuming

$$\mathbb{A}\vec{x} = \vec{f} \quad , \quad (\text{D.1})$$

it is possible to bound the propagation of an error in  $\vec{f}$  to the solution  $\vec{x}$  [citare top]. Imposing an error in the rhs  $\delta\vec{f}$ , the following may be written:

$$\mathbb{A}(\delta\vec{x} + \vec{x}) = \delta\vec{f} + \vec{f} \quad . \quad (\text{D.2})$$

Because  $\mathbb{A}\vec{x} = \vec{f}$ , using the normo properties immediately leads to:

$$\|\delta\vec{x}\| \leq \|\mathbb{A}^{-1}\| \|\delta\vec{f}\| \quad , \quad (\text{D.3})$$

and dividing it by  $\|\vec{f}\|$ , the formula for the relative error propagation:

$$\frac{\|\delta\vec{x}\|}{\|\vec{x}\|} = \|\mathbb{A}\| \|\mathbb{A}^{-1}\| \frac{\|\delta\vec{f}\|}{\|\vec{f}\|} \quad . \quad (\text{D.4})$$

$\|\mathbb{A}\| \|\mathbb{A}^{-1}\|$  is the *condition number* of the matrix  $\mathbb{A}$ .

From (D.4) it is possible to see that an error in the rhs (for example the *machine precision error*) propagates to the solution  $\vec{x}$  but it is bounded by the *condition number*.



# E

## Elimination of spurious modes by Cockburn et. al. [14]

While reading this thesis, a reader may be interested in why singularities arise using the *Lagrange multipliers*  $\gamma$  and how Cockburn et. al. avoided them in [14]. This appendix will reply to these two questions.

First, it is interesting to underline why, using the *Lagrange multipliers*, singular modes arise on the intersection points.

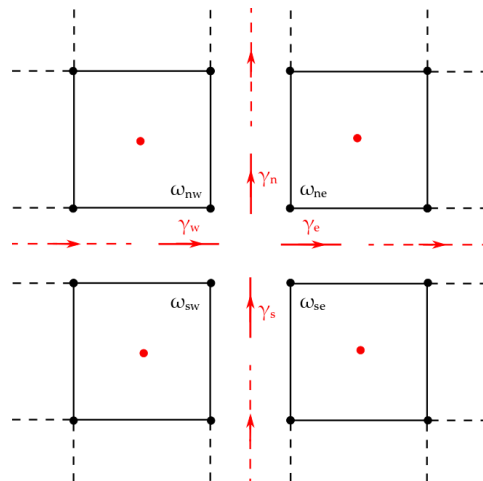


Figure E.1: Singular cross intersection.

Figure E.1 shows the point-intersection of four elements. We recall that *Lagrange multipliers*,  $\lambda$  and  $\gamma$ , have been used to impose the continuity between edges and points. Therefore, focusing on the intersection,

$\gamma$  have been used to impose the following identity:

$$\omega_{nw} = \omega_{ne} = \omega_{se} = \omega_{sw} \quad , \quad (\text{E.1})$$

which imposes the continuity of the vorticity. With this objective in mind, four *Lagrange multipliers* have been used. For each of them one equation is written in the system. These equations are:

$$\omega_{nw} - \omega_{ne} = 0 \quad , \quad (\text{E.2})$$

$$\omega_{ne} - \omega_{se} = 0 \quad , \quad (\text{E.3})$$

$$\omega_{sw} - \omega_{se} = 0 \quad , \quad (\text{E.4})$$

$$\omega_{nw} - \omega_{sw} = 0 \quad . \quad (\text{E.5})$$

It is clearly visible that  $\omega_{nw} = \omega_{ne}$ ,  $\omega_{ne} = \omega_{se}$  and  $\omega_{se} = \omega_{sw}$  lead to  $\omega_{sw} = \omega_{nw}$ , as a result (E.5) is linearly dependent on the other three equations. This yields to a singular system of equations.

Furthermore, in order to unequivocally prove that the singularities arise due to the four *Lagrange multiplier*  $\gamma$  near each intersection point, the kernel of the singular matrix in (4.19) can be numerically computed. Using a  $2 \times 2$  grid of  $2^{nd}$  order elements, the kernel is a one-dimensional space (one corner leads to one singular mode). The basis describing this function space has only one vector whose non zero entries are correspondent to  $\gamma_n$ ,  $\gamma_e$ ,  $\gamma_s$  and  $\gamma_w$ .

Cockburn et. al., in [14], noticed that not all  $\gamma$  (called  $\psi_\Lambda$  in their paper) are linearly independent. Using a triangular mesh and linear elements, they discovered that the number of linearly independent  $\gamma$  are  $3n_K - n_V$  where  $n_K$  and  $n_V$  are the number of triangles and vertices, respectively. Their solution consists in randomly deleting one *Lagrange multiplier*  $\gamma$  and the correspondent equation, for each vertex. Translating this methodology to the above example means to delete one of the four *Lagrange multipliers* and the corresponding equation. This leads to three linearly independent equations which originate a non-singular system.